Migration for Organelles and Bacteria in Insulator-Based Microfluidic Devices

by

Jinghui Luo

A Dissertation Presented in Partial Fulfillment
of the Requirements for the Degree
Doctor of Philosophy

Approved November 2015 by the
Graduate Supervisory Committee:

Alexandra Ros, Chair
Mark Hayes
Chad Borges

ARIZONA STATE UNIVERSITY

December 2015

ABSTRACT

Efficient separation techniques for organelles and bacteria in the micron- and sub-micron range are required for various analytical challenges. Mitochondria have a wide size range resulting from the sub-populations, some of which may be associated with diseases or aging. However, traditional methods can often not resolve within-species size variations. Strategies to separate mitochondrial sub-populations by size are thus needed to study the importance of this organelle in cellular functions. Additionally, challenges also exist in distinguishing the sub-populations of bio-species which differ in the surface charge while possessing similar size, such as *Salmonella typhimurium* (*Salmonella*). The surface charge of *Salmonella* wild-type is altered upon environmental stimulations, influencing the bacterial survival and virulence within the host tissue. Therefore, it is important to explore methods to identify the sub-populations of *Salmonella*.

This work exploits insulator-based dielectrophoresis (iDEP) for the manipulation of mitochondria and *Salmonella*. The iDEP migration and trapping of mitochondria were investigated under both DC and low-frequency AC conditions, establishing that mitochondria exhibit negative DEP. Also, the first realization of size-based iDEP sorting experiments of mitochondria were demonstrated. As for *Salmonella*, the preliminary study revealed positive DEP behavior. Distinct trapping potential thresholds were found for the sub-populations with different surface charges.

Further, DEP was integrated with a non-intuitive migration mechanism termed absolute negative mobility (ANM), inducing a deterministic trapping component which allows the directed transport of µm- and sub-µm sized (bio)particles in microfluidic devices with a nonlinear post array under the periodic action of electrokinetic and dielectrophoretic forces. Regimes were revealed both numerically and experimentally in which larger particles migrate against the average applied force, whereas smaller particles show normal response. Moreover, this deterministic ANM (dANM) was characterized with polystyrene beads demonstrating improved migration speed at least two orders of magnitude higher compared to previous ANM systems with similar sized colloids. In addition, dANM was induced for mitochondria with an AC-overlaid waveform representing the first demonstration of ANM migration with biological species. Thus, it is envisioned that the efficient size selectivity of this novel migration mechanism can be employed in nanotechnology, organelle sub-population studies or fractionating protein nanocrystals.

DEDICATION

To my family, especially my mother and father for their love and support.

To all my friends for their trust in me and their encouragement.

ACKNOWLEDGMENTS

First of all, I would like to express my sincere gratitude to my advisor and doctoral committee chair, Professor Alexandra Ros for not only providing me with the wonderful opportunity to work on the projects presented in this dissertation but also consistently offering me great guidance, support and timely feedbacks throughout my graduate studies.

I also would like to thank my supervisory committee members, Professor Mark Hayes and Professor Chad Borges, for their time and kind help in the completion of this work.

For the materials presented in Chapter 3, I would like to thank co-authors Bahige G. Abdallah from the School of Molecular Sciences at Arizona State University, and Professor Edgar A. Arriaga and Dr. Gregory G. Wolken from the Department of Chemistry at University of Minnesota. In addition, I would like to thank Dr. Fernanda Camacho-Alanis for her help with SEM imaging.

For the materials presented in Chapter 4, I would like to thank co-authors Professor Edgar A. Arriaga and Katherine Muratore from the Department of Biochemistry, Molecular Biology and Biophysics at University of Minnesota. Additionally, I would like to thank Dr. Fernanda Camacho-Alanis for her help with photolithograpy.

For the materials presented in Chapter 5, I would like to thank Katherine Muratore for providing the isolated mitochondria sample. I also would like to thank Daniel Mieritz and Professor Don Seo from the School of Molecular Sciences at Arizona State University for instructing me in the use of the DLS instrument as well as offering the time and help with the measurements.

For the materials presented in Chapter 6, I would like to thank Professor Yixin Shi from the School of Life Sciences at Arizona State University for providing the *Salmonella typhimurium* samples.

Finally, I would like to thank all my fellow graduate students and lab mates from Alexandra Ros lab for their assistance and fruitful discussions during all these years.

TABLE OF CONTENTS

Page

CHAPTER

APPENDIX Page

LIST OF TABLES

Table Page

LIST OF FIGURES

Figure Page

CHAPTER 1

INTRODUCTION

Separation and fractionation of micron- and sub-micron sized particles is important for the development of nanoparticle-based applications as well as for biological studies, since effective isolation methods are required to study biologically important species such as cells, organelles, or large genomic DNA. In addition, revealing the heterogeneity of particular bio-species through subpopulation analysis may allow novel insights into biochemical pathways inducing malfunction and eventually disease.

Among the research of organelles, the study of mitochondria is important due to its significant contribution to many cellular functions such as energy production, metabolism, cellular signaling, and apoptosis [1-3]. Mitochondria have intrinsic heterogeneous sizes and morphologies suggesting the existence of mitochondrial subpopulations dividing into normal mitochondria of about 0.1 – 1 μm in diameter [4, 5] and atypically sized giant mitochondria (> 1 μm) [4]. The latter have been observed in models of aging and in tissue of various pathological states such as neurodegeneration [6-8], metabolic disorders [9-11], and myopathies [12, 13]. In addition, the formation of cristae and the relation between the ultrastructure as observed in giant mitochondria and diseases are reviewed in Zick *et al.* [14] in detail. All these studies have suggested that such size heterogeneity may be an important factor associated with disease initiation and progression. Therefore, reliable and effective techniques allowing size-based subpopulation analysis of organelles are demanded.

Conventional fractionation or isolation methods can separate a particular organelle from cell lysate and they are typically based on size and density such as differential centrifugation [15, 16], density gradient centrifugation [16-19], and flow field-flow fractionation [20]. Other techniques for sample purification have also been developed [21, 22] including electromigration methods such as free flow electrophoresis (FFE) [19, 23-25], micro-FFE [26], isoelectric focusing [27], capillary electrophoresis [28], and dielectrophoresis (DEP) [29, 30]. In addition, immunomagnetic isolation of mitochondria has also been reported [31]. However, these methods are mainly focused on isolating mitochondria from cell cytoplasm and are generally not capable of subpopulation fractionation. Thus, methods that can distinguish and separate subpopulations of organelles based on their size are yet to be developed.

As size-based subpopulation analysis is in demand, employing non-intuitive and novel migration mechanisms is thus suggested. Micro- and nanofluidic devices in combination with the tailored integration of structured elements, fluid and force fields (thermal, electric, dielectrophoretic, magnetic) have been shown to evoke novel migration mechanisms [32], which cannot occur on the macroscale. Prominent examples are ratchets and Brownian motors capable of directed transport of nanoparticles or even molecules [33, 34]. Another demonstration is the phenomenon absolute negative mobility (ANM), in which particles can be transported in directions opposite to an average force [35-38]. The ANM phenomena seems counter-intuitive, however, it obeys the laws of physics and results from non-equilibrium conditions created by a periodic driving force and nonlinear elements (created through obstacles in a microfluidic structure). The coexistence of ‘normal’ migration and migration in the direction opposite to an average force for differently sized particles can be exploited for separation.

Most ratchets or ANM systems require some source of randomness which is delivered by the Brownian motion of biomolecules or nanoparticles. For separation purposes, such methods are however poorly suited for most realistic fractionation devices since the Brownian diffusion of particles in the target size range is intrinsically slow. Moreover, in the case of ANM the integration of geometrical traps requiring microstructured features similar in size to micro- or nano-particles of interest is required. Hence, further miniaturization to nm-sized particles is technically challenging.

DISSERTATION WORK METHODOLOGY

This dissertation is organized into seven main chapters. After this introductory chapter, Chapter 2 provides a brief description of the theories involved in the numerical simulations and experiments. Chapter 3 describes the iDEP migration and trapping of polystyrene beads and isolated mitochondria in both DC and low-frequency AC fields in a tailored microfluidic device, followed by the DEP-based fractionation of mitochondria subpopulations by a microfluidic sorter and the validation of the sorting experiment by numerical simulations. Chapter 4 describes the development and application of a non-linear symmetric insulator-based device as a tool for the separation of micron and sub-micron particles. Deterministic ANM was realized with the integration of periodically driven electrokinetic and dielectrophoretic forces, which was proved by the numerical modeling and then demonstrated experimentally by employing polystyrene beads. In this chapter, a novel waveform was also suggested to induce dANM for sub-micron sized particles and a demonstration with mitochondrial sample was shown. Chapter 5 presents the velocity profiles quantified for the dANM-migration-induced mitochondria and sub-micron polystyrene beads. The separation of sub-micron sized beads by dANM was also demonstrated experimentally. It was then validated by the numerical modeling process. Chapter 6 presents the preliminary DEP study of *Salmonella typhimurium*. Finally, Chapter 7 provides suggestions for future work based on the current results presented in this dissertation.

CHAPTER 2

BACKGROUND AND THEORY

ELECTROOSMOSIS

In the microfluidic device, the transportation of sample can be realized by the electroosmotic flow (EOF) [39]. As for a device made of glass and polydimethylsiloxane (PDMS), oxygen plasma treatment generates silanol groups (Si-OH) on the PDMS surface which are ionizable in aqueous solution [40]. The de-protonation process leads to negative charges on the surface and thus attracts counterions (*i.e.* cations) from the solution while anions are repelled away. Some counterions are directly attached to the PDMS or glass surface, forming an immobile layer which is termed Stern layer. Loosely associated to the Stern layer is the diffuse layer which also mainly contains cations. In this layer, ions diffuse freely under the influence of electrostatic attraction and thermal diffusion. Stern layer and diffuse layer together are termed electrical double layer (EDL). As depicted in Figure 2-1(a), the electric potential ψ at the solid surface, *i.e.* ψ_{wall}, depends on the surface charge density. Then, ψ decreases linearly across the Stern layer and drops exponentially across the diffuse layer and extending into the bulk solution. At an infinite point in the bulk solution to the solid surface, ψ becomes zero, *i.e.* $\psi_{bulk} \rightarrow 0$ as $x \rightarrow \infty$. The thickness of EDL is defined as the Debye length (λ_D) which can be expressed as [41]:

$$\lambda_D = (\frac{\varepsilon_m RT}{2F^2 cz^2})^{1/2} \qquad (2-1)$$

where F denotes the Faraday's constant, c is the electrolyte concentration, z is the electrolyte valence, R is the gas constant and T is the temperature. ε_m is the medium permittivity:

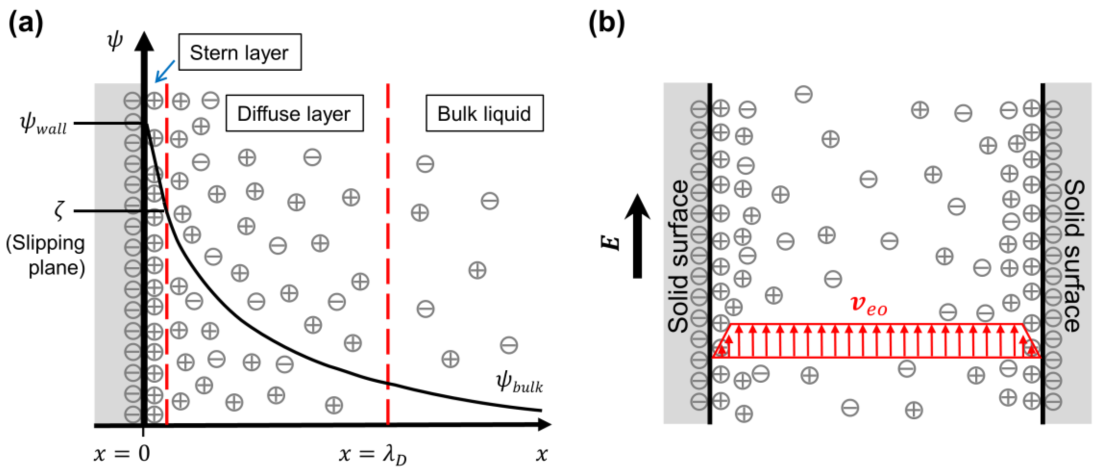

Figure 2-1. Schematics of electric double layer (EDL) and the mechanism of electroosmosis. (a) The solid surface is negatively charged, thus some cations from the aqueous solutions adsorb on the solid surface and form an immobile layer (Stern layer). In the second layer adjacent to the Stern layer, ions are loosely attached and can diffuse freely, thus this layer is termed the diffuse layer. The electric potential ψ decreases linearly across the Stern layer and drops exponentially across the diffuse layer. The thickness of EDL is defined as the Debye length, λ_D. The potential at the slipping plane is the zeta potential, ζ. (b) Schematic of the flat EOF velocity profile arising at negatively charged solid surfaces of a straight channel upon the application of an external electric field (not to scale). The velocity is uniform throughout the cross section but drops quickly to zero at the interface.

$$\varepsilon_m = \varepsilon_{r,m}\varepsilon_0 \qquad (2-2)$$

where $\varepsilon_{r,m}$ is the relative permittivity of the medium and ε_0 is the permittivity of vacuum. λ_D is typically within the nanometer range.

The interface of the Stern layer and the diffuse layer is a slipping plane which separates the potentially moving fluid from the Stern layer. The potential at the slipping plane (Figure 2-1(a)) is termed as the zeta potential (ζ) which is dependent on the Debye length [41]:

$$\zeta = \frac{\lambda_D \sigma}{\varepsilon_m} \qquad (2-3)$$

where σ is the charge density at the shear surface.

Upon the application of an external electric field ($\boldsymbol{E}$) along the longitudinal direction of a straight channel, the net charges in EDL start to move and consequently lead to the liquid motion in channel. The resultant flow exhibits a flat profile which is uniform throughout the cross section but drops quickly to zero at the Stern-diffuse layer interface (Figure 2-1(b)). The electroosmotic (EO) velocity, $\boldsymbol{v}_{eo}$, is defined by the Smoluchowski equation [39, 42]:

$$\boldsymbol{v}_{eo} = \frac{\boldsymbol{E}\varepsilon_m \zeta}{\eta} \qquad (2-4)$$

where η is the viscosity of the medium.

The EO mobility, μ_{eo}, is defined as the EO velocity over unit field strength [42]:

$$\mu_{eo} = \frac{\boldsymbol{v}_{eo}}{\boldsymbol{E}} \qquad (2-5)$$

In a straight microfluidic channel, the EO velocity can be calculated by the distance L the fluid has travelled during the time t when certain potential V is applied across this distance:

$$\boldsymbol{v}_{eo} = \frac{L}{t} \qquad (2-6)$$

and

$$\boldsymbol{E} = \frac{V}{L} \qquad (2-7)$$

Substitution of Eq. $(2-6)$ and $(2-7)$ into Eq. $(2-5)$ yields:

$$\mu_{eo} = \frac{L^2}{Vt} \qquad (2-8)$$

which can be used to determine the EO mobility in a straight microfluidic channel.

ELECTROPHORESIS

Electrophoresis is the motion of charged particles relative to the stationary liquid when an electric field is applied (Figure 2-2) [43]. The electrophoretic (EP) force, $\boldsymbol{F}_e$, on a particle with charge q can be expressed as:

$$\boldsymbol{F}_{ep} = q\boldsymbol{E} \qquad (2-9)$$

Based on the Stokes drag law, the drag force ($\boldsymbol{F}_d$) on a spherical particle is given as [44]:

$$\boldsymbol{F}_d = 6\pi\eta r(\boldsymbol{u} - \boldsymbol{v}) \qquad (2-10)$$

where r is the particle radius, $\boldsymbol{u}$ is the fluid velocity, and $\boldsymbol{v}$ is the particle velocity. When EP force is balanced with the drag force on the particle, the EP velocity $\boldsymbol{v}_{ep}$ can thus be derived:

$$\boldsymbol{v}_{ep} = \boldsymbol{u} - \boldsymbol{v} = \frac{q\boldsymbol{E}}{6\pi\eta r} \qquad (2-11)$$

Therefore, particles differing in the charge-to-size ratio can be separated by electrophoresis. The EP mobility μ_{ep} can thus be expressed as [43]:

$$\mu_{ep} = \frac{\boldsymbol{v}_{ep}}{\boldsymbol{E}} = \frac{q}{6\pi\eta r} \qquad (2-12)$$

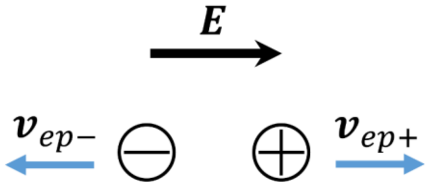

Figure 2-2. Schematic of the mechanism of electrophoresis. Arrows depict the migration directions of charged particles along (positive charge) or opposite to (negative charge) the electric field direction.

Electroosmosis and electrophoresis together can be termed as electrokinesis. When an electric field is applied to a straight microfluidic channel containing an aqueous suspension of negatively-charged particles, a positive EOF and electrophoresis (EP) of the particle induce the apparent velocity $\boldsymbol{u}$:

$$\boldsymbol{u} = (\mu_{eo} - \mu_{ep})\boldsymbol{E} = \mu_{ek}\boldsymbol{E} \qquad (2-13)$$

where μ_{ek} represents the electrokinetic mobility.

DIELECTROPHORESIS

Dielectrophoresis (DEP) is the motion of polarizable particles in a non-uniform electric field (Figure 2-3) [45]. It is governed by the polarization of a particle – which could be either charged or neutral - and the surrounding medium in which it is suspended. DEP theory has been comprehensively reviewed in several articles such as Pethig [46]. Briefly, in order to induce DEP as a migration effect, a system which can generate an inhomogeneous electric field is constructed, such as a pair of electrodes of different configurations (Figure 2-3) or a non-linear array of insulating posts in a microfluidic channel (Figure 4-1(b)). Electric field gradients are thus created in the space between the electrodes when a voltage is supplied or around the insulating bodies upon the application of potentials in the microchannel reservoirs.

The arising DEP force, $\boldsymbol{F}_{dep}$, on a spherical particle can be expressed as [47, 48]:

$$\boldsymbol{F}_{dep} = 2\pi r^3 \varepsilon_m f_{CM} \nabla \boldsymbol{E}^2 \qquad (2-14)$$

where f_{CM} represents the Clausius-Mossotti factor [44, 46-48]:

$$f_{CM} = \frac{\varepsilon_p - \varepsilon_m}{\varepsilon_p + 2\varepsilon_m} \qquad (2-15)$$

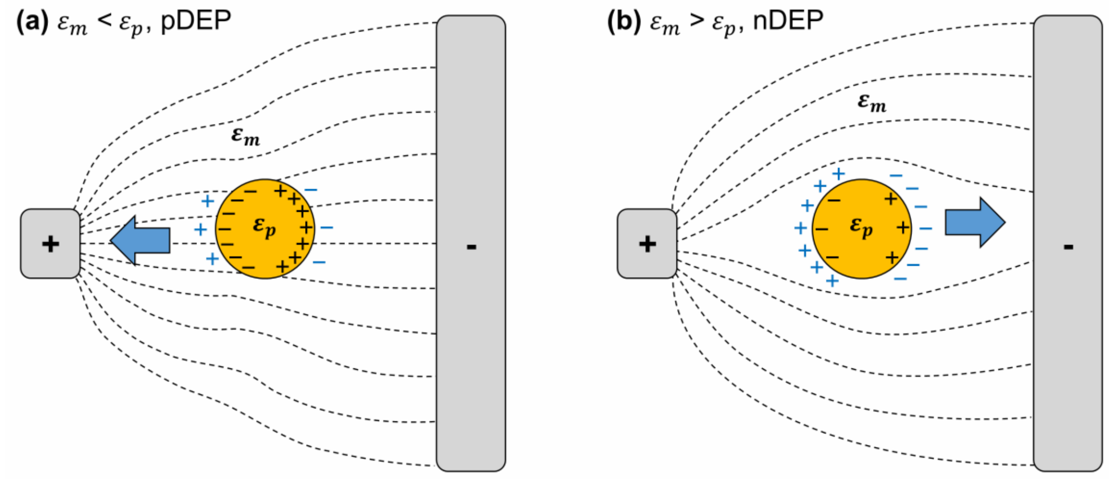

Figure 2-3. Schematics of the mechanism of dielectrophoresis for a polarizable particle (orange dot) in a non-uniform electric field created by two electrodes of different geometries. Electric field lines are presented by the black dash lines pointing from positive charges to negative charges. (a) The particle is more polarizable than the medium and it moves towards the region of high electric field gradient, representing positive DEP. (b) The particle is less polarizable than the medium and it moves towards the region of low electric field gradient, showing negative DEP. The polarities of the electrodes can be switched while the DEP migration direction of the particle solely depends on ε_m and ε_p.

where ε_p is the particle permittivity which can be calculated according to a single shell model (Figure 2-4) [47]:

$$\varepsilon_{p,1shell} = \varepsilon_{mem}\left[\frac{\left(\frac{d_{mem}+r_{cyto}}{r_{cyto}}\right)^3 + 2\left(\frac{\varepsilon_{cyto}-\varepsilon_{mem}}{\varepsilon_{cyto}+2\varepsilon_{mem}}\right)}{\left(\frac{d_{mem}+r_{cyto}}{r_{cyto}}\right)^3 - \left(\frac{\varepsilon_{cyto}-\varepsilon_{mem}}{\varepsilon_{cyto}+2\varepsilon_{mem}}\right)}\right] \qquad (2-16)$$

where $\varepsilon_{p,1shell}$ represents ε_p when using the above equation. d_{mem} and r_{cyto} represent the thickness of the membrane and the radius of the cytoplasm, respectively. The sum of d_{mem} and r_{cyto} equals to the particle radius r. ε_{mem} and ε_{cyto} are the permittivity of the membrane and that of the cytoplasm, respectively.

The Clausius-Mossotti factor f_{CM} governs the dielectrophoretic properties of suspended particles apart from their size. When ε_p is greater than ε_m, f_{CM} is positive, thus

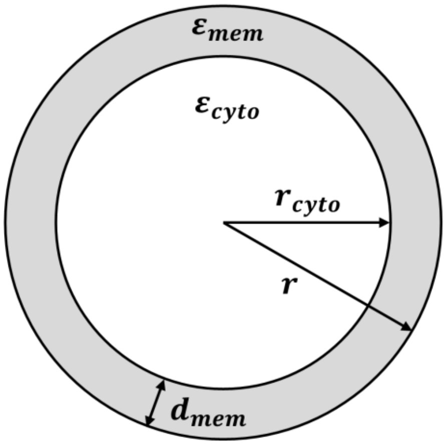

Figure 2-4. Single-shell model for a membrane-covered spherical particle. The thickness of the membrane is d_{mem} and the radius of the cytoplasm is r_{cyto}. The permittivity of the membrane and that of the cytoplasm are represented by ε_{mem} and ε_{cyto}, respectively.

positive DEP (pDEP) behavior is exhibited in which particles are attracted to the regions of high $\nabla \boldsymbol{E}^2$ (Figure 2-3(a)). Conversely, when ε_p is less than ε_m rendering f_{CM} negative, a repulsion from the regions of high $\nabla \boldsymbol{E}^2$ occurs and the corresponding migration and trapping behavior is termed negative DEP (nDEP) (Figure 2-3(b)).

In DC and low-frequency AC conditions (<50 kHz), f_{CM} can be approximated as [47, 48]:

$$f_{CM} = \frac{\sigma_p - \sigma_m}{\sigma_p + 2\sigma_m} \qquad (2-17)$$

where σ_m is the conductivity of the medium which can be measured by a conductivity meter. σ_p is the conductivity of the particle which can be approximated from Eq. $(2-16)$ at DC conditions:

$$\sigma_{p,1shell} = \sigma_{mem}\left[\frac{\left(\frac{d_{mem}+r_{cyto}}{r_{cyto}}\right)^3 + 2\left(\frac{\sigma_{cyto}-\sigma_{mem}}{\sigma_{cyto}+2\sigma_{mem}}\right)}{\left(\frac{d_{mem}+r_{cyto}}{r_{cyto}}\right)^3 - \left(\frac{\sigma_{cyto}-\sigma_{mem}}{\sigma_{cyto}+2\sigma_{mem}}\right)}\right] \qquad (2-18)$$

where $\sigma_{p,1shell}$ represents σ_p when using the above equation. σ_{mem} and σ_{cyto} are the membrane conductivity and the cytoplasmic conductivity, respectively. Thus, the DEP force at low frequencies can be estimated by the conductive properties of the particle and the suspending medium.

When the DEP force on a spherical particle is balanced with the drag force on the particle, *i.e.* $\boldsymbol{F}_{dep} = \boldsymbol{F}_d$, the DEP velocity $\boldsymbol{v}_{dep}$ can thus be derived [44, 49]. Combining Eq. $(2-14)$ with Eq. $(2-10)$ results in:

$$\boldsymbol{v}_{dep} = \boldsymbol{u} - \boldsymbol{v} = \frac{r^2\, f_{CM}\, \varepsilon_m}{3\eta} \nabla \boldsymbol{E}^2 \qquad (2-19)$$

The contribution of the DEP force to the migration of a particle can also be expressed by the DEP mobility μ_{dep} and the electric field gradient $\nabla \boldsymbol{E}^2$ [44]:

$$\boldsymbol{v}_{dep} = \mu_{dep} \nabla \boldsymbol{E}^2 \qquad (2-20)$$

The DEP mobility μ_{dep} can thus be calculated by [49]:

$$\mu_{dep} = \frac{r^2\, f_{CM}\, \varepsilon_m}{3\eta} \qquad (2-21)$$

According to the above equation, when the medium in which the particle is suspended is considered as homogeneous, μ_{dep} is dependent on the radius r for a spherical particle. However, the shape of a sample may not be perfectly spherical. Thus, the variations in the size and shape originating from a sample population could result in different μ_{dep} values. In addition, μ_{dep} also depends on the Clausius-Mossotti factor f_{CM} which involves the conductivity of the particle σ_p (Eq. $(2-17)$). Since σ_p relates to the size, the effective surface area and the ionic properties of a particle [46, 50], μ_{dep} could also be influenced by these factors.

NON-EQUILIBRIUM MIGRATION PROCESSES

According to Newton's second law, upon the application of a net force in an equilibrium system without any geometrical obstacles, particles accelerate towards the direction of the net external force. This movement of particles is termed "normal response" in the context of this thesis (Figure 2-5(a)). However, if the system is far from thermal equilibrium, a migration direction of particles opposite to the applied force could be induced in addition to the normal response, resulting in the ratchet effects (Figure 2-5(b)) [51]. Furthermore, if a net motion against the net external force of any direction is induced (Figure 2-5(c)), it is called absolute negative mobility (ANM) [35]. The distinctive difference between the two non-equilibrium migration processes is that when the net force ($\boldsymbol{F}_{av}$) is zero, a particle undergoing a ratcheting migration mechanism has a non-zero velocity while the velocity of a particle exhibiting ANM is zero (Figure 2-5(b) and (c)).

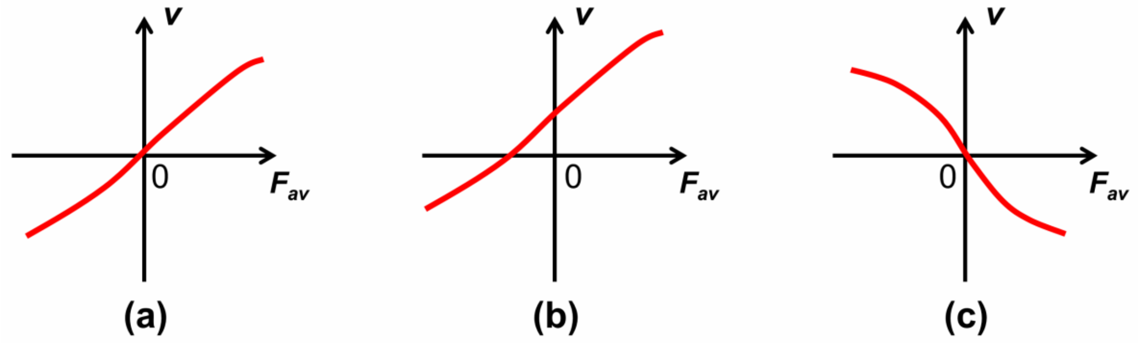

Figure 2-5. Normal migration and non-equilibrium migration processes. (a) A particle showing normal response is accelerated in the direction of the net external force. (b) A particle undergoing a ratcheting process can migrate in the direction opposite to the net applied force. It has a non-zero velocity when the net applied force is zero. (c) A particle exhibiting ANM migrates oppositely to the net external force of any direction. Compared to the ratcheting process, the velocity of the ANM process is zero when the net force is zero.

The ratcheting and ANM migration processes are counter-intuitive, yet they still obey the laws of physics. Their features can be explained by the respective structures employed. As in an unsymmetrical structure shown in Figure 2-6(a) for a ratcheting process, when the net driving force $\boldsymbol{F}_{av}$ equals to zero, a particle firstly moves from left to right in the first half period and passes around an obstacle by thermal diffusion (turquoise solid line). In the second half period, the particle moves to the left and is trapped at the flat side of a triangle (pink dash line). When the whole period ends, the net migration distance of the particle is not zero, thus resulting in the non-zero velocity of the particle undergoing a ratcheting process at zero $\boldsymbol{F}_{av}$.

More specifically, ratchet effects refer to the directed transport under non-equilibrium conditions in periodic systems with broken spatial symmetry [51]. The migration direction of a particle showing a ratchet effect relates to the orientation of the broken geometry of the structure (Figure 2-6(a)). If the orientation of the geometry is reversed or the directions of the forces in the two half periods are switched, the ratchet effect vanishes because the condition for a stable trapping in the half period with a larger external force disappears (Figure 2-6(b)). Note that “broken” is used to describe the entire geometric structure layout; it does not mean the individual element in the structure (such as the triangular obstacles in Figure 2-6(a) and (b)) cannot be symmetric. In fact, several applications employing ratchet effects exploited symmetrical obstacles which were arranged to realize the broken symmetry as a tool for inducing the directed migration of particles [51-54].

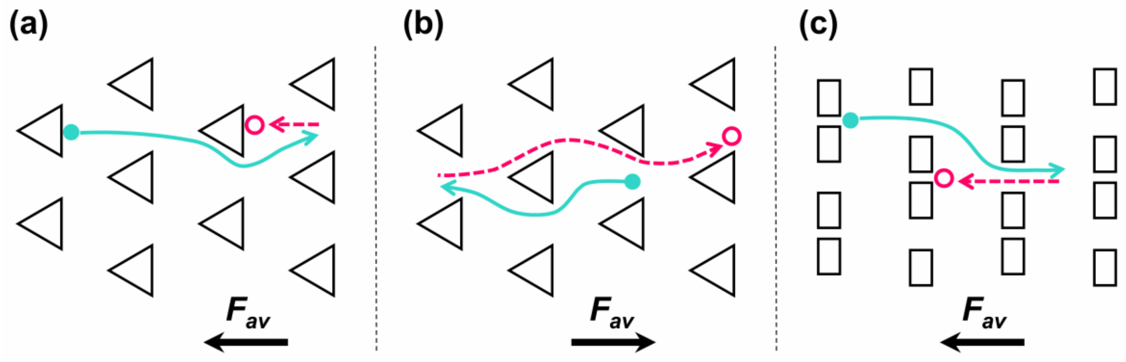

Figure 2-6. Schematics of the mechanisms of ratcheting and ANM migration processes. External forces are applied in the horizontal direction. The magnitude of the force in the 1st half driving period is small compared to that in the 2nd half period. The direction of the resultant net driving force ($\boldsymbol{F}_{av}$) in a complete period is indicated by the black arrow. The start and the end positions of a particle in a complete driving period are represented by a turquoise dot and a pink circle, respectively. The trajectory and migration direction of a particle is indicated by a turquoise solid line and arrow in the 1st half period and then a pink dash line and arrow in the 2nd half period. If the particle travels less than 1 spatial period in a complete driving period, neither a ratchet effect nor an ANM migration could be induced. This situation is thus not discussed here. In (a) and (b), the tips of the triangular obstacles are facing left and the flat sides are facing right, constructing an oriented unsymmetrical structure. In (a), a particle moves to the right and passes around the tip of a triangle in the 1st half period. While in the 2nd half period, the particle moves to the left and gets trapped at the flat side of the triangle. This results in a net migration of the particle pointing to the right while $\boldsymbol{F}_{av}$ is to the left. Note that this result could still be achieved even when the forces in the two half periods have the same magnitude, thus leading to a non-zero velocity at zero $\boldsymbol{F}_{av}$. In (b), a particle moves to the left in the 1st half period and may escape the flat side by thermal diffusion. In the 2nd half period, the particle moves to the right and passes around the tip(s) of the triangle(s) because the trapping at those positions is not stable. The resultant net migration has the same direction as $\boldsymbol{F}_{av}$, showing the normal response. Such oriented migration of the particle shown in (a) and (b) is due to the broken spatial symmetry of the structure, which leads to the feature of the ratcheting process differing from ANM. (c) The rectangular obstacles make up for a non-linear symmetrical structure. The small gap is smaller than any particle size employed in the structure. In the 1st half period, a particle may escape the small gap by thermal diffusion. But it will be trapped by the small gap when moving back from right to left in the 2nd half period because it does not have enough time to diffuse due to a larger velocity caused by the larger external force. This results in a net migration of the particle in the direction opposite to $\boldsymbol{F}_{av}$, exhibiting ANM. If $\boldsymbol{F}_{av}$ changes direction, this conclusion still applies due to the symmetry of the structure.

The other non-equilibrium process, ANM, was first realized in experiment by exploiting micron-sized colloidal particles of which Brownian motion is significant [36-

38]. A non-linear but symmetric structure was utilized with the application of an AC signal overlaid with a DC offset, creating the non-equilibrium conditions. The small gap as shown in Figure 2-6(c) is also called a geometric “trap” which has a dimension smaller than any employed particle size in the structure. When a small external force (such as $U_{dc} - U_{ac}$) is applied in the 1st half period, a particle migrates with the slow flow. When it encounters a small gap, whether it could pass around the trap or not depends on its diffusion coefficient, which relates to the particle size. Thus, within the same time, a small particle can diffuse for longer distance perpendicularly to the flow direction as compared to a large particle with a low diffusivity, leading to a successful escape from the trap for the small size while the large particle is more likely to be trapped. In the 2nd half period when the external force becomes large (such as $U_{dc} + U_{ac}$), the particle accelerates and has less time to diffuse. So, trapping occurs for the particle once it hits on a small gap regardless of the particle size. Therefore, after a complete driving period, a small particle may migrate towards a direction opposite to the net external force $\boldsymbol{F}_{av}$ which results in the ANM process (Figure 2-6(c)), while a large particle tends to migrate to the direction of $\boldsymbol{F}_{av}$. Note that when $\boldsymbol{F}_{av}$ is zero, a particle will migrate for the same distances in the two half periods due to the symmetry of the structure, resulting in a zero net migration distance at zero $\boldsymbol{F}_{av}$.

CHAPTER 3

INSULATOR-BASED DIELECTROPHORESIS STUDY OF MITOCHONDRIA

INTRODUCTION

As an important organelle participating in many cellular functions [1-3], mitochondria display a wide range of sizes plausibly resulting from the coexistence of subpopulations [4]. According to the studies over the past few decades, the abnormally enlarged giant mitochondria may be associated with disease or aging [6-13]. Therefore, a proper subcellular separation method to distinguish and harvest various sizes of mitochondria is needed to elucidate the role of this organelle in cellular functions.

Conventional strategies to separate and prepare mitochondria fractions are based on either size and density such as differential centrifugation [15, 16], density gradient centrifugation [16-19], and flow field-flow fractionation [20], or charge-dependent methods such as free flow electrophoresis [19, 23-25], isoelectric focusing [27], and capillary electrophoresis [28]. In addition, immunomagnetic isolation of mitochondria has also been reported [31]. However, these methods are mainly focused on isolating mitochondria from cell cytoplasm and few have considered the separation of mitochondrial subpopulations [26].

Here, a novel method to manipulate mitochondria in a microfluidic device, namely by their dielectrophoretic properties, is proposed. To accomplish this, the dielectrophoretic migration of isolated mitochondria was investigated under DC and low frequency AC conditions, which was then applied to fractionate mitochondria into various size groups using a microfluidic sorter.

Dielectrophoresis (DEP) is an electric field gradient-based technique allowing the manipulation of polarizable particles in an inhomogeneous electric field [45]. In the case where DEP is the dominating force, particles can be trapped in regions where electric field gradients establish. In conjunction with other transport phenomena, concentration of particles into streams or separation can also occur [55, 56]. Most commonly, traditional DEP applications focus on the use of electrodes to evoke electric field gradients [57, 58], as utilized with a variety of biological samples, namely cells [59, 60] and tissue [61-63]. Observed variations in the DEP response of such samples have led to techniques that can separate and distinguish cell lines such as various malignant or cancerous cells [64-66] or detect and concentrate bacteria [67, 68]. While the use of DEP for the characterization and analysis of organelles was originally suggested by Pohl [45] a few decades ago, only one DEP-based application toward organelles was found in the literature in which mitochondria were purified from cell homogenates in an electrode-based DEP microfluidic device [29].

While with electrode-based DEP (eDEP) the frequency dependence of the DEP response can be tested, the DC and low frequency DEP behavior of biological entities can also be examined with insulator-based DEP (iDEP) [49, 60, 69-72]. In iDEP, electric field gradients are generated by integrating insulating structures within a microfluidic device. Upon application of a potential difference between the ends of such a device, the insulating structures deviate electric field lines into an inhomogeneous distribution, creating electric field gradients at these locations. This method has the advantage of providing uniform electric field gradients spanning the entire microfluidic cross section, in addition to avoiding involved fabrication of embedded electrodes and reactions at electrodes within a microchannel [73].

In addition to eDEP and iDEP applications, considerable numbers of innovative DEP-based microfluidic devices have been developed to suit for various research needs over the last few years [32]. One of the techniques is contactless DEP (cDEP) in which the electric field in the main channel is evoked by a high-frequency potential applied in the side channel across a thin barrier of a dielectric material such as polydimethylsiloxane (PDMS) [74-77]. Since the sample is placed in the main channel, the direct contact between the sample and the electrodes is avoided. Moreover, this technique could advantageously prevent electrolysis and bubble formation in the main channel which potentially exist in eDEP and iDEP applications. However, due to the breakdown voltage of the dielectric barrier and in order to induce sufficient electric field gradient in the main channel, the thickness of the dielectric membrane and the voltage and frequency applied in the side channel require vigorous adjustments.

Since DEP has demonstrated large capability of being exploited to provide a new dimension of organelle separation, the manipulation of mitochondria by iDEP in the microfluidic devices is investigated. First, the dielectrophoretic properties of isolated Fischer 344 (F344) rat semimembranosus muscle mitochondria and C57BL/6 mouse hepatic mitochondria in low conductivity buffer (0.025 – 0.030 S/m) at physiological pH (7.2 – 7.4) are studied using a tailored PDMS microfluidic device. Direct current (DC) and alternating current (AC) of 0 – 50 kHz with potentials of 0 – 3000 V applied over a channel length of 1 cm are separately employed to generate inhomogeneous electric fields and establish that mitochondria exhibit negative DEP (nDEP). DEP trapping potential thresholds at 0 – 50 kHz are also determined to be weakly dependent on applied frequency and are generally above 200 V for mitochondria. Second, a separation scheme using DC potentials < 100 V to perform the first size-based iDEP sorting experiment of mitochondria is demonstrated as a potential precursor to isolating biologically relevant size fractions. Dynamic light scattering is used to analyze the size distribution of the samples collected from the sorting device and the numerical simulation based on the experimental conditions matches the sorting results well. Samples of isolated mitochondria with heterogeneous sizes (150 nm – 2 µm diameters) are successfully separated into sub-micron fractions, indicating the ability of DEP to isolate mitochondria into sub-populations based on their size.

MATERIALS AND METHODS

Chemicals

Si wafer (5 in.) was purchased from University Wafer. SU-8 2007 negative photoresist and developer were purchased from Microchem (Newton, MA, USA). (Tridecafluoro-1,1,2,2-tetrahydrooctyl)trichlorosilane (FOTS) was obtained from Gelest Inc. (Morrisville, PA, USA). SYLGARD® 184 silicone elastomer kit for polydimethylsiloxane (PDMS) was obtained from Dow Corning Corporation (Midland, MI, USA). Glass slides of 0.15 mm thickness were purchased from Electron Microscopy Sciences (Gold-Seal coverslip; Hatfield, PA, USA) and platinum wire was purchased from Alfa Aesar (Ward Hill, MA, USA). 0.87-µm-diameter polystyrene beads (FP-0852-2; ex: 470 nm, em: 490 nm) which were made using persulfate as the initiator and thus preserving negative surface charges were purchased from Spherotech (Lake Forest, IL, USA). For muscle isolation buffer, sucrose was purchased from MP Biomedicals (Solon, OH, USA), potassium chloride (KCl) and potassium phosphate (K_2HPO_4) were from Mallinckrodt

(Paris, KY, USA), tris-HCl was from Teknova (Hollister, CA, USA), ethylene glycol tetraacetic acid (EGTA) was from Amresco (Solon, OH, USA), and bovine serum albumin (BSA) was from Roche (Indianapolis, IN, USA). For liver isolation buffer, sucrose and EGTA were purchased from Sigma-Aldrich, 3-(N-morpholino)propanesulfonic acid (MOPS) was from Acros (Geel, Belgium), and tris was from Fisher (Fair Lawn, NJ, USA). For buffers used in DEP experiments, 4-(2-hydroxyethyl)piperazine-1-ethanesulfonic acid (HEPES), poly(ethylene glycol)-*block*-poly(propylene glycol)-*block*-poly(ethylene glycol) (brand name Pluronic® F108), potassium hydroxide (KOH), and sucrose were purchased from Sigma-Aldrich (St. Louis, MO, USA). Deionized water was from a Synergy purification system (Millipore, USA).

Microchip fabrication

A silicon master wafer patterned with the microfluidic structures was fabricated by photolithography as shown in Figure 3-1. In general, the wafer was firstly cleaned in piranha and was rinsed with R/O water, acetone and IPA. Then SU-8 was spin coated on the wafer at suitable rpm to reach the desired height (Figure 3-1(a)). After soft bake, the wafer was exposed to UV light through a chrome mask (Figure 3-1(b)), and post-baked. Then it was developed in SU-8 developing solution (Figure 3-1(c)). After hard bake, the wafer was silanized by FOTS to make the surface hydrophobic.

After the master wafer was made, it was followed by elastomer molding using soft lithography. Briefly, the PDMS silicon elastomer base and curing agent were mixed at a 10:1 ratio (w/w), poured onto the master wafer (Figure 3-1(d)), degassed under vacuum, and cured in an oven for at least 4 h at 80 ℃. The PDMS mold was then peeled off from the master wafer resulting in channels with a depth of 10 μm and 2-mm-diameter reservoirs were manually punched at the channel ends (Figure 3-1(e)). The PDMS mold was cleaned with isopropanol and distilled water and a glass slide was cleaned with acetone, isopropanol and distilled water in an ultrasonic bath, dried in a stream of nitrogen, and treated with oxygen plasma (PDC-001; Harrick Plasma, Ithaca, New York, USA) at high RF for 1 min. After treatment, the PDMS mold was irreversibly bonded to the glass slide (Figure 3-1(f)) to form a sealed microchannel system 1 cm in length for all DC and AC experiments.

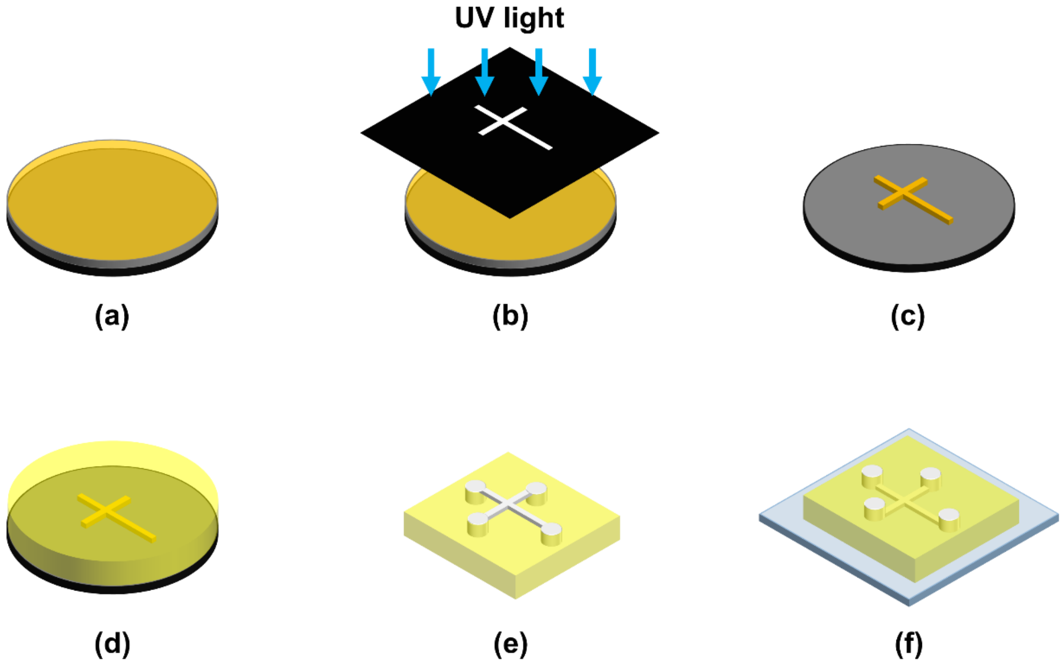

Figure 3-1. Microchip fabrication procedures. (a) The SU-8 photoresist is spin coated on the Si wafer. (b) The UV light exposes to SU-8 through a mask. (c) Exposed SU-8 forms the microfluidic structure and remains on the wafer, while the non-exposed part is rinsed away in the developing solution. (d) The PDMS is cured on the silanized wafer. (e) The PDMS mold is peeled off from the wafer and holes are punched at the end of each channel. (f) The channel side of the PDMS mold and a glass substrate are treated in oxygen plasma and they are bonded together to form an irreversible seal. The holes remain open as the inlet/outlet for the fluidic manipulation in the microfluidic structure.

Mitochondria preparation and labeling

Mitochondria were prepared at the University of Minnesota according to procedures based on mechanical homogenization and differential centrifugation from the semimembranosus muscle of a Fischer 344 (F344) rat [78, 79] (hereafter called muscle mitochondria) and from the liver of a C57BL/6 mouse [80] (hereafter called hepatic or liver mitochondria). For all procedures, animals were housed in a central specific pathogen-free facility and were treated in an optimally ethical and humane fashion using protocols approved by the Institutional Animal Care and Use Committee.

For mitochondria prepared from rat semimembranosus muscle, the muscle was excised from an anesthetized animal and placed in ice-cold muscle isolation buffer (100 mM sucrose, 100 mM KCl, 50 mM tris-HCl, 1 mM K_2HPO_4, 0.1 mM EGTA, 0.2% (w/v) BSA, adjusted to pH 7.4). All subsequent procedures for muscle and liver mitochondria isolation were performed on ice or at 4 ℃ unless otherwise noted. The sample was minced into small (~1 mm) pieces and rinsed with muscle isolation buffer to remove blood. The pieces (~1 g total) were transferred to 5 mL of muscle isolation buffer containing 0.2 mg/mL Nagarse (bacterial proteinase type XXIV, Sigma-Aldrich) and incubated on ice for 1 min. The sample was then blended with an electric homogenizer (Tissue Tearor, Biospec, Bartlesville, OK, USA) for three 20 s intervals. Muscle isolation buffer was added to a total volume of 9 mL and the sample was centrifuged at 700 ×*g* for 10 min. The pellet was discarded and this step was repeated. The supernatant was centrifuged at 10000 ×*g* for 10 min. The resulting pellet was washed twice (10000 ×*g* for 10 min) and re-suspended in 1.2 mL of muscle isolation buffer containing 10% dimethyl sulfoxide (DMSO, Sigma-Aldrich). Aliquots (50 µL each) were flash-frozen in a liquid nitrogen dewar.

For mitochondria prepared from mouse liver, the animal was anesthetized and the liver was excised. The liver was immersed in ice-cold liver isolation buffer (200 mM sucrose, 10 mM MOPS, 10 mM tris, 1.0 mM EGTA, adjusted to pH 7.4) and it was rinsed with liver isolation buffer and minced into small (~1 mm) pieces. The pieces were rinsed, suspended in 5 mL of buffer, and transferred to a glass 15 mL Potter-Elvehjem homogenizer (Wheaton, Millville, NJ). The sample was homogenized with 3-5 strokes of a motor-driven Teflon pestle operated at 1600 RPM (Wheaton). The homogenate was centrifuged at 600 ×*g* for 10 min and the resulting pellet was discarded. The supernatant was centrifuged at 7000 ×*g* for 10 min, then the pellet was washed once with liver isolation buffer and centrifuged at 7000 ×*g* for 10 min. Mitochondria were re-suspended in 4 mL of liver isolation buffer containing 10% DMSO, divided into four aliquots, and flash-frozen in a liquid nitrogen dewar. When needed, mitochondria samples were transported on dry ice and otherwise stored in a nitrogen dewer. Samples were transferred to a -80 ℃ freezer one day prior to the experiment. Isolation buffer was stored at 4 ℃ and subjected to a 0.2 μm sterile filter before use.

Mitochondria were labeled with MitoTracker Green (Life Technologies, USA) at the time of experimentation. 1 mM MitoTracker Green stock solution in DMSO was thawed to room temperature, diluted by isolation buffer, and added to the mitochondria sample to reach a final concentration of 800 nM MitoTracker Green. The mitochondria sample was incubated at 37 ℃ with gentle shaking (300 RPM) for 15 min, then centrifuged (10000 ×*g*) at 4 ℃ for 10 min followed by removal of the supernatant. The resulting mitochondria-containing pellet was then resuspended in Buffer B (250 mM sucrose, 250 µM or 1 mM F108, 10 mM HEPES, pH adjusted to 7.2 – 7.4 with KOH, σ_m = 0.025 – 0.030 S/m).

Bead solution preparation

1 µL of 0.87-µm-diameter polystyrene beads were suspended in 500 µL Buffer B and vortexed for 10 minutes. Then the solution was sonicated for 2 hours before use.

Fluidic operations

The following general preparation was followed for both microfluidic devices shown in Figures 3-2 and 3-6. After assembly, all microfluidic channels were immediately filled with Buffer A (500 µM or 1 mM F108, 10 mM HEPES, pH adjusted to 7.2 – 7.4 with KOH) by capillarity and the chip was placed in a humid environment overnight to ensure complete surface coating with F108. Buffer A was then removed by vacuum suction, and the channels were washed with Buffer B three times and refilled by adding Buffer B to the outlet reservoirs.

DEP characterization and trapping experiments were performed using the microfluidic device shown in Figure 3-2. For this device, a PDMS holder was employed to increase the reservoir volume and provide stability for the electrodes. The holder was ~0.5 cm thick, consisting of 5 mm diameter reservoirs that matched the channel design allowing it to be reversibly placed onto the assembled chip. The prepared mitochondria sample was added to an inlet reservoir replacing Buffer B and mineral oil was added on top of the liquid layer in both reservoirs to prevent evaporation. Platinum electrodes attached to the reservoirs were connected via micro-clamps (LabSmith, Livermore, CA, USA) to either a

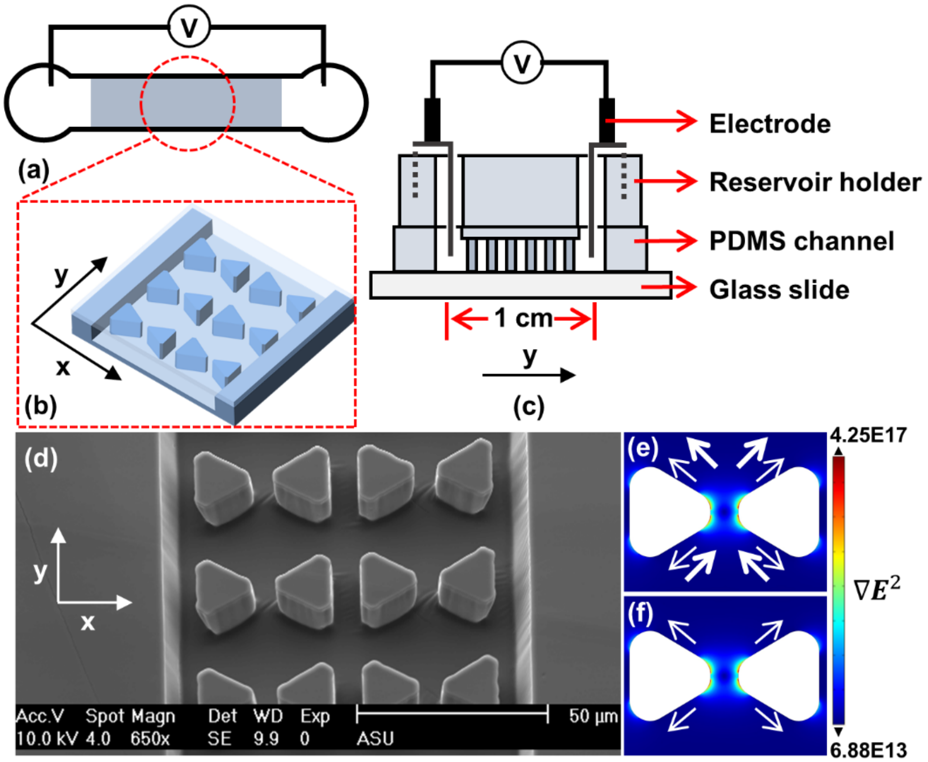

Figure 3-2. (a) – (d) Schematics of the microchip (not to scale). (a) Channel top view with shaded area indicating the post region. (b) Zoom-in of the post region. (c) Channel side cross section with PDMS reservoir holder and integrated electrodes. (d) SEM image of the post region. (e) and (f) show the numerical simulations of $\nabla \boldsymbol{E}^2$ for a post pair based on a DC experiment where 3000 V was applied across a 1-cm-long channel. Under DC conditions (e), small arrows indicate the nDEP force direction and large arrows indicate the electrokinetic forces resulting from electroosmosis and electrophoresis. Under AC conditions (f), only nDEP forces are prevalent. Note that arrow size does not represent the magnitude of the forces. For all experiments, the electric field is applied along the y-axis.

DC power supply (HVS448-6000D High Voltage Sequencer, LabSmith) commanded by Sequence software (version 1.150, LabSmith), or an AC power supply from a high voltage amplifier (AMT-3B20, Matsusada Precision Inc.) amplified from a Multifunction DAQ card (USB X Series, National Instruments, TX, USA) programmed by LabVIEW 2010 (version 10.0.1, National Instruments).

The microfluidic device shown in Figure 3-6 was employed for sorting experiments. Outlet reservoirs were filled with 5 µL of Buffer B prior to the experiment and at the beginning of the experiment, 5 µL of mitochondria sample was injected into the inlet reservoir. Positive DC potentials ranging from +20 to +60 V were applied to the inlet and negative DC potentials ranging from -20 to -60V were applied to the outlets. Sorting was performed over a duration of ~1 h and solutions were extracted from all reservoirs for size analysis.

Detection and data analysis

Fluorescence images were acquired with an inverted microscope (IX71, Olympus, Center Valley, PA, USA) equipped with a 100 W mercury burner (U-RFL-T, Olympus, Center Valley, PA, USA) and fluorescence filter set (exciter ET470/40, dichroic T495LP, emitter ET525/50, Semrock, USA). A 40× (LUCPlanFLN, NA = 0.60) objective was used to visualize the migrations of polystyrene beads and a 60× (UPLSAPO60×W, water immersion, NA = 1.20) or 100× (UPLSAPO100xO, oil immersion, NA = 1.40) objective was used to visualize the migrations of mitochondria in the microchannel. Images were captured at an interval of 100 or 150 ms using a CCD camera (for DC experiments: iXon X3, Andor Technology, Belfast, Northern Ireland; for AC experiments: QuantEM:512SC, Photometrics, Tucson, AZ, USA) and Micro-Manager software (version 1.4.7, Vale Lab, UCSF, CA, USA). The data were then analyzed with ImageJ software (version 1.47d, NIH). Note that the fluorescence emission of the beads was more intense in comparison to the stained mitochondria.

For sorting experiments, dynamic light scattering (DLS) (Spectro Size 302, Molecular Dimensions, UK) was used for size characterization of particle distributions in the inlet and each outlet. A 3 μL hanging droplet was set up in a 24-well crystallization plate and aligned to the DLS laser until a response signal was obtained. Each sample was subjected to 10 consecutive measurements lasting 20 s each. The results were combined into histograms of particle size distribution as well as signal intensity heat maps.

RESULTS

The DEP behavior of muscle mitochondria and hepatic mitochondria were tested in the device depicted in Figure 3-2. The iDEP device consists of a 1-cm-long linear channel, in which an array of triangular insulating posts is integrated. A dynamic coating with Pluronic® F108 was utilized to significantly reduce the adsorption of samples to channel walls as well as sample aggregation [42, 81, 82]. Figure 3-2(a) – (c) shows the device schematically and Figure 3-2(d) shows a scanning electron microscopy image of the post array in the microchannel. A reservoir holder was attached to the PDMS mold and defined the volume of the reservoirs accessing the inlet and outlet. Mitochondria iDEP was tested under both DC and AC conditions (up to 50 kHz). Figure 3-2(e) and 2(f) show the arising $\nabla \boldsymbol{E}^2$ around the inward facing tips of two triangular posts which represent all post pairs in the channel. Additionally, arrows indicate the direction of electrokinesis and nDEP for DC (Figure 3-2(e)) and nDEP only in the case of AC (Figure 3-2(f)). According to the single-shell model (Eq. $(2-18)$) and the literature values for mitochondria [83-86], the derived mitochondrial conductivity was estimated to be 6 × 10^{-5} S/m. With a medium conductivity of 0.025 – 0.030 S/m, a f_{CM} of -0.5 was thus applied in the simulations. The resulting $\boldsymbol{F}_{dep}$ acting on mitochondria with diameters of 150 nm to 2 µm ranges from -9.4 $\times 10^{-14}$ to -2.2 $\times 10^{-10}$ N at the post region ($\nabla \boldsymbol{E}^2_{\max}$ = 10^{17} V^2/m^3) and -9.4 $\times 10^{-16}$ to -2.2 $\times$ 10^{-12} N away from the posts ($\nabla \boldsymbol{E}^2_{\max}$ = 10^{15} V^2/m^3), exhibiting a two orders of magnitude difference.

Results of DC experiment

Mitochondria DEP was studied under DC conditions at various electric field strengths (0 – 3000 V applied across a channel length of 1 cm). A low conductivity buffer with a physiological pH similar to what was used in the previous capillary electrophoresis study on mitochondria [87] was chosen. Generally, mitochondria were observed moving away from the inward facing tips of the posts where the highest electric field gradient regions were present, indicating nDEP. An example of this behavior can be seen in Figure 3-3(a) which shows a fluorescence snapshot of muscle mitochondria under a DC field with a voltage-to-distance ratio of 3000 V/cm. Three typical mitochondria migration behaviors were observed and classified as “wiggling”, “trapping”, and “trap hopping”. Wiggling is defined as mitochondria moving in-between two adjacent post pairs along the flow direction. This behavior could result from a combination of several factors: (1) electroosmotic flow (EOF), which drives the mitochondria toward the cathode, (2) migration of mitochondria to the anode due to their negative electrophoretic mobility (μ_{ep}) at physiological pH [87], and/or (3) nDEP forces pushing the mitochondria away from the inward facing post tips. The velocity of a particle transported by the EOF and the electrophoresis is proportional to the magnitude of the electric field (Eq. $(2-4)$ and $(2-11)$). The magnitude of the DEP force is also directly proportional to the organelle size as

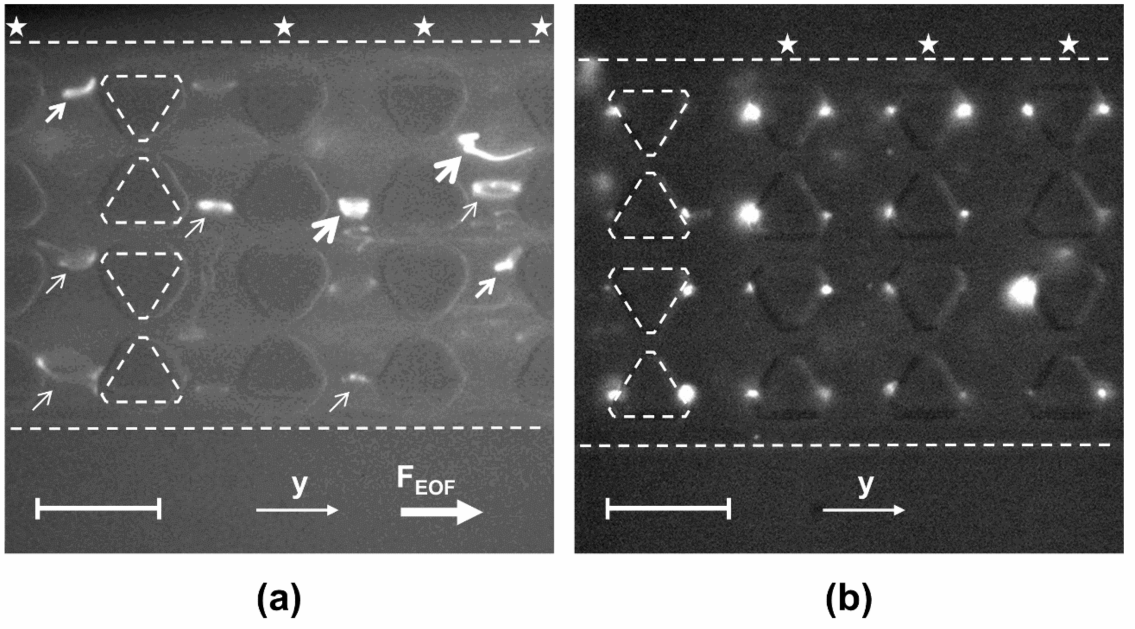

Figure 3-3. Behaviors of (a) muscle mitochondria under DC conditions at 3000 V and (b) hepatic mitochondria under AC conditions at 180 V and 50 kHz across the 1-cm-long channel. Scale bar is 30 µm. One row of posts and the channel edges are outlined in each figure; the other rows of posts are indicated by stars. In (a), the thinnest arrows point at mitochondria wiggling in-between adjacent rows of posts, the medium thickness arrows point at those trapped at the edges of posts or away from the inward facing tips of the posts (nDEP trapping), and the thickest arrows point at those migrating in-between several rows of posts quickly (trap hopping). (see Supplemental video Fig2a enhanced in [30]). In (b), AC iDEP trapping is shown. Since electroosmotic flow was suppressed under AC conditions, mitochondria were attracted toward the edges of the posts immediately when voltage was applied. (see Supplemental video Fig2b enhanced in [30]).

well as the electric field gradient (Eq. $(2-14)$). Meanwhile, the magnitude of the electric field as well as the gradient of it varies within the post array. Additionally, the local electric field lines may be distorted by the displacement of a particle if the particle size is not negligible (Figure 2-3). In this situation, the migration of the particle could induce a continuous re-distribution of the electric field lines. This could possibly alter the magnitude of the electric filed and the local field gradients around the particle, which in turn constantly influence the EO, EP and DEP forces on the particle. Therefore, mitochondria experience unbalanced forces within the post array, resulting in the wiggling behavior observed in the DC experiments.

The second phenomenon is trapping. When mitochondria were approaching a post pair, the nDEP force was large enough to repel them away to areas of lower $\nabla \boldsymbol{E}^2$ along the edges of posts, effectively trapping them. The third phenomenon, trap hopping, is in principle similar to wiggling; however, mitochondria also migrated perpendicularly to the flow direction. In this way, mitochondria could escape high $\nabla \boldsymbol{E}^2$ regions before being trapped and continue migrating longitudinally until they were randomly trapped by another post pair downstream. In real time, this appeared as though the mitochondria were hopping between post pair sections, hence the designated term. Figure 3-3(a) provides a snapshot of each of the three mitochondria migration phenomena with arrows indicating the distinct migration mechanisms occurring.

To elucidate the observed behavior for mitochondria, the DEP properties of 0.87-µm polystyrene beads were also studied as they have been demonstrated to be a good model particle for characterizing iDEP devices [49, 69, 71]. With an estimated conductivity of 0.001 S/m [88], polystyrene beads are expected to show nDEP behavior [69] under the same experimental conditions (σ_m = 0.025 – 0.030 S/m) used for mitochondria. As such, these beads provided a reference for nDEP behavior. The results of beads experiments are shown in Figure 3-4, which support the conclusion that mitochondria exhibit nDEP since the polystyrene beads resemble the migration behavior of the mitochondria when using the same conditions and microfluidic device.

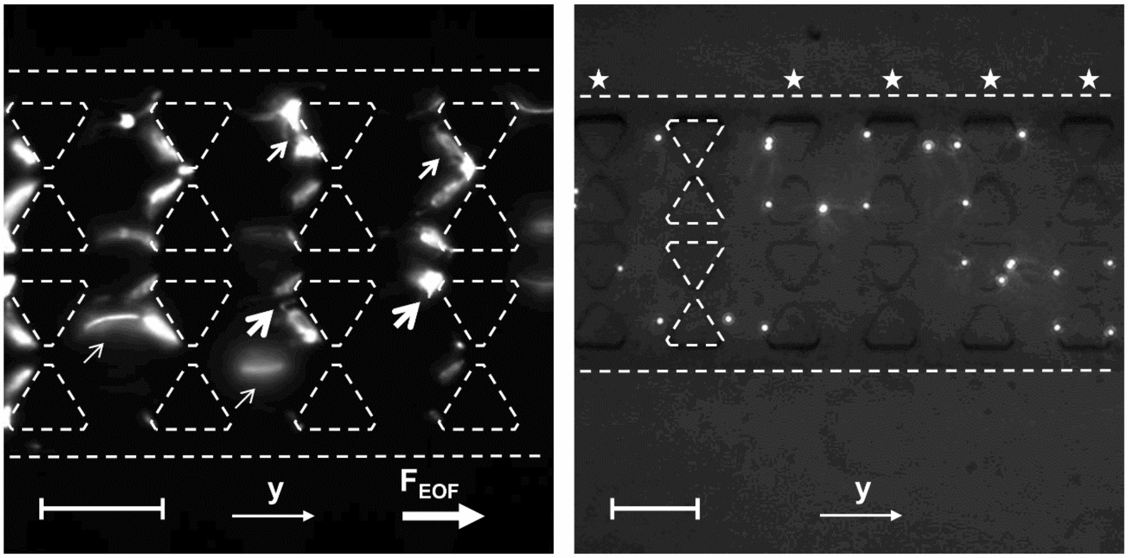

(a) (b)

Figure 3-4. Behaviors of 0.87-µm polystyrene beads under (a) DC conditions at 900 V/cm and (b) AC conditions at 300 V/cm and 7.5 kHz. Scale bar is 30 µm. In (a), the thinnest arrows point at beads wiggling in-between adjacent rows of posts, medium thickness arrows point at those trapped at the edges of posts or away from the inward facing tips of the posts (nDEP trapping), and the thickest arrows point at those migrating in-between several rows of posts quickly (trap hopping). In (b), AC iDEP trapping is shown. Since electroosmotic flow was suppressed under AC, the beads were attracted to the edges of posts immediately when voltage was applied.

Results of AC experiment: trapping potential threshold vs. frequency

AC frequencies ranging from 0 to 50 kHz were tested in the same chip under varying applied potentials. As expected, the DEP trapping behavior was pronounced since the electrokinetic component was suppressed. Consequently, the migration behavior of the mitochondria showed stronger DEP trapping since the electrokinetically supported wiggling and trap hopping phenomena were suppressed. Upon the application of AC signal, mitochondria were attracted to the edges of the posts where $\nabla \boldsymbol{E}^2$ is low (Figure 3-3(b)), again indicating nDEP trapping in accordance with the DC experiments.

In addition, the potential threshold at which the mitochondria began to exhibit significant trapping behavior was studied as demonstrated in Figure 3-5(a) for AC frequencies ranging from 0 to 50 kHz in seven devices (*n* = 7) with about 100 mitochondria per potential tested. The large variation observed at each frequency, shown as error bars, is expected from the natural size distribution of mitochondria in the sample. Consequently, Figure 3-5(a) shows that trapping potential threshold for heterogeneous mitochondria is weakly dependent on frequency. Furthermore, this data was collected from highest to lowest frequency over the duration of each single experiment; therefore, a possible reason for the increasing error at low frequencies may be the longer exposure of the mitochondria to the electric field (while residing in the chip). This exposure could cause changes in their DEP properties over the course of the experiment and could also lead to mitochondria aggregation. Additionally, at low frequencies, EOF is not completely suppressed since a considerable DC component is acting in each half period of the periodic potential (as tested with an oscilloscope). This could also explain why the potential required to trap the mitochondria was somewhat higher at low frequencies compared to high frequencies. Also as a reference, the trapping potential threshold of polystyrene beads was studied under the same conditions and the results are shown in Figure 3-5(b).

Note that for both DC and AC experiments, currents never exceeded 10 µA even at the largest potentials (max. 3000 V) tested, and power dissipation is on the order of a few tens of mW (no larger than 30 mW when at the maximum applied potential 3000 V). A considerable heating and temperature rise above 37˚C within the device are thus only expected for larger potentials applied (> 100 V), such as examined by Chaurey *et al.* [89], and over long durations (several minutes to hours). If potentials are kept small, effects on

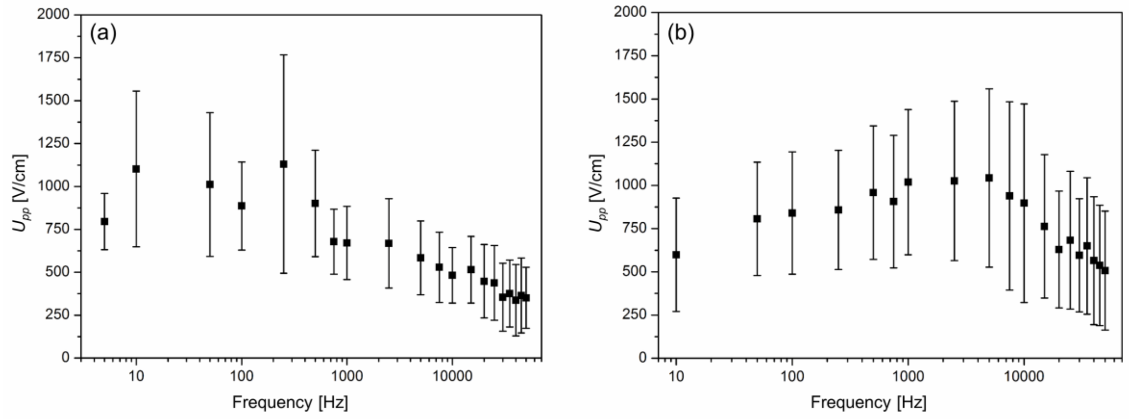

Figure 3-5. Dependence of trapping potential threshold on frequency for (a) muscle mitochondria and hepatic mitochondria (n = 7) and (b) beads (n = 7). In general, mitochondria can be trapped at applied peak-to-peak potentials above 200 V across the 1-cm-long channel and at frequencies between 0 – 50 kHz, while beads can be trapped at applied peak-to-peak potentials (U_{pp}) above 400 V under the same conditions.

mitochondria viability are expected to be marginal as examined by Nakano *et al*. [90] Therefore, other assays on viable mitochondria can be performed after iDEP experiments. Consequently, low applied potentials on the order of 100 V were used to test iDEP-based sorting for mitochondria subpopulations; the results are reported as follows. It is also noted that considerable pH gradients can occur in iDEP experiments; however, when the applied potentials are small and durations on the order of minutes are not exceeded, considerable pH variations are not expected [91].

Proof-of-principle nDEP-based sorting experiment and numerical simulation

Based on the study of mitochondria iDEP, iDEP sorting of hepatic mitochondria was investigated by using a microfluidic sorter previously developed for sorting nano beads and protein nanocrystals by nDEP [69]. A schematic of this device can be seen in Figure 3-6(a) in which six different microchannels (*I*: inlet, 2×*O*: outer, 2×*MO*: midouter, *C*: center)

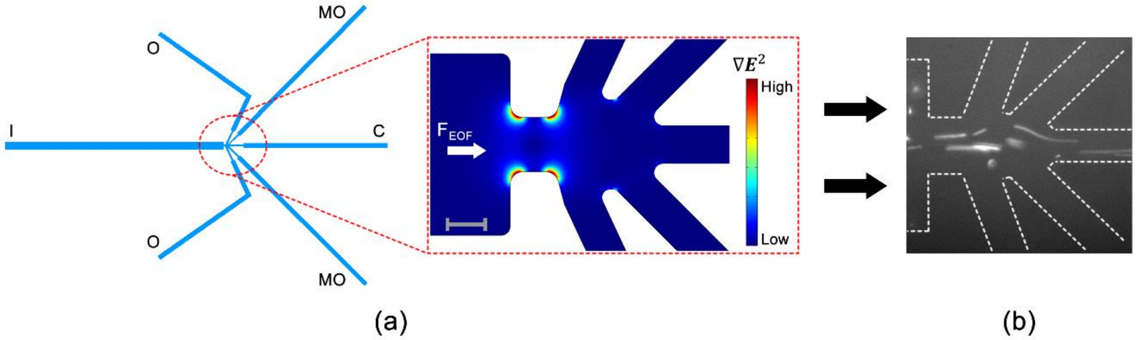

Figure 3-6. (a) Schematic of the microfluidic device employed to sort hepatic mitochondria. The device consists of one inlet channel (*I*) and five outlet channels (*O*: outer, *MO*: mid-outer, *C*: center) with reservoirs at all channel ends (not shown). The mitochondria sample is injected into the inlet reservoir and transported through the device via electroosmosis. The zoomed in region shows the constriction area where inhomogeneous electric fields are generated, creating areas of high $\nabla \boldsymbol{E}^2$ to induce DEP. Scale bar is 20 μm. (b) Fluorescence microscopy image of the constriction region during a mitochondria sorting experiment. Applied potentials are +60 V in *I*, -60 V in *C*, and 0 V in *MO* and *O*. As shown, large particles focus into the center outlet channel (*C*) due to their higher nDEP forces repelling them from areas of high $\nabla \boldsymbol{E}^2$. (see Supplemental Video Fig4b enhanced in [30]).

are employed for particle fractionation. Mitochondria of various sizes were introduced in the inlet reservoir (*I*) and DC potentials were applied to all channels to transport the organelle downstream by EOF. The zoomed in region shows a numerical simulation of $\nabla \boldsymbol{E}^2$ at the constriction area connecting the inlet to the outlets where electric field lines converge to establish an inhomogeneous electric field inducing nDEP. Areas of high $\nabla \boldsymbol{E}^2$ (red), three orders of magnitude larger than the wide inlet channel (blue), form and repel larger mitochondria with a greater $\boldsymbol{F}_{dep}$ from constriction walls, per Eq. $(2-14)$ in Chapter 2. Consequently, the sorting principle is based on the varying magnitude of $\boldsymbol{F}_{dep}$ experienced by differently sized mitochondria flowing through the device.

As a proof of principle that this sorting mechanism could be applied to mitochondria, the sorter was set up with DC voltages of +20 to +60 V in *I*, –20 to –60 V in *C*, and 0 V in *MO* and *O* (low potentials were used to reduce Joule heating effects that could potentially damage the sample). The optimal potential scheme was determined to be -60V *I*, +60V C, and 0 V *MO* and *O* in which upon entering the constriction, large mitochondria experiencing a greater nDEP force focus into the center outlet channel (*C*), as shown in Figure 3-6(b). Conversely, small mitochondria experiencing lesser nDEP forces are only marginally influenced by nDEP at the constriction and therefore can deflect into the *O* and *MO* outlet channels. Because small mitochondria can have a sub-micron size range, they are difficult to detect with optical microscopy as they are either below the resolution limit or have weak fluorescence emission indistinguishable from the background. Therefore, DLS was used to detect and quantify the size distribution of each fraction collected after ~1 h of sorting at the optimized potentials (Figure 3-7).

In the upper half of Figure 3-7, histograms are shown illustrating the detected particle size distributions in each reservoir and in the lower half, scattering intensity heat maps with respect to particle size in each reservoir are shown. Figure 3-7(a) illustrates the expected large size distribution of the injected bulk mitochondria sample ranging from ~300 nm to 2 µm diameters. Because the entire sample, namely the larger mitochondria, focuses into the center outlet, a similar distribution is seen in Figure 3-7(b). The smaller mitochondria ideally fractionate into the side outlet channels *MO* and *O*, which is shown in Figure 3-7(c) and (d) as both having sub-micron distributions. Surprisingly, an even more desirable effect is seen here as the *MO* fraction has a measured size range of ~200 – 600 nm, whereas further fractionation occurs in *O* which was measured at ~150 – 350 nm. In total, three fractions of decreasing size from *C* to *O* were obtained, indicating that the nDEP properties of mitochondria can be exploited for size-based sorting.

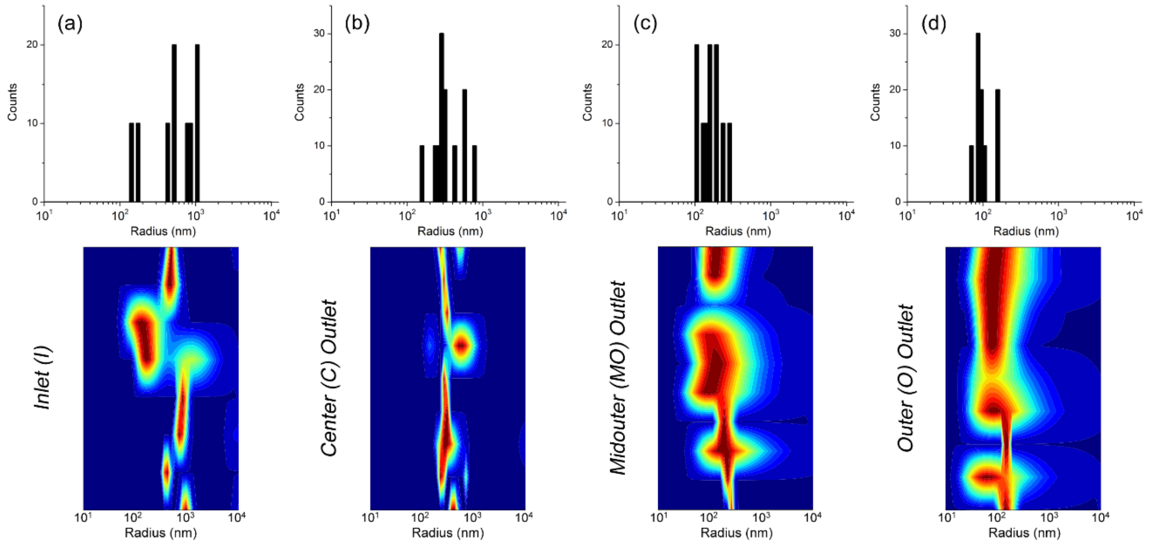

Figure 3-7. Size analysis by dynamic light scattering of the sorted hepatic mitochondria sample. The upper frame shows the histogram size distributions of detected particles and the lower frame shows the heat maps of scattering intensities with respect to particle size (blue = lowest, red = highest, y-axis spans the measurement time). (a) Size distribution of the injected inlet solution. A wide distribution (~300 nm – 2 µm diameters) is observed, qualifying the need for sorting. The smallest particles detected in other fractions are not seen due to their significantly lower scattering intensities. (b) Size distribution of the fraction collected from the *C* outlet which has the same wide distribution as the inlet since all sample particles flow here. (c) Size distribution of the *MO* fraction which is shifted towards a smaller particle size range of ~200 – 600 nm. (d) Size distribution of the *O* fraction showing a further shift towards an even smaller size range of ~150 – 350 nm. As observed, the mitochondria sample was fractionated into three size groups, decreasing from the *C* to *O* outlet channels.

Furthermore, from a typical loading of 5 µl of sample containing 10^6 mitochondria, analysis of the obtained fractions show that from a bulk mitochondria preparation, large mitochondria can be separated from small mitochondria. For an outlet reservoir, the estimated recovery is ~10^5 mitochondria per reservoir. This amount is sufficient for further analysis such as the measurement of membrane potentials [92], mitochondrial respiration [93], or proteomics studies [94].

To help establish and support this developed optimal potential scheme, the sorting experiments was simulated using *COMSOL Multiphysics 4.3* within an exact replica of the microfluidic device geometry used in the experiments. Three relevant physics were considered in the numerical model: DEP [49], electrokinesis due to EOF [49], and diffusion. This numerical method was successfully applied to the previously mentioned sorter developed to fractionate nanocrystals [69], thus the same physical model was employed and adapted to mitochondria DEP parameters. The detailed description is shown below.

Mathematically, DEP was considered by the DEP velocity ($\boldsymbol{v}_{dep}$) and mobility (μ_{dep}) as described by Eq. $(2-20)$ and $(2-21)$ in Chapter 2. Due to the mitochondria having a negligible conductivity, f_{CM} became equal to -0.5. Two representative particle sizes, 500 nm and 2 µm diameters, were simulated which gives μ_{dep} values of -7.9×10^{-21} $m^4 \cdot V^{-2}\ s^{-1}$ and -1.3×10^{-19} $m^4 \cdot V^{-2}\ s^{-1}$, respectively. To consider an electrokinetic component, the electrokinetic velocity ($\boldsymbol{u}$) and mobility (μ_{ek}) were used as described by Eq. $(2-13)$. Electrophoretic effect was considered to be negligible, therefore μ_{ep} was negated and μ_{eo} (1.5×10^{-8} $m^2 \cdot V^{-1}\ s^{-1}$ for F108 coated PDMS) dominated as μ_{ek}.

The final parameter, diffusion, was considered by the particle diffusion coefficients (*D*) calculated with the Stokes-Einstein equation (500 nm: 9.8×10^{-13} $m^2\ s^{-1}$, 2 µm: 2.5×10^{-13} $m^2\ s^{-1}$). Combining all three physics, the concentration profiles could be simulated by computing the total flux, $\boldsymbol{J}$.

$$\boldsymbol{J} = -D\nabla c + c[\boldsymbol{u}_{ek} + \boldsymbol{u}_{dep}] \qquad (3-1)$$

The system was solved at steady state, therefore:

$$\frac{\partial c}{\partial t} = \nabla \cdot \boldsymbol{J} = 0 \qquad (3-2)$$

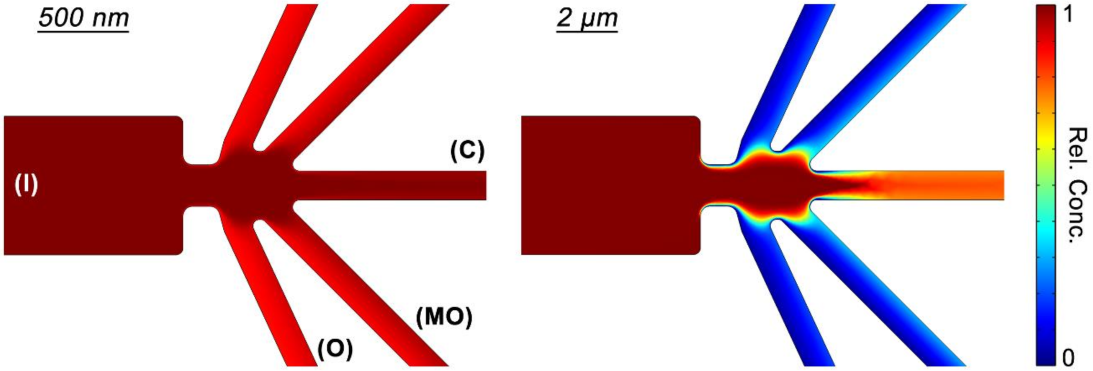

Figure 3-8. Simulated relative concentration profiles of the nDEP sorting mechanism supporting the optimized potential scheme for mitochondria sorting shown experimentally in Figure 3-6(b) (+60 V in *I*, -60 V in *C*, and 0 V in *MO* and *O*). Two representative particle sizes were studied (500 nm and 2 µm diameters). As expected, the larger particles focus into the *C* outlet whereas the smaller particles deflect into the *MO* and *O* outlets, effectively sorting and isolating them.

A medium conductivity of 0.03 S/m was applied and potentials were set to +60 V in the inlet (*I*), 0 V in the side outlets (*MO* and *O*), and -60 V in the center outlet (*C*). The *Transport of Diluted Species* module within *COMSOL* allowed for the μ_{dep} and *D* of each particle size to be input with values given above. The electric field and creeping flow driven by EOF were also calculated, which were accounted for in the overall calculation for the transport of the particles and resulted in the concentration profiles of the constriction region and encompassing channels shown in Figure 3-8.

The resulting profile of the smaller 500 nm particles illustrates complete deflection (> 90% rel. conc.) into all outlet reservoirs due to a weak influence of DEP. Under the same conditions, the corresponding profile of the larger 2-µm particles illustrates DEP driven focusing into the *C* outlet channel (> 90% focused, < 10% deflected). Consequently, these simulation results agree with expected migration trends.

CONCLUSION

In summary, the DEP properties of isolated mitochondria from Fischer 344 (F344) rat semimembranosus muscle and C57BL/6 mouse liver were studied and it was elucidated that they exhibit nDEP behavior. This was performed using a surface treated PDMS microfluidic device with DC (0 – 3000 V) and AC (0 – 50 kHz) electric fields applied across a 1 cm long channel and media with a conductivity of 0.025 – 0.030 S/m at physiological pH. The trapping potential thresholds for mitochondria at the applied frequency range were generally above 200 V and were found to be weakly dependent on frequency. These conclusions were confirmed by a model study utilizing 0.87-µm polystyrene beads known to exhibit nDEP, since their behavior within the post array was in agreement with that of the mitochondria under the same conditions. Moreover, the DEP-based sorting experiment conducted at low DC potentials successfully sorted mitochondria into various size fractions. The size range investigated is highly compatible with separations of “giant” mitochondria observed under conditions of disease and aging [4]. This is the first time that iDEP sorting of an organelle type, specifically mitochondria, has been demonstrated. Additionally, the amount of sorted mitochondria is suitable for most ensuing studies and negative effects due to iDEP manipulation are greatly suppressed due to the low potentials applied in the sorting device. Overall, this study provides important information about mitochondria under both DC and AC conditions, contributing to a foundation for future development of mitochondria subpopulation separation and applications to investigate their role in aging and disease.

CHAPTER 4

DETERMINISTIC ABSOLUTE NEGATIVE MOBILITY STUDY OF MITOCHONDRIA

INTRODUCTION

Efficient particle separation techniques in the micron- and submicron range is required for the various analytical challenges related to nanotechnology and microbiology. Based on the studies of DEP properties of polystyrene beads and mitochondria described in Chapter 3, a non-linear symmetric microfluidic structure was designed. With the new structure, an innovative method which can induce the non-intuitive, yet efficient migration mechanism absolute negative mobility (ANM) while not requiring the Brownian motion of analytes is developed. In this method, the size selectivity and the characteristic migration of ANM were induced under the periodic action of the combination of the insulator-based dielectrophoresis (iDEP) and the electrokinetically induced transport. Due to the contribution of the size-based DEP trapping force [46], the migration directions of different-sized particles were deterministic – thus termed deterministic ANM (dANM) – and tunable by the external electric field. Moreover, the geometric trap was no longer needed so that a simple photolithographic device fabrication strategy can be applied without the need of nanofabrication techniques, whereas the size selectivity for sub-µm biological species such as mitochondria is preserved.

In the present work, the realization of dANM for µm- and sub-µm sized polystyrene particles was firstly studied by numerical simulations. Regimes in which the deterministic particle migration opposite to the average applied force occurs for larger particles – a typical signature of deterministic absolute negative mobility (dANM) – were revealed, whereas normal response is obtained for smaller particles. The coexistence of dANM and normal migration was characterized and optimized in numerical modeling and subsequently implemented in a microfluidic device demonstrating at least two orders of magnitude higher migration speeds in the proof-of-principle experiments as compared to the previous ANM systems. Based on the parameters quantified from the experiments and the actual structure dimensions used, the simulations were refined and a suitable DEP mobility was thus proposed to reach a good agreement with the experiments. Furthermore, dANM was demonstrated for the mouse liver mitochondria with adequate modification to the waveform of the applied potentials, thus preserving the size selectivity for sub-μm biological species such as mitochondria.

MATERIALS AND METHODS

Chemicals

4.4- μm-diameter (FP-3065-2) and 0.9- μm-diameter (FP-0852-2) polystyrene beads which were made using persulfate as the initiator and thus preserving negative surface charges were purchased from Spherotech (Lake Forest, IL, USA). SYLGARD® 184 silicone elastomer kit for polydimethylsiloxane (PDMS) was obtained from Dow Corning Corporation (Midland, MI, USA). 4-(2-hydroxyethyl)piperazine-1-ethanesulfonic acid (HEPES), poly(ethylene glycol)-*block*-poly(propylene glycol)-*block*-poly(ethylene glycol) (brand name Pluronic® F108), potassium hydroxide, and sucrose were purchased from Sigma-Aldrich (St. Louis, MO, USA). Deionized (DI) water was from a Synergy purification system (Millipore, USA). For beads experiments, Fisherbrand® Plain

Microscope glass slides were purchased from Thermo Fisher Scientific Inc. (75 × 50 × 1.0 mm; USA). For mitochondria experiments, Gold-Seal coverslip were purchased from Electron Microscopy Sciences (48 × 60 mm, No. 1; Hatfield, PA, USA). Platinum wire was purchased from Alfa Aesar (Ward Hill, MA, USA).

Microchip fabrication

The patterns of the microstructures were designed in AutoCAD (Autodesk Inc.) and were then transferred to a chrome mask. The fabrications of the silicon master wafer and the microfluidic device were the same as described in Chapter 3.

Fluidic operations

All the dANM experiments were performed using the microfluidic device as schematically shown in Figure 4-1. After assembly, each channel was filled with solution A (0.5 mM F108 for bead experiment and 1 mM F108 for mitochondrion experiment, 10 mM HEPES, pH adjusted to 7.4 by KOH, sterile-filtered to 0.2 μm) by capillarity and the chip was placed in a humid environment overnight (16 – 24 hours) to coat all the channel surfaces with F108. Solution B (250 mM sucrose in solution A, pH 7.4, 0.03 S/m, sterile-filtered to 0.2 μm) was used to prepare the polystyrene bead or the mitochondrion solution and to rinse the channel right before use. A 0.5 cm thick PDMS holder was employed to increase reservoir volume and provide stability for the electrodes. The prepared bead or mitochondrion solution was added to an inlet reservoir and solution B to another reservoir. Mineral oil was added on top of the liquid layer in both reservoirs to prevent evaporation. Pt electrodes attached to the reservoirs were connected via micro-clamps (LabSmith, Livermore, CA, USA) to an AC power supply from a high voltage amplifier (AMT-3B20, Matsusada Precision Inc.) driven through a Multifunction DAQ card (USB X Series, National Instruments, TX, USA) programmed by LabVIEW 2014 (version 14.0, National Instruments).

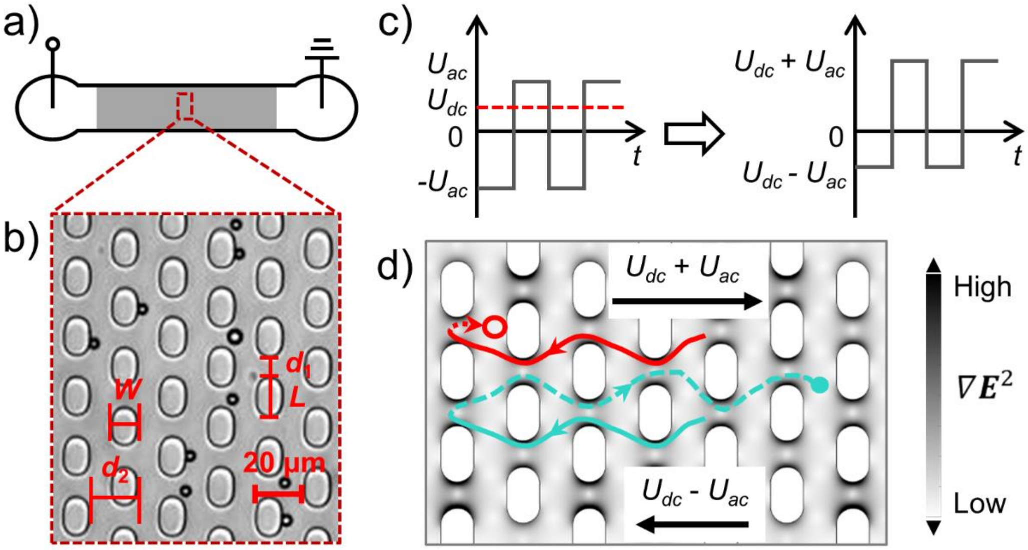

Figure 4-1. (a) Top view of the 1-cm-long channel (not to scale). The shaded area refers to the post array section in the channel. (b) Bright field microscopy image of a section of the post array region. W, L, d_1 and d_2 refer to post width, length, gap distance and row distance, respectively, and are defined in the Numerical Modeling section. The dark circles correspond to 4.4-µm polystyrene beads. (c) The combination of an AC amplitude U_{ac} and a DC offset U_{dc} results in a waveform used in both simulation and bead experiment. (d) The dANM behavior (red line) and the normal migration (turquoise line) in one driving period are shown. Particles are assumed to exhibit nDEP and are also subject to electrokinetic migration. In the 1st half period at the applied potential $U_{dc} - U_{ac}$, particles are transported to the left and the trajectories are depicted by solid lines. When particles migrate to the right in the 2nd half period at$U_{dc} + U_{ac}$, two situations occur: (1) For large DEP forces, particles are trapped near a post as indicated by the red dashed line and circle (end position of particle after one period). This situation relates to dANM, as the particle migrates opposite to $\boldsymbol{F}_{av}$. (2) For small DEP forces, particles migrate through the gaps as indicated by the turquoise dashed line and dot (end position of particle). This relates to normal migration behavior following $\boldsymbol{F}_{av}$. The surface plot shows the gradient of the electric field (see grey scale).

For the electrokinetic mobility measurement, the chip preparation was similar to the procedures for dANM experiments except that a straight channel without posts was used. Beads were introduced into the channel by capillary action, the liquid level was well balanced and subsequently a DC signal was supplied by the high voltage amplifier. The resulting bead migration was recorded with a video camera with time interval recorded by Micro-Manager software (version 1.4.7, Vale Lab, UCSF, CA, USA) as described in Detection and Data Analysis. The migration of beads was imaged at 20, 40, 60, 80 and 100 V/cm.

Preparation of bead and mitochondria suspensions

The bead solution was prepared by diluting 1 μL original bead solution from the manufacturer in 100 μL solution B. Then the beads were rinsed for three times by repeating a procedure of 1 min vortex, centrifugation at 10000*g* for 5 minutes, removing of the supernatant and re-suspension of the pellet in 100 μL solution B. After rinsing, the bead solution was sonicated for 1 hour.

Mitochondria were prepared from the liver of a four week old male C57BL/6 mouse as previously described [80]. All mice were housed in a designated clean facility and treated in accordance with protocols approved by the Institutional Animal Care and Use Committee at the University of Minnesota. The mouse was euthanized and the liver was excised and placed in 10 mL ice-cold isolation buffer (10 mM Tris, 1 mM EGTA, 10 mM MOPS, 200 mM Sucrose). All subsequent isolation steps were performed on ice or at 4 ℃ as appropriate. The liver was transferred to a Petri dish, rinsed with isolation buffer and minced into small (~1 mm) pieces using a razorblade. The liver pieces were again rinsed with isolation buffer and re-suspended in 4 mL isolation buffer and transferred to a 15 mL glass Potter-Elvehjem homogenizer tube (Wheaton, Millville, NJ). The liver was homogenized by 4 strokes of a tight-fitting motor driven Teflon pestle (Wheaton) operated at 1600 RPM. The homogenate was transferred to a 15 ml conical tube and centrifuged at 600*g* for 10 min. The supernatant was removed, divided into four 1.5 ml Eppendorf tubes and centrifuged at 7000*g* for 10min. Each pellet was washed in 1 mL isolation buffer and centrifuged at 7000*g* for 10 min. Each pellet was resuspended in 900 μL isolation buffer and transferred to cryotubes containing 100 μL DMSO and snap frozen in liquid nitrogen. Then the mitochondria samples were shipped from the University of Minnesota to Arizona State University on dry ice and stored in a nitrogen dewer when received. Sample was transferred to a -80 ℃ freezer one day prior to the experiment. 1 mM MitoTracker Green stock solution in DMSO was thawed to room temperature, diluted by solution C (100 mM sucrose, 125 mM KCl, 10 mM HEPES, 2 mM K_2HPO_4, 5 mM $MgCl_2$, pH adjusted to 7.4 by KOH, sterile-filtered to 0.2 μm) and added to mitochondria sample to reach a final concentration of 800 nM MitoTracker Green. The mitochondria solution was incubated at 37 ℃ with gentle shaking (160 RPM) for 15 min and then centrifuged (10000*g*) for 10 min. After the removal of the supernatant, the pellet was re-suspended gently in solution B followed by a 5-min centrifugation (10000*g*) step. After removing the supernatant, the resulting mitochondria pellet was re-suspended in solution B.

Detection and data analysis

Fluorescence images were acquired with an inverted microscope (IX71, Olympus, Center Valley, PA, USA) equipped with a 100 W mercury burner (U-RFL-T, Olympus, Center Valley, PA, USA) and fluorescence filter set (for 0.9-μm beads and mitochondria: exciter ET470/40, dichroic T495LP, emitter ET525/50, Semrock, USA; for 4.4-μm beads: exciter 607/36, emitter 670/39). A 20× (LUCPlanFLN, NA = 0.45) or a 40× (LUCPlanFLN, NA = 0.60) objective was used to visualize bead migration and a 60× (UPLSAPO60×W, water immersion, NA = 1.20) objective was used to visualize mitochondria migration in the microchannel. Images were captured by a CCD camera (QuantEM:512SC, Photometrics, Tucson, AZ, USA) and Micro-Manager software.

The obtained videos were then processed by ImageJ software (version 1.47d, NIH). In dANM experiments and for 4.4-μm beads at each applied potential, over 230 individual trajectories were analyzed using the MTrack2 plugin [95]. Depending on when the particle moved out/in the focus region, 1 - 9 complete periods were considered per particle. For the experiment with 0.9 μm beads, 40 trajectories of 1 - 2 complete periods for each applied potential were analyzed using the Manual Tracking plugin [96]. For mitochondria, the trajectories of 20 individual mitochondria in a complete period at the specific driving conditions were evaluated using the Manual Tracking plugin [96]. Stroboscopic images were manually generated by overlaying each image frame at corresponding locations from the same video and this procedure was done for bead and mitochondria, respectively.

For EK mobility measurement, over 100 individual trajectories for 4.4-μm beads at each DC voltage were analyzed by MTrack2 plugin [95] to obtain the migration distances over defined time intervals. After plotting the average migration velocity versus the applied DC electric field, the elektrokinetic mobility of 4.4-μm beads was obtained by calculating the slope of the least squares line, which resulted in $2.2 \pm 0.33 \times 10^{-9}\ \mathrm{m}^2 \cdot \mathrm{V}^{-1}\ \mathrm{s}^{-1}$ (Appendix A 1). This value was used in the refined simulations.

NUMERICAL MODELING

The simulations were performed using *COMSOL Multiphysics 4.4* in a non-linear spatially-periodic structure (Figure 4-1(b)). Since the particles are treated as point-like particles in the simulation, virtual walls were additionally constructed with a distance equal to the particle radius to account for specific particle sizes. The parameters used in the preliminary and the refined simulations are listed in Table 4-1. The DEP mobilities were calculated by Eq. $(2-21)$ in Chapter 2 for the respective particle sizes with the relative permittivity of the medium $\varepsilon_{r,m}$ = 80 as for water [97] and the viscosity of the medium η = 8.90 × 10^{-4} Pa s as for water. The value of f_{CM} used in the preliminary simulation is estimated to be -0.5 based on the literature value of σ_p for polystyrene [98, 99] and σ_m measured in the employed solution (0.03 S/m).

Table 4-1. Parameters used in the preliminary and the refined simulations

	Preliminary simulation			Refined simulation
Post size $L \times W$ [µm]	13.2 × 2			17 × 10
Gap size d_1 [µm]	11.8			8
Row spacing d_2 [µm]	20			20
Particle diameter [µm]	3.5	4.5	5.0	4.4
μ_{ek} [$\times 10^{-9}$ $m^2 \cdot V^{-1}$ s^{-1}]	15	15	15	2.2
μ_{dep} [$\times 10^{-19}$ $m^4 \cdot V^{-2}$ s^{-1}]	-4.1	-6.7	-8.3	-6.4

For the refined model, post geometries were matched to those in the actual experimental device and a parameter sweep was additionally performed for the DEP mobility parameter to find matching velocities in accordance with the experimental velocities. For the parameter sweep of the DEP mobility used in the refined simulation, the f_{CM} value varied from -0.08 to -0.4 corresponding to μ_{dep} from -1 to -5 $\times 10^{-19}$ $m^4 \cdot V^{-2}$ s^{-1} (not included in Table 1). The result is shown in Figure 4-4 and discussed in detail in the Results section.

Three relevant physics were considered to model particle migration: EK, DEP, and Brownian force. Firstly, by combining the static study result of the *Electric Currents* module with a rectangle and an analytic function, a tunable alternating electric field with rectangle waveform (Figure 4-1(c)) was realized representing the combination of U_{ac} and U_{dc} (Appendix A 2 and A 3). This was then coupled with the time-dependent study using the *Creeping Flow* module providing an alternating flow profile in which the electrokinetic components were considered. Based on Eq. $(2-13)$ in Chapter 2, the flow profile was obtained by the apparent velocity $\boldsymbol{u}$. Electrophoresis of particles was neglected for the preliminary simulations (results shown in Figure 4-2) and the electrokinetic component was considered through the EOF mobility μ_{eo} for F108 coated PDMS [49]. In the refined simulations (Figure 4-4), experimentally determined electrokinetic mobility μ_{ek} for 4.4 μm polystyrene beads was used. Finally, the electric field and the flow profile were additionally integrated with the DEP force ($\boldsymbol{F}_{dep}$) and the Brownian force ($\boldsymbol{F}_B$) to perform the time-dependent study with the *Particle Tracing for Fluid Flow* module. Newton's second law was utilized to solve for the instant velocity of the particle:

$$\frac{d(m_p\boldsymbol{v})}{dt} = \boldsymbol{F}_t \tag{4-1}$$

where m_p is the particle mass and $\boldsymbol{F}_t$ stands for the total force applied on the particle at time t. The particle trajectory was then visualized by solving Eq. $(2-10)$ and Eq. $(4-1)$ time-dependently:

$$\boldsymbol{F}_{d_{(t)}} = 6\pi\eta R(\boldsymbol{u}_{(t)} - \boldsymbol{v}_{(t-1)}) \tag{4-2}$$

and

$$\frac{m_p(\boldsymbol{v}_{(t)}-\boldsymbol{v}_{(t-1)})}{\Delta t} = \boldsymbol{F}_{d_{(t)}} + \boldsymbol{F}_{dep_{(t)}} + \boldsymbol{F}_{B_{(t)}} \tag{4-3}$$

where t = 1, 2, …, *etc*. Note that at the first time step (t = 1) particles were released with zero initial velocity $\boldsymbol{v}_{(0)}$. $\boldsymbol{F}_{dep_{(t)}}$ was calculated by Eq. $(2-14)$ in Chapter 2 with $\nabla\boldsymbol{E}^2$ at the current particle position.

For the particle sizes used in this study, the Brownian force $\boldsymbol{F}_B$ was negligible and had no influence on dANM, as expected for this deterministic migration effect. For comparison, numerical modeling was performed with the same model but without Brownian motion contribution, which then resulted in similar results (see Appendix A 4). However, it was found that particles may disappear at the borders of the structures due to zero velocity during the modeling when there was no Brownian motion contribution. Therefore, the Brownian force was still included in the modeling to decrease the events of particle vanishing.

For each simulation case, the resultant particle trajectories were used for calculating the average migration velocities. In all simulations, particle-particle interactions and the particle gravity were not considered. The time step and the period were chosen carefully to ensure each particle travelled at least one spatial period in the considered time period.

RESULTS

Mechanism of dANM and results of preliminary numerical modeling

Firstly, the microfluidic device design and the prevailing migration properties for dANM of polystyrene particles will be discussed as follows. dANM was studied in an elastomer microchannel in which an array of posts was integrated as shown schematically in Figure 4-1(a) and (b). The directed motion of different particle sizes is induced due to the interplay of electrokinetic driving and dielectrophoretic trapping. Due to the symmetry in the system, particles are on average not displaced if a periodic potential U_{ac} below the iDEP trapping threshold is applied; the average force ($\boldsymbol{F}_{av}$) acting on the particles is zero. If this periodic potential is however combined with a static offset component U_{dc} ($\boldsymbol{F}_{av}$≠0) as exemplarily shown in Figure 4-1(c), dielectrophoretic trapping may be induced and directed particle migration occurs. Particles of different sizes migrate with different velocities and in different directions. This is schematically depicted in Figure 4-1(d), displaying the migration trajectories for two particle sizes. Both particles migrate according to their electrokinetic properties in the first half of the driving period (solid lines). The conditions are set such that DEP cannot trap the particles. In the second half driving period (dashed lines), the applied potential is stronger, inducing DEP trapping, but only for the larger particle. Hence, the larger particle will be trapped, whereas the smaller particle can still migrate. Repeating this process periodically leads to the average transport of larger particles against $\boldsymbol{F}_{av}$, whereas smaller particles respond in the direction of $\boldsymbol{F}_{av}$.

To characterize the conditions where dANM occurs, numerical modeling was firstly employed. The contributing factors giving rise to particle migration under dANM regimes are electrokinesis (bulk electroosmotic flow and particle electrophoresis) as well as DEP. Various combinations of U_{ac} and U_{dc} were tested as well as post array geometries in order to find the threshold parameters under which normal and dANM particle responses exist. Initially, 3.5-μm and 5-μm particle sizes were investigated in this regime. Figure 4-2(a) shows the characteristic signature of dANM for the 5-μm particles as apparent in a negative velocity for positive U_{dc} offset. In other words, the 5-μm particles are transported against $\boldsymbol{F}_{av}$ in a regime of +/- 225 V/cm U_{dc} offset, an AC amplitude of 275 V/cm and 0.625 Hz. In contrast, 3.5-μm beads show 'normal' behavior as they migrate in the direction of $\boldsymbol{F}_{av}$.

Interestingly, dANM was observed for the larger particles (5 μm) under the coexistence of normal migration for the smaller particles (3.5 μm). This is contrary to what was previously reported in the literature [36] since in the Brownian motion based mechanism smaller particles show ANM while larger sizes migrate in a normal manner. This results from the difference in the trapping mechanism. Previously, ANM was induced by utilizing geometric traps which particles need to avoid via random Brownian motion during the periodic driving. The smaller the particles, the more readily they avoid a trap and thus show ANM in contrast to larger particles of which the Brownian motion is not sufficient to induce migration around a geometric trap. As contrast, trapping in dANM occurs when the dielectrophoretic force is large enough to trap a particle while smaller particles are not affected. Note that the dielectrophoretic force scales with the cube of the

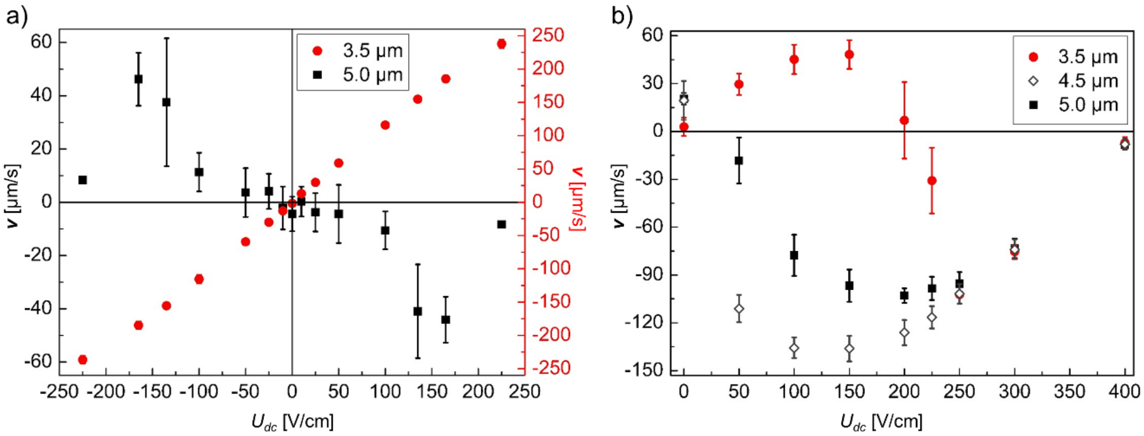

Figure 4-2. Numerical modeling results revealing regimes of dANM vs. DC offset. Particle diameters of 3.5, 4.5 and 5.0 µm are represented by solid circles, hollow diamonds and solid squares, respectively (the number of tracked particles varies from 4 to 20 due to the vanishment of particles at the channel walls during simulation as mentioned in Numerical Modeling). The error bars represent the standard deviations of the velocities as obtained at each applied potential. (a) For U_{ac} = 275 V/cm and $|U_{dc}| < U_{ac}$, 5-µm particles always show dANM, while 3.5-µm particles show normal migration due to the weaker DEP trapping force. (b) For U_{ac} = 450 V/cm and $U_{dc} < U_{ac}$, 5.0- and 4.5-µm particles show dANM. 3.5-µm particles show normal behavior at U_{dc} < 200 V, whereas dANM is induced when larger DEP trapping forces act for U_{dc} > 200 V. For small DC offsets, 4.5-µm particles migrate faster than 5.0 µm particles because smaller sizes experience less strong DEP force in the first half of the driving period $(U_{dc} - U_{ac})$.

particle radius. As a consequence, the size-ANM relationship is reversed in dANM as compared to ANM.

The second important result is that a maximum dANM velocity of ~50 µm/s was observed (Figure 4-2(a)). This average velocity is three orders of magnitude larger as compared to ANM velocities for comparable µm-sized particles [100]. This is advantageous for further separation and fractionation applications exploiting this counter-intuitive migration phenomenon. Note that particles suspended in a 100 µm × 100 µm section could be effectively transported and collected at the extreme ends of this section in an overall time of ~2 seconds. Additionally, due to the dielectrophoretic trapping mechanism, a large size selectivity (~R^3) is induced, which can be exploited in future devices for separation and fractionation. Moreover, the combination with iDEP allows the tuning of dANM driving parameters to sub-µm particle sizes without the need of nanofabrication technology, which will be demonstrated below.

Further, the dependency of dANM on the amplitude of U_{ac} was investigated as well as the selectivity for a third particle size. Figure 4-2(b) shows the velocity vs. U_{dc} response for U_{ac} of 450 V/cm for 3.5-µm, 4.5-µm and 5-µm particles. Two major observations can be made: First, due to the augmented amplitude, larger DEP forces are induced thus causing dANM for 3.5-µm particles at U_{dc} > 200 V/cm. Second, in the range of 50 V/cm < U_{dc} < 200 V/cm, all three particles show differing average velocities indicating the potential to exploit this regime for separations. The two larger particles show negative (but distinct) while the 3.5-µm particles show positive velocities. In addition to these major observations, it was noted that 4.5-µm particles migrated faster than 5 µm particles at U_{dc} < 200 V/cm. From a detailed analysis of the simulated trajectories, it was found that this effect was due to the first half of the periodic driving when $U_{dc} - U_{ac}$ was acting. In this phase, DEP slowed down the overall migration and induced slightly larger acting DEP forces for the larger particles. The second half of the driving period ($U_{dc} + U_{ac}$) did not contribute to this behavior since trapping forces were large enough for both species in this situation that trapping occurred as soon as particles encountered any nearby posts. This reversal in size dependence of dANM only occurs, when DEP forces influence the first half driving period as observed for U_{ac} = 450 V/cm.

Proof-of-principle dANM experiment with polystyrene particles

Next, the occurrence and regimes of dANM were investigated in experiments to examine the migration behavior predicted in the numerical model. A microchannel exhibiting a post array as featured in Figure 4-1 was fabricated with PDMS and the migration of 0.9- μm and 4.4- μm-diameter polystyrene beads in aqueous solution buffered at pH 7.4 was observed. Similar periodic driving parameters as in the simulations were employed and the average velocity of particles was evaluated by individual particle tracking. Figure 4-3 shows the obtained average migration velocities for both particle sizes. Note that only for the larger particles negative U_{dc} offset values were tested for consistency with the numerical modeling since the physical principles contributing to dANM are not dependent on the sign of U_{dc} (see Figure 4-2(a)). As shown in Figure 4-3(a), a dANM signature is apparent for the 4.4- μm beads in a range of 50 V/cm < U_{dc} < 225 V/cm, whereas 0.9- μm particles show normal behavior. The stroboscopic image inserted in Figure 4-3(a) is an example of the dANM migration of the 4.4-μm bead in a complete driving period during which $\boldsymbol{F}_{av}$ points to the left while the net migration of the bead is to the right. Figure 4-3(b) indicates the corresponding experiment with U_{ac} of 450 V/cm, similarly showing dANM. Both experiments (Figure 4-3) clearly indicate the occurrence of dANM similarly to what was predicted.

Several factors, however, differ from the numerical model. First, the maximum dANM velocity amounts in ~5 μm/s for the 4.4- μm beads which is two orders of magnitude larger than previously reported for ANM with similar bead sizes [100], however slower than observed with the numerical model (Figure 4-2). This could be attributed to an overestimation of the dielectrophoretic trapping component and an underestimation of the

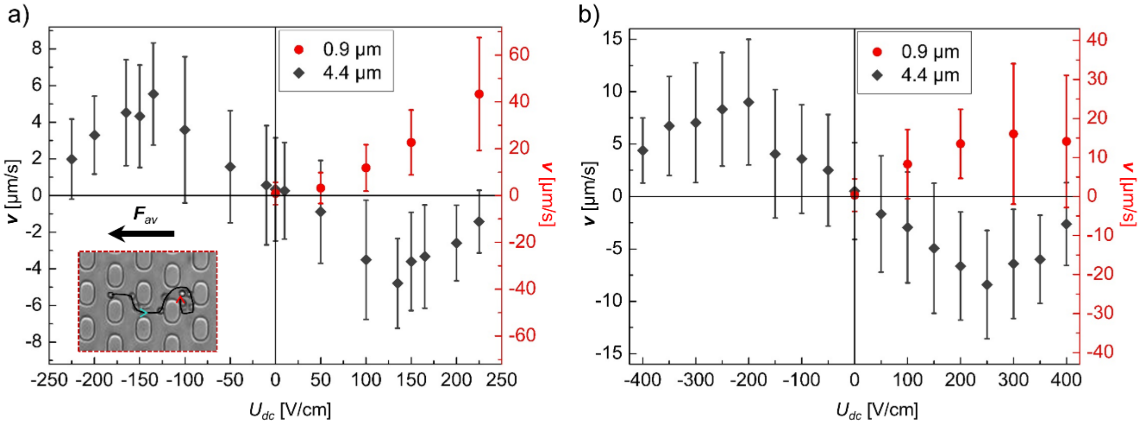

Figure 4-3. Experimental results of migration velocity vs. DC offset. Diameters of 0.9 and 4.4 µm are represented by solid circle and solid diamond, respectively. The error bars represent the standard deviations of the velocities as obtained at each applied potential from tracking over 230 particle trajectories for 4.4 µm beads and 40 trajectories for 0.9 µm beads. (a) U_{ac} = 275 V/cm and $|U_{dc}| < U_{ac}$. (b) U_{ac} = 450 V/cm and $|U_{dc}| < U_{ac}$. For both (a) and (b), the dANM behavior of 4.4-µm beads was significant while 0.9 µm beads migrated 'normally' following $\boldsymbol{F}_{av}$. The inserted stroboscopic image in (a) shows the trajectory of a 4.4 µm bead in a complete driving period at U_{dc} = -135 V/cm. At $-U_{dc} + U_{ac}$, the bead moved along the depicted trajectory following the turquoise arrowhead. At $-U_{dc} - U_{ac}$ it was trapped at the position marked by the red arrowhead. This results in the dANM migration of the bead since its net migration is to the right while the average $\boldsymbol{F}_{av}$ points to the left.

electrophoretic component of the beads in the model (which will be further discussed below). Second, the experimentally measured velocities exhibit increased error compared to the simulations even though a larger amount of beads has been analyzed with particle tracking (over 230 particle trajectories) than was released in the numerical simulation (20 particles per offset). This could be caused by the heterogeneity in size and potentially surface charge of the employed beads, which are intrinsic parameters of the commercially obtained polystyrene beads.

Refined numerical simulation with experimental conditions

Since the experimentally observed maximum dANM velocities were smaller than obtained with the numerical model, the parameters employed in the numerical model were revisited. The major driving force leading to transport of the particles through the post array is related to the electokinetic migration in the respective phases of the periodic driving. Thus the apparent electrokinetic mobility of 4.4-µm beads was determined by experiment and analyzed via particle tracking. The resulting μ_{ek} value is tabulated in Table 1. It was then employed for a refined simulation. In addition, the dielectrophoretic mobility of the polystyrene beads was adapted. Since the beads have a size distribution which could result in different μ_{dep}, the μ_{dep} values for the 4.4-µm beads were varied exemplarily in the model calculations (Figure 4-4).

Figure 4-4 represents an overview of this parameter sweep. Represented are 5 U_{dc} offset values for μ_{dep} of -3, -4, and -6.4 $\times 10^{-19}$ $m^4 \cdot V^{-2}$ s^{-1} corresponding to variations in the Clausius-Mossoti factor f_{CM} in Eq. $(2-21)$. At U_{dc} = 135 V/cm where the maximum dANM velocity was found, the corresponding velocities for μ_{dep} of -1, -2, and -5 $\times 10^{-19}$ $m^4 \cdot V^{-2}$ s^{-1} are additionally shown. Furthermore, the experimentally observed dANM velocities are overlaid in Figure 4-4 (solid diamond). This parameter sweep indicated that the model coincides excellently with the observed velocities at μ_{dep} between -3 and -4 $\times 10^{-19}$ $m^4 \cdot V^{-2}$ s^{-1}. Second, for $\mu_{dep} < -4 \times 10^{-19}$ $m^4 \cdot V^{-2}$ s^{-1} or $\mu_{dep} > -3 \times 10^{-19}$ $m^4 \cdot V^{-2}$ s^{-1} the maximum velocities are reduced and the dANM effect is less prominent. Moreover, for μ_{dep} of -1 $\times 10^{-19}$ $m^4 \cdot V^{-2}$ s^{-1} normal behavior is observed, *i.e.* a positive velocity. The latter observation clearly supports the characteristic selectivity mechanism in this dANM

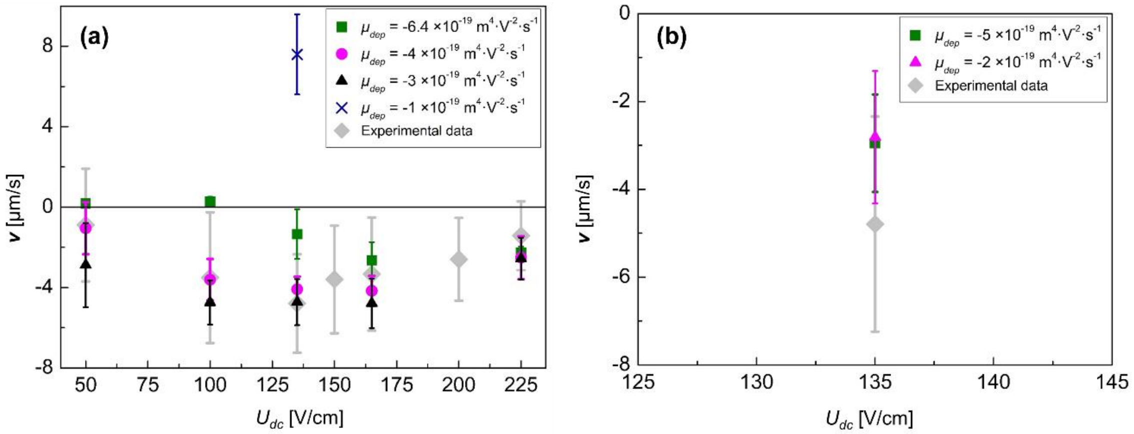

Figure 4-4. (a) Migration velocity vs. DC offset obtained from the refined simulation for 4.4 µm particles at U_{ac} = 275 V/cm and $U_{dc} < U_{ac}$. μ_{dep} of -6.4 ×10^{-19} m^4 ·V^{-2} s^{-1} (solid square) results in much slower velocities than the experimental data (solid diamond) at U_{dc} ≤ 135 V/cm while μ_{dep} of -1 ×10^{-19} m^4 ·V^{-2} s^{-1} (cross symbol) even showed normal behavior. The best match of the parameter sweep of μ_{dep} with the experimental data was found at μ_{dep} between -3 (solid triangle) and -4 ×10^{-19} m^4 ·V^{-2} s^{-1} (solid circle). (b) Migration velocity obtained from the refined simulation for 4.4-µm particles at U_{ac} = 275 V/cm and U_{dc} = 135 V/cm. Represented here are the velocities at μ_{dep} of -2 (solid triangle) and -5 ×10^{-19} m^4 ·V^{-2} s^{-1} (solid square) which are reduced comparing to the experimental data (solid diamond), indicating less prominent dANM effect. The number of tracked particles varies from 9 to 19 due to the vanishment of particles during simulation as mentioned in Numerical Modeling.

approach: If the DEP forces are too weak and can no longer trap a particle (in the phase where $U_{dc} + U_{ac}$ act), the dANM effect vanishes.

dANM demonstration for mitochondria

To further exploit the size selectivity of dANM and to extend its application on biological samples, driving forces suitable to induce dANM for mouse liver mitochondria were designed. Since iDEP force in DC mode was too weak to induce large enough trapping force for the much smaller mitochondria, it was enhanced through the overlay with an AC component in the kHz range as iDEP trapping at AC mode was previously investigated [30]. The modified waveform for dANM driving is represented in Figure 4-

5(a). Briefly, a low DC potential (U_{dc1}) was employed in the 1st half period, which provided the driving force for all mitochondria while the DC-induced DEP trapping force was negligible. In the second half period, an AC component (U_{ac_high}) was utilized and overlaid with a DC component (U_{dc2}). The frequency and amplitude of U_{ac_high} can be adjusted to suit the need for trapping a target particle size – here mitochondria. This combination of the potentials in the two half driving periods essentially represents a dANM case with a low frequency U_{ac} driving force and U_{dc} offset similar to the bead experiments. The only difference results in the trapping force induced through U_{ac_high}.

Based on the previous DEP study of mitochondria [30] and the current microfluidic structure (Figure 4-1(b)), U_{ac_high} was chosen with an amplitude of 700 V/cm and a frequency of 30 kHz to induce trapping in the second half driving period. Potentials of

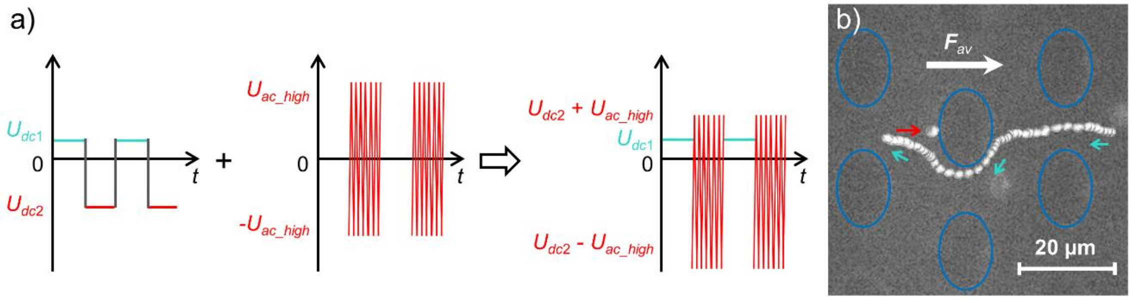

Figure 4-5. (a) The waveform applied for dANM experiments with mitochondria: The typical dANM U_{ac} driving (here indicated through U_{dc1} and U_{dc2} on the left) is combined with an AC component U_{ac_high} to obtain the waveform shown on the right. To distinguish the two half driving periods, the potential applied in the first half period is displayed in turquoise and that applied in the second half period is red. (b) The stroboscopic image shows the trajectory of a fluorescently labeled mitochondrion in a complete driving period. During the application of U_{dc1}, the mitochondrion moved in the direction indicated by the turquoise arrows. In the second half period, when $U_{dc2} + U_{ac\_high}$ was applied, the mitochondrion was trapped at the position pointed at by the red arrow. This results in dANM behavior of the mitochondrion since its net migration is to the left while the average driving force $\boldsymbol{F}_{av}$ dominated by its electrophoretic mobility points to the right. The blue ovals indicate the insulating posts in the channel.

U_{dc1} = 20 V/cm and U_{dc2} = -30 V/cm were chosen to induce dANM with each half period lasting 10 seconds. The resultant migration of mitochondria showed dANM behavior. Figure 4-5(b) depicts a trajectory of a mitochondrion in a complete driving period in form of a stroboscopic image, clearly showing the dANM signature. Under these conditions, the dANM velocity was evaluated to be -2.90 ± 0.90 μm/s for mitochondria in the same order of magnitude as obtained with μm-sized microparticles as demonstrated above. In addition, there were a few mitochondria showing normal migration, indicating that for those special cases the DEP trapping force induced by U_{ac_high} was not strong enough compared to the driving force by U_{dc2}. Interestingly, these mitochondria appeared smaller in size indicating that smaller mitochondria show a normal migration behavior whereas larger species exhibit dANM. This example demonstrates the potential of dANM for size-based separation of organelles, which is promising for sub-population analysis and separation of abnormally sized organelles.

CONCLUSION

In this work, the first design study for dANM and the experimental realization of this deterministic counter-intuitive migration phenomenon were demonstrated with colloidal particles and mouse liver mitochondria. The size selectivity of this novel migration technique is ideally suited for separation and fractionation, and it allows steering of analytes into opposite directions and at different rates. A microfluidic post array in which dANM can be evoked was successfully developed and suitable parameter selection of the driving forces was demonstrated through numerical modeling and in experiment. Note that the only tuning parameter is the dielectrophoretic component for given electrokinetic and intrinsic sample contributions. By employing µm- and sub-µm sized polystyrene microbeads, the occurrence of dANM was proved to be in excellent agreement with the numerical model. As quantified from the experiments, an intrinsic advantage of dANM lies in the two orders of magnitude improved average migration velocities of polystyrene beads as compared to the existing ANM approaches [100] and up to four times larger magnitude to ratchet approaches [51], which is favorable for future separation or fractionation applications. In addition, the here presented dANM approach can be readily realized with standard photolithographic and soft lithographic techniques and allows dANM for sub-µm species via the adjustment of the DEP trapping forces though variation of the externally applied potentials. As proof-of-principle, the realization of dANM for mouse liver mitochondria was shown and it represented the first experimental application of an ANM migration mechanism for a bioparticle. It is thus envisioned that this novel migration mechanism is applicable to a large range of separation problems in which size selectivity is required, such as in the fractionation of organelles and their subpopulations, in nanotechnological applications or as fractionation method for protein nanocrystals.

CHAPTER 5

dANM-BASED SEPARATION IN THE SUB-MICRON SIZE REGION

INTRODUCTION

In Chapter 4, the potential application of deterministic absolute negative mobility (dANM) in the separation of micron and sub-micron sized particles has been demonstrated by both numerical modeling and experiment. An overlay of a DC offset on a low-frequency AC signal was exploited to induce the periodically driven electrokinetic and dielectrophoretic effects on the migration and trapping of particles in the aforementioned approach. At the end of the results section in Chapter 4, a second waveform which overlays an AC component on a driving DC signal was additionally suggested for realizing dANM for sub-micron sized particles. An experimental demonstration of dANM realized for isolated mouse liver mitochondria was shown with this novel waveform, revealing the potential of extending the application of dANM in separation into the sub-micron size range.

In this chapter, the induced dANM migration was further quantified for the C57BL/6 mouse hepatic mitochondria with the novel waveform mentioned above. To prove that the dANM migration mechanism can be exploited as a tool for the separation in the sub-micron size range when size selectivity is needed, this novel waveform was additionally applied in the manipulation of 0.3- and 0.9-micron-diameter polystyrene beads in a microfluidic device with F108-coated all-PDMS channels. The migration velocities for each particle size were quantified. Moreover, the electrokinetic mobility of each bead size was determined in the straight microfluidic channel. Together with the voltages and the square waveform applied in the experiments, the obtained EK mobility values were subsequently employed in numerical modeling for validating the experimental results. Under these conditions, the simulations resulted in good agreement with the experimental results, exhibiting that 0.9-micron-diameter particles can migrate against the net driving force demonstrating obvious dANM behavior. Meanwhile, particles with 0.3 micron diameters showed normal response. Thus, the capability of dANM for the size-based separation problems in the sub-micron size range was demonstrated experimentally and numerically.

MATERIALS AND METHODS

Chemicals

0.3- (FP-0262-2) and 0.9-μm-diameter (FP-0852-2) polystyrene beads which were made using persulfate as the initiator and thus preserving negative surface charges were purchased from Spherotech (Lake Forest, IL, USA). SYLGARD® 184 silicone elastomer kit for polydimethylsiloxane (PDMS) was obtained from Dow Corning Corporation (Midland, MI, USA). 4-(2-hydroxyethyl)piperazine-1-ethanesulfonic acid (HEPES), poly(ethylene glycol)-*block*-poly(propylene glycol)-*block*-poly(ethylene glycol) (brand name Pluronic® F108), potassium hydroxide, and sucrose were purchased from Sigma-Aldrich (St. Louis, MO, USA). Deionized (DI) water was from a Synergy purification system (Millipore, USA). Gold-Seal coverslip were purchased from Electron Microscopy Sciences (48 × 60 mm, No. 1; Hatfield, PA, USA). Platinum wire was purchased from Alfa Aesar (Ward Hill, MA, USA).

Microchip fabrication

The pattern of the microstructure used in this chapter was described in Figure 4-1 in Chapter 4. The fabrications of the silicon master wafer and the preparation of the PDMS mold were the same as described in Chapter 3. In order to maintain the same coating effect of all the surfaces in the microchannel, the glass slide was cleaned, dried and then spin-coated at 1300 rpm for 30 seconds with PDMS mixed in the same ratio as preparing a PDMS mold. Then the PDMS-coated glass was placed in an oven for at least 4 hours at 80 ℃. The resultant PDMS layer was approximately 20 μm thick. In order to minimize the PDMS autofluorecence (see supplementary info of [101]), the PDMS mold containing the microchannels and the PDMS-coated glass were exposed to UV light for 1 hour. Then they were treated with oxygen plasma and bonded together to form a sealed microchannel system as described in Chapter 3. Since the surfaces of the microchannel were all made of PDMS, it was called the "all-PDMS" channel in the context of this thesis.

Preparation of bead and mitochondria suspensions

The preparations of the C57BL/6 mouse hepatic mitochondria and the polystyrene bead solutions were the same as described in Chapter 4.

Fluidic operations

All the dANM experiments were performed using the microfluidic device as schematically shown in Figure 4-1 in Chapter 4. After assembly, each channel was filled with solution A (1 mM F108, 10 mM HEPES, pH adjusted to 7.4 by KOH, sterile-filtered to 0.2 μm) by capillarity immediately and the chip was placed in a humid environment overnight (16 – 24 hours) to coat all surfaces with F108. Solution B (250 mM sucrose in solution A, pH 7.4, 0.03 S/m, sterile-filtered to 0.2 µm) was used to prepare the mitochondrion or the polystyrene bead solution and to rinse the channel for three times right before use. A 0.5-cm-thick PDMS holder was employed to increase reservoir volume and provide stability for the electrodes. The prepared mitochondrion or bead solution was added to an inlet reservoir and solution B to another reservoir. Mineral oil was added on top of the liquid layer in both reservoirs to prevent evaporation. Pt electrodes attached to the reservoirs were connected via micro-clamps (LabSmith, Livermore, CA, USA) to an AC power supply from a high voltage amplifier (AMT-3B20, Matsusada Precision Inc.) driven through a Multifunction DAQ card (USB X Series, National Instruments, TX, USA) programmed by LabVIEW 2014 (version 14.0, National Instruments).

For the electrokinetic mobility measurement, the experiments were done in the same chip as used for dANM experiments but in the post-free region of a channel. Once enough beads were in the focused region of a channel, the liquid level was well balanced and subsequently a DC signal was supplied by the high voltage amplifier. The resulting bead migration was recorded with a video camera with time interval recorded by Micro-Manager software (version 1.4.7, Vale Lab, UCSF, CA, USA) as described in Detection and Data Analysis. The migration of beads was imaged at 10, 20, 30, and 40 V/cm. The experiments were repeated in 3 microchannels.

Detection and data analysis

Fluorescence images were acquired with an inverted microscope (IX71, Olympus, Center Valley, PA, USA) equipped with a 100 W mercury burner (U-RFL-T, Olympus, Center Valley, PA, USA) and fluorescence filter set (for mitochondria and 0.9-µm beads: exciter ET470/40, dichroic T495LP, emitter ET525/50, Semrock, USA; for 0.3-µm beads: exciter 607/36, emitter 670/39). The migration of mitochondria in the microchannel was visualized by a 60× (UPLSAPO60×W, water immersion, NA = 1.20) objective and the bead migration was visualized by the 60× objective or a 40× (LUCPlanFLN, NA = 0.60) objective. Images were captured by a CCD camera (QuantEM:512SC, Photometrics, Tucson, AZ, USA) and Micro-Manager software (version 1.4.7, Vale Lab, UCSF, CA, USA).

The obtained videos for mitochondria or beads were then processed by ImageJ software (version 1.49, NIH). For each data point in the dANM velocity profile for mitochondria (Figure 5-1) or beads (Figure 5-3), 20 individual trajectories of mitochondria or beads per microchannel in a complete period at the specific driving conditions were evaluated using the Manual Tracking plugin [96]. The experiment was repeated in three channels for mitochondria and beads, respectively. For the stroboscopic image shown in Figure 5-2(b), the trajectories of particles with either 0.3 or 0.9 micron diameter were manually generated by overlaying each image frame at corresponding locations from the same video.

For the electrokinetic mobility measurement, the measurement at each DC signal was repeated in 3 channels. 20 individual trajectories per bead size per channel were analyzed by the Manual Tracking plugin [96] to obtain the migration distances over defined time intervals. After plotting the average migration velocity versus the applied DC electric field, the elektrokinetic mobility of 0.3-µm beads ($\mu_{ek\_0.3\_\mu m}$) and that of 0.9-µm beads

($\mu_{ek\_0.9\_\mu m}$) were obtained by calculating the slope of the least squares line (Appendix B 1). These EK mobility values were subsequently applied in the simulation.

Determination of the size distribution of mitochondria

The C57BL/6 mouse hepatic mitochondria solution was prepared as described in Chapter 4. A DLS instrument (Zetasizer Nano - ZS, Malvern, Worcestershire, UK) was used to analyze the size distribution of the sample. In general, a disposable folded capillary cell was rinsed with ethanol, distilled water, and solution B1 to remove bubbles in the chamber. Then, the mitochondria solution was carefully added into the capillary cell which was placed in the DLS instrument for the analysis. Two trials with 3 scans per trial were conducted to determine the size distribution of the mitochondrial sample (Appendix B 2). Note that the conductivity of the solution in the capillary cell was 320 μS/cm as determined by the instrument. It is the same as the conductivity of solution B1 used to condition the channels in mitochondria experiments, indicating that the rinsing step was able to condition the mitochondria solution to the same environment as in the microchannel.

NUMERICAL MODELING

The simulations were performed using *COMSOL Multiphysics 5.1*. The numerical method was successfully applied to the previous modeling of dANM induced for micron-sized particles as described in Chapter 4, thus the same physical model was employed and adapted to the new waveform and parameters (Appendix B 3). The detailed description is shown below.

The non-linear spatially-periodic structure was the same as used in Chapter 4 except that the dimensions of the virtual walls were adapted according to the particle sizes used in this chapter. Three relevant physics were considered to model particle migration: EK, DEP, and Brownian force. Mathematically, DEP was considered by the DEP velocity ($\boldsymbol{v}_{dep}$) and mobility (μ_{dep}) as described by Eq. $(2-20)$ and $(2-21)$ in Chapter 2. Due to the polystyrene having a negligible conductivity [98, 99] and σ_m measured in the employed solution (0.03 S/m), f_{CM} became equal to -0.5. Two particle sizes, 0.3-µm and 0.9-µm diameters, were simulated with μ_{dep} values of -2.48×10^{-21} $m^4 \cdot V^{-2}$ s^{-1} and -2.39×10^{-20} $m^4 \cdot V^{-2}$ s^{-1} respectively as calculated by Eq. $(2-21)$ with the relative permittivity of the medium $\varepsilon_{r,m}$ = 80 as for water [97] and the viscosity of the medium η = 8.90×10^{-4} Pa s as for water.

To consider an electrokinetic component, the electrokinetic velocity ($\boldsymbol{u}$) and mobility (μ_{ek}) were used as described by Eq. $(2-13)$. Experimentally determined $\mu_{ek\_0.3\_\mu m}$ and $\mu_{ek\_0.9\_\mu m}$ for the employed polystyrene beads (Appendix B 1) were both applied in simulation.

As for the modeling process, the static study result of the *Electric Currents* module was firstly combined with a rectangle and an analytic function, resulting in a tunable alternating electric field with rectangle waveform representing the combination of U_{dc1} and U_{dc2} (Figure 5-2(a)). The result was then coupled with the time-dependent study using the *Creeping Flow* module generating an alternating flow profile in which the electrokinetic components were considered. Note that the AC signal U_{ac_high} was not applied in this module. It is because when the AC waveform created by a sine wave and the second analytic function was added in *Creeping Flow*, the computer cannot complete the simulation. Since the symmetric fast alternating current does not contribute significantly to the electrokinetic flow profile, the AC waveform was omitted. Finally, the electric field and the flow profile were additionally integrated with the DEP force ($\boldsymbol{F}_{dep}$) and the Brownian force ($\boldsymbol{F}_B$) to perform the time-dependent study with the *Particle Tracing for Fluid Flow* module. The particle trajectory was then visualized by solving the instant velocity of a particle time-dependently (see Eq. $(4-2)$ and $(4-3)$ in Chapter 4). The AC signal U_{ac_high} was added in this module since it was the major component that induced different behaviors of particles based on their size. The effect of U_{ac_high} was verified by performing simulation with the same model but without AC waveform, which resulted in the normal migration behavior of 0.9-µm-diameter particles (Appendix B 4).

The average migration velocities were evaluated identically as described in Chapter 4. The results are shown in Figure 5-3 and discussed in detail in the Results section.

RESULTS

Quantification of dANM-induced migration velocity for mitochondria

Based on the study shown in Chapter 4, overlaying an AC component (U_{ac_high}) in the kHz range with a low DC potential (U_{dc2}) can evoke a large enough iDEP trapping force for the isolated mitochondria sample in one of the half driving periods. Meanwhile, mitochondria could migrate with the flow in the other half period when only a DC driving (U_{dc1}) was applied. Thus, dANM was successfully induced for sub-micron bio-species with the waveform shown in Figure 4-5(a).

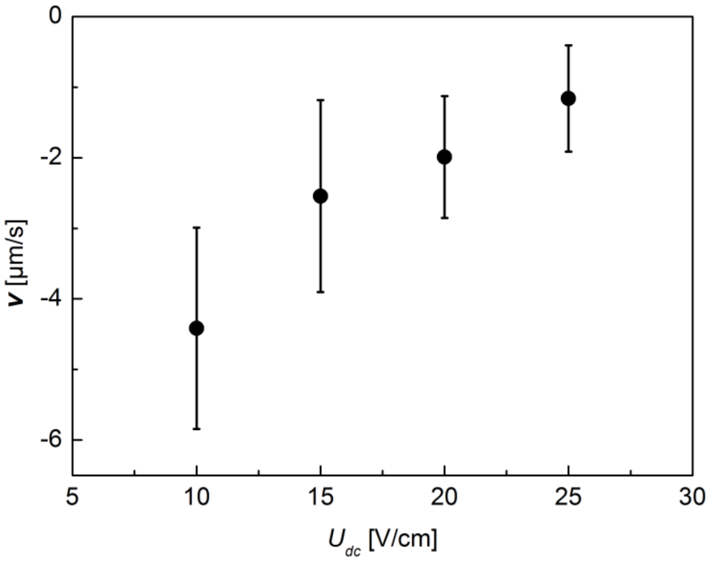

Figure 5-1. Experimental results of migration velocity ($\boldsymbol{v}$) vs. driving DC (U_{dc}) for isolated mitochondria. The error bars represent the standard deviations of the velocities obtained at each U_{dc} based on 60 individually tracked mitochondrial trajectories. At the experimental conditions, the average migration velocities of mitochondria were in the opposite direction to the applied U_{dc}, clearly demonstrating the dANM migration behavior.

In the work presented in this chapter, the microchannel integrated with a post array as featured in Figure 4-1 in Chapter 4 was employed here for the isolated mouse hepatic mitochondria suspended in pH 7.4 aqueous buffer solution. The trapping potential was chosen as U_{ac_high} with an amplitude of 800 V/cm and a frequency of 30 kHz. Periodic driving parameters of U_{dc1} = -40, -30, -20, and -10 V/cm and U_{dc2} = 60 V/cm were chosen in addition to the AC component to induce dANM with each half period lasting equal time. The driving DC over a complete driving period is thus defined as $U_{dc} = (U_{dc1} + U_{dc2})/2$ with $|U_{dc2}| > |U_{dc1}|$. The results of the average migration velocities of mitochondria are shown in Figure 5-1. As seen from the results, the dANM signature is apparent for mitochondria. The velocity at each U_{dc} was proportional to the magnitude of U_{dc1} applied in one of the half periods. This is because in the other half period, mitochondria could be trapped by the DEP trapping force supplied by the AC component U_{ac_high} even though a driving DC voltage U_{dc2} was also applied. Besides, the sign of U_{dc1} was opposite to that of U_{dc2} and U_{dc}. Therefore, the smaller the absolute value of U_{dc1}, the smaller the velocities of mitochondria while the larger the value of U_{dc}. The error bars could be caused by the wide size distribution of mitochondria which ranged from 150 to 800 nm in radius (Appendix B 2).

In addition, the maximum dANM velocity amounts in ~5 µm/s which is comparable to that obtained for 4.4-µm beads in Chapter 4 at similar net driving DC while it is two orders of magnitude larger than previously reported for beads ANM [100]. This exhibits the great potential of dANM as a tool for the separation of mitochondrial sub-populations.

Proof-of-principle dANM-based separation experiment and numerical modeling with sub-micron polystyrene particles

To demonstrated that dANM could potentially be exploited in the separation applications in the sub-micron size range, two typical sizes which represent the lower and the upper limits of the normal mitochondria size range [4, 5], namely 0.3-µm and 0.9-µm diameters, were chosen for the experiment. According to the previous study [30] that mitochondria and polystyrene beads exhibit the same DEP trapping behaviors under both DC and low-frequency AC conditions, the beads were used as a model which can be easily prepared and could relate distinct behaviors observed in experiment to size directly. The microchannel used for mitochondria experiment was employed here with both sizes of beads suspended in pH 7.4 aqueous buffer solution.

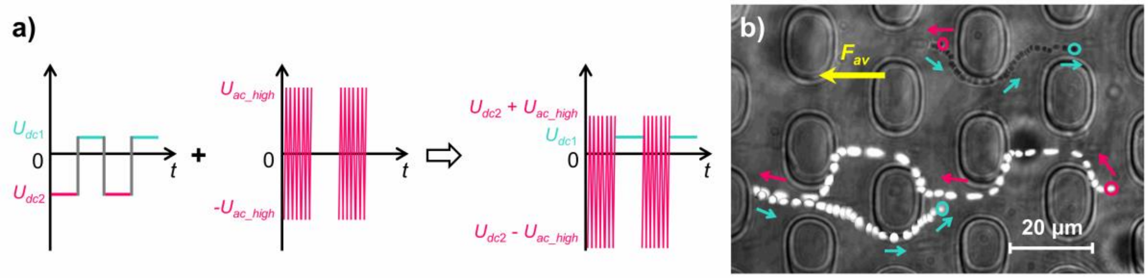

Figure 5-2. (a) The applied waveform for the manipulation of the sub-micron sized polystyrene beads of which the resultant trajectories were shown in (b). The driving DC voltages (here indicated through U_{dc1} and U_{dc2} on the left) are combined with an AC component U_{ac_high} to obtain the waveform shown on the right. To distinguish the two half driving periods, the potential applied in the first half period is displayed in pink and that applied in the second half period is turquoise. (b) The stroboscopic image shows the trajectory of a 0.9-µm bead (dark dot) and that of a 0.3-µm bead (fluorescent dot) in a complete driving period. In the first half period when $U_{dc2} + U_{ac\_high}$ was applied, both beads started at the position highlighted by the pink circles. Note that the 0.9-µm bead can only move back and forth within the region depicted by a pink arrow. Meanwhile, the 0.3-µm bead moved several spatial periods in the direction indicated by the pink arrows. During the application of U_{dc1}, both beads moved in the direction indicated by the turquoise arrows. By the end of the period, they ended up at the positions indicated by the turquoise circles. The distinctive migration behaviors in the entire driving period result in the dANM behavior of the 0.9-µm bead since its net migration was to the right while the 0.3-µm bead followed the average driving force $\boldsymbol{F}_{av}$ which pointed to the left.

A demonstration of the dANM-based separation of sub-micron polystyrene beads was shown in Figure 5-2. The AC signal U_{ac_high} was chosen with an amplitude of 400 V/cm and a frequency of 10 kHz. DC potentials of U_{dc2} = -60 V/cm and U_{dc1} = 20 V/cm were chosen so that particles that were not trapped can travel at least one spatial period in each half driving period. Figure 5-2(b) depicts the result from the experiment in which a trajectory of a 0.9-µm bead (dark dot) in a complete driving period in form of a stroboscopic image was show, clearly exhibiting the dANM signature. A trajectory of a 0.3-µm bead (fluorescent dot) obtained from the same video at the same conditions was also included to show the normal migration behavior, indicating that for smaller sizes the

DEP trapping force induced by U_{ac_high} was not strong enough as compared to the driving force by U_{dc2}. This example demonstrates the capability of dANM for the size-based separation of sub-micron species, which is promising for the sub-population analysis and separation of abnormally sized organelles in the nanometer size range.

In addition, the migration velocities were quantified from experiments for 0.9- and 0.3-µm-diameter beads (Figure 5-3, solid symbols). In this case, the AC signal U_{ac_high} was chosen with an amplitude of 800 V/cm and a frequency of 30 kHz. Potentials of U_{dc2} = -60 V/cm and U_{dc1} = 10, 20, 30, and 40 V/cm were chosen as the driving DC in each half period. At the applied conditions, 0.9-µm beads can be trapped at the posts upon the application of U_{dc2} and U_{ac_high} while they could migrate with the flow at U_{dc1}. Since $U_{dc} = (U_{dc1} + U_{dc2})/2$ and $|U_{dc2}| > |U_{dc1}|$, U_{dc} resulted in the same sign as U_{dc2} which was opposite to U_{dc1}. Therefore, the migration velocities of 0.9-µm beads were in a direction opposite to U_{dc}, exhibiting the dANM migration behavior. For the same reason, the velocity profile of 0.9-µm beads showed the same tendency as that observed for mitochondria as shown in Figure 5-1. To be specific, 0.9-µm beads accelerated while $|U_{dc}|$ was decreasing with the increasing $|U_{dc1}|$. Meanwhile, the DEP trapping force for 0.3-µm beads was weak that the beads migrated with the flow in both half periods. Thus, 0.3-µm beads showed the normal response and their average migration velocities were proportional to the magnitude of U_{dc}. Moreover, the resultant velocities as shown in Figure 5-3 have the similarly improved speed as that of mitochondria. More specifically, the maximum dANM velocity of 0.9-µm beads amounts in ~10 µm/s which were two orders of magnitude larger as compared to the previous ANM studies [100]. At the same conditions, 0.3-µm beads migrated with a similar magnitude of speed but in an opposite direction. Thus, the

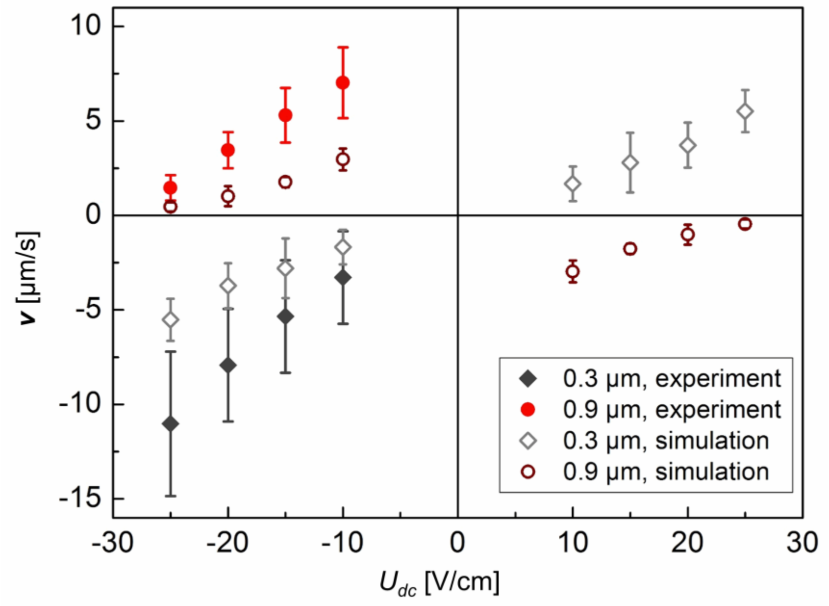

Figure 5-3. Experimental and simulation results of migration velocity ($\boldsymbol{v}$) vs. driving DC (U_{dc}) for the 0.3- and 0.9-micron-diameter particles. The error bars represent the standard deviations of the velocities obtained at each U_{dc} from tracking 60 or 20 individual trajectories for the experimental or the simulation results, respectively. The overlaid AC signal U_{ac_high} was 800 V/cm at 30 kHz. The driving DC in a complete driving period is defined as $U_{dc} = (U_{dc1} + U_{dc2})/2$ and $|U_{dc2}|>|U_{dc1}|$. At the applied conditions in both the experiment and the numerical modeling, the average migration velocities of 0.9-micron particles were in the opposite direction to the applied U_{dc}, exhibiting apparent dANM signature. Whereas 0.3-micron particles showed the normal response with their migration velocities proportional to $|U_{dc}|$. The simulation results were obtained at positive U_{dc} values but they were additionally mirrored to the side of the experimental results at negative U_{dc} in order to help guide the eyes. It is clear that the tendency of the velocities simulated by the numerical modeling was in good agreement with that quantified from the experiment.

two size groups can be directed into two opposite directions and the capability of dANM for solving the size-based separation problems in the sub-micron size range is demonstrated.

To help establish the new waveform (Figure 5-2(a)) and to understand the effect of the overlaid AC signal in inducing the DEP-based dANM migration, the same magnitude of the periodic driving potentials as applied in bead experiments were employed in numerical modeling for particles of 0.3 and 0.9 µm diameters with each half driving period lasted equal time. In this case, the AC signal U_{ac_high} still preserved an amplitude of 800 V/cm and a frequency of 30 kHz. Potentials of U_{dc2} = 60 V/cm and U_{dc1} = -10, -20, -30, and -40 V/cm were chosen as the driving DC in each half period since the physical principles contributing to dANM are not dependent on the sign of U_{dc}. The average velocities were evaluated for each particle size by tracking 20 individual particle trajectories at each U_{dc}. The results were shown in Figure 5-3 as hollow symbols.

According to the simulation results, the dANM signature was apparent for 0.9-µm-diameter particles. Thus, the simulated velocities had the same tendency as that for 0.9-µm beads quantified from experiments that the average migration velocities increased as $|U_{dc}|$ was decreased with the increasing $|U_{dc1}|$. As for the particles of 0.3 µm diameter, normal migration behavior was shown, which was the same as observed from experiments. By examining the particle trajectories (not shown), it is obvious that this smaller size migrated with the flow in both half driving periods, indicating that their velocities were proportional to the net DC potential applied in the entire driving period, *i.e.* U_{dc}. Therefore, the larger the value of U_{dc}, the larger the velocities of the 0.3-µm-diameter particles.

By comparing the velocity profiles obtained from the simulation (hollow symbols in Figure 5-3) to that from the experiment (solid symbols in Figure 5-3), the simulated values were lower than the experimental results for the same sized particles and at the same U_{dc}. This situation was also observed in Chapter 4 and it was suggested that it could be attributed to an overestimation of the dielectrophoretic trapping component as well as an underestimation of the electrophoretic component of the particles in the model. Since the EK mobility experimentally quantified for each particle size was employed in the simulation, the influence from the electrophoretic component has already been considered.

However, the DEP mobilities used in simulations were calculated by Eq. $(2-21)$ with the assumption that f_{CM} = -0.5. Whereas in reality, f_{CM} may deviate from -0.5 and ranges from -0.5 to 0, which could consequently result in smaller DEP mobility values and thus higher velocities. In addition, it should be noted that numerical modeling did not reflect all the experimental effects. Therefore, in spite of the slower velocities as obtained by numerical modeling, the simulation results still reached 2 orders of magnitude faster speed than pervious ANM approaches [100] and thus were in good agreement with the experiment.

The resolution of dANM-based separation

The resolution R_S of a separation can be readily used to reflect how well two specific components are separated. It can be defined by the distance ΔX between the two zones divided by the combined widths of their peaks (Figure 5-4) [102]:

$$R_S = \frac{\Delta X}{2(\sigma_{S1}+\sigma_{S2})} \qquad (5-1)$$

where σ_S is the standard deviation which related to the total effective diffusion coefficient D_T and the time t [102]:

$$\sigma_S = (2D_T t)^{1/2} \qquad (5-2)$$

D_T describes all the factors that contribute to the random walk of a particle and thus lead to the zone broadening.

Since 95.6% of a Gaussian area lies between $-2\sigma_S$ and $2\sigma_S$, the distance from $-2\sigma_S$ to $2\sigma_S$ can be arbitrarily taken as the effective zone width w (Figure 5-4). The resolution can thus be determined by [102]:

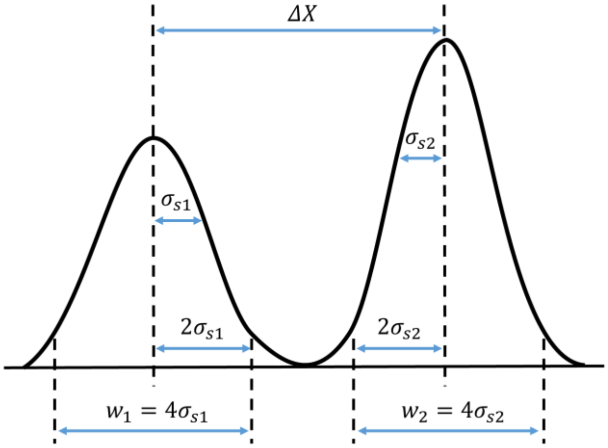

Figure 5-4. Separation resolution for two specified component zones is defined as $R_s = \Delta X/2(\sigma_{s1} + \sigma_{s2})$, where ΔX measures the distance between the peaks and $2\sigma_{s1}$ and $2\sigma_{s2}$ represent the zone dispersion. The distance from $-2\sigma_s$ to $2\sigma_s$ can be termed as the effective zone width w.

$$R_s = \frac{2\Delta X}{w_1 + w_2} \tag{5-3}$$

Since the numerical modeling can provide the coordinates of the released particles at specified time steps, the resolution of dANM-based separation at specific conditions applied in an experiment can be estimated by Eq. $(5-3)$ with the data provided by the simulation results. For example, based on the simulation results for 0.9- and 0.3-μm-diameter particles at U_{dc} = 10 V/cm (Figure 5-3), the resolution is determined to be R_s = 1.5 (Appendix B 5), which indicates a good baseline separation. Note that this result is based on just one complete driving period lasting for 20 seconds in the simulation. Given that more than one driving periods can be run in an actual experiment, the two particle sizes from the same injection inlet could be separated and be collected at the corresponding outlets without any overlap. With the above descriptions of R_s and the numerical modeling, the parameters needed to obtain an optimized resolution for a dANM separation can be found for other combinations of particle sizes, DEP and electrokinetic properties while avoiding to conduct time-consuming experiments.

CONCLUSION

In this work, the C57BL/6 mouse hepatic mitochondria were manipulated in a non-linear symmetric microfluidic post array. A low-frequency AC signal was additionally overlaid with periodic driving DC potentials to supply periodic EK driving and strong enough DEP trapping force for the mitochondrial sample. With these conditions, dANM migration was induced for mitochondria and the average migration velocities were quantified. Further, the dANM-based separation was demonstrated experimentally with 0.3- and 0.9-μm-diameter polystyrene beads. To be specific, dANM behavior was induced for 0.9-μm beads whereas the 0.3-μm beads were observed to show normal migration at the same conditions. This is the first experimental realization of directing differently sized sub-micron particles into opposite directions by dANM, indicating that this novel migration technique can be applied as a tool for the size-based separations in the sub-micron size range. In addition, the experimentally determined EK mobilities for 0.3- and 0.9-μm-diameter beads were employed in the numerical modeling and the migration velocities were quantified for each particle size. The simulated velocity profiles showed good agreement with the experimental results for beads in terms of the magnitude and tendency. Moreover, both the aforementioned mitochondrial velocity profile and the bead velocities have suggested an intrinsic advantage of dANM which lies in the two orders of magnitude improved average migration velocities as compared to the existing ANM approaches for similarly sized particles [100] and up to four times larger magnitude to ratchet approaches [51]. Furthermore, an example calculation for the separation resolution was shown based on a set of simulation data. The result demonstrated baseline separation for 0.3- and 0.9-µm-diameter particles within 20 seconds. Therefore, dANM is favorable for future separation or fractionation applications of mitochondria sub-populations. In addition, the here presented dANM approach can be readily realized with standard photolithographic and soft lithographic techniques and allows inducing dANM for sub-µm species via the adjustment of the DEP trapping forces though the variation of the externally applied potentials. It is thus envisioned that this novel migration mechanism is applicable to a wide range of separation problems in which size selectivity is required, such as in the fractionation of organelles and their subpopulations, in nanotechnological applications or as fractionation method for protein nanocrystals.

CHAPTER 6

DIELECTROPHORESIS OF *SALMONELLA TYPHIMURIUM*

INTRODUCTION

Salmonella typhimurium (*Salmonella* for short in the following content) is an infectious food borne pathogen which could result in severe symptoms such as gastroenteritis [103, 104]. Literature has suggested that a two-component system PhoP/PhoQ in *Salmonella* is responsible for regulating the lipid components and proteins in the bacterial envelope which are important for the survival and virulence of the bacteria within the host tissue [105]. This regulation by the PhoPQ system to the surface component of *Salmonella* can be stimulated by environmental conditions and directly results in the alteration of the bacterial surface charge density. Since the change of the lipid and protein contents cannot be probed directly, the variance of the bacterial surface charge can be exploited instead to gain insight into the bacterial envelope composition and to elucidate the PhoPQ regulatory work on the bacterial resistance to antibiotics.

Dielectrophoresis (DEP) depends on the migration of polarizable species in an inhomogeneous electric field. Since different populations of *Salmonella* possess similar size, the surface charge of this bacterium is a major factor that influences the bacterial polarization in an electric field [46]. Therefore, DEP can be applied as a tool for the study of *Salmonella* surface charge. Previously, the DEP-dependent techniques have been utilized to manipulate various bacterial species, such as the dielectrophoretic concentration and separation of the live and the dead *E. coli*. [71] The selectivity of insulator-based DEP (iDEP) was also employed for the separation and concentration of Gram-negative and

Gram-positive bacteria [72]. In addition, a study has suggested using electrode-based DEP (eDEP) to detect *Salmonella* within microfluidic channels [106]. However, iDEP-based techniques for distinguishing *Salmonella* sub-populations have not been assessed experimentally yet.

In this work, an insulator-based microfluidic device was utilized to study the DEP properties of *Salmonella* sub-populations at low-frequency AC conditions. Different levels of Mg^{2+} were applied to stimulate the charge variance in the cell envelope of *Salmonella* wild-type (WT). More specifically, the *Salmonella* wild-type exhibits low or high negative charges when incubated in low (-L) or high (-H) Mg^{2+} concentration, respectively. A *Salmonella* mutant-type (mutant) was additionally studied in the experiment as a control since this mutant strain always carries high surface charges regardless of the environmental stimulations. It is envisioned that the dielectrophoretic study of *Salmonella* variants presented here will provide novel insight in the fractionation and detection techniques for *Salmonella* sub-populations and extend the studies to the regulatory network of PhoPQ upon Mg^{2+} stimulation and the antibiotic resistance of the bacteria.

MATERIALS AND METHODS

Chemicals

SYLGARD® 184 silicone elastomer kit for polydimethylsiloxane (PDMS) was obtained from Dow Corning Corporation (Midland, MI, USA). 4-(2-hydroxyethyl)piperazine-1-ethanesulfonic acid (HEPES), poly(ethylene glycol)-*block*-poly(propylene glycol)-*block*-poly(ethylene glycol) (brand name Pluronic® F108), potassium hydroxide, and sucrose were purchased from Sigma-Aldrich (St. Louis, MO, USA). Deionized (DI) water was from a Synergy purification system (Millipore, USA). Gold-Seal coverslip were purchased from Electron Microscopy Sciences (48 × 60 × 0.15 mm; Hatfield, PA, USA). Platinum wire was purchased from Alfa Aesar (Ward Hill, MA, USA).

Microchip fabrication

The pattern of the microstructure was shown in Figure 6-1(b). The fabrication of the photopatterned master wafer and the preparation of the microfluidic device for the study of the iDEP properties of *Salmonella* were the same as described in Chapter 3. . The preparation of the microfluidic chip used in the experiment in which channel position dependent iDEP of *Salmonella* was observed was the same as described in Chapter 5.

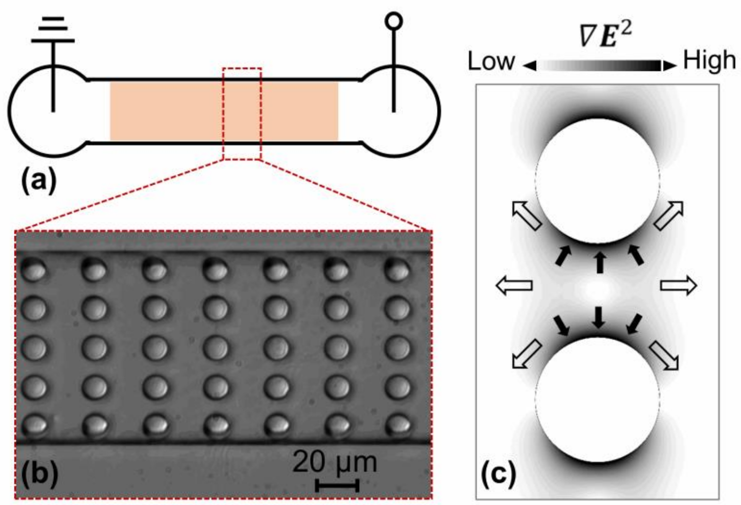

Figure 6-1. (a) Schematic of the 1-cm-long microfluidic channel (not to scale). The shaded area corresponds to the post array region. (b) Bright field microscopy image (top view) of a section of the post array region. (c) Upon the application of a potential in the channel reservoirs, electric field gradients are established around the posts and the $\nabla \boldsymbol{E}^2$ distribution is indicated by the color code. The solid arrows indicate the attraction in pDEP mode and the open arrows indicate the repulsion from the high $\nabla \boldsymbol{E}^2$ regions, *i.e.* nDEP.

Fluidic operations

The experiments were performed using the microfluidic device as schematically shown in Figure 6-1(a). After assembly, all microfluidic channels were filled with solution A (1 mM F108, 10 mM HEPES, pH adjusted to 7.4 by KOH, sterile-filtered to 0.2 µm) by capillarity and the chip was placed in a humid environment overnight (16 – 24 hours) to ensure complete surface coating with F108.

After that, the channel was rinsed for three times with solution B (250 mM sucrose in solution A, pH 7.4, 0.03 S/m, sterile-filtered to 0.2 µm) for the DEP property studies or with solution A for the experiment in which channel position dependent iDEP of *Salmonella* was observed. A 0.5-cm-thick PDMS holder was employed to increase the reservoir volume and to provide stability for the electrodes. The prepared bacteria solution was added to both reservoirs with mineral oil added on top of the liquid layer to prevent evaporation. Pt electrodes attached to the reservoirs were connected via micro-clamps (LabSmith, Livermore, CA, USA) to an AC power supply from a high voltage amplifier (AMT-3B20, Matsusada Precision Inc.) driven through a Multifunction DAQ card (USB X Series, National Instruments, TX, USA) programmed by LabVIEW 2014 (version 14.0, National Instruments).

Preparation of *Salmonella typhimurium* samples

Two strains of *Salmonella*, *i.e.* the wild type (WT) and the mutant type (mutant), were grown and prepared in either low [Mg^{2+}] (-L) or high [Mg^{2+}] (-H) buffer by Dr. Yixin Shi from School of Life Sciences, ASU. The samples were modified to express the green fluorescent protein (GFP) [107] so that their migration behavior can be observed and imaged through fluorescence microscopy. Each sample was freshly prepared and then incubated in 37 ^{o}C with gentle shaking at 160 rpm for 2 hours right before the DEP experiment. In addition, the sample type was not revealed until the DEP experiment was completed (*i.e.* blind test).

For the iDEP property studies, a sample was centrifuged at 10000 rpm (5-cm radius) for 2 min and the supernatant was removed. Then, 200 μL solution B was added to the pellet followed by gentle vortexing and re-suspension of the sample. Next, the sample was centrifuged again and the supernatant was removed. Finally, the pellet was re-suspended in 100 μL solution B.

For the experiment in which channel position dependent iDEP of *Salmonella* was observed, each sample was prepared in the same way as described above except that solution A was used instead of solution B, and that the pellet was re-suspended in 50 μL solution A in the final re-suspension.

Detection and data analysis

Fluorescence images were acquired with an inverted microscope (IX71, Olympus, Center Valley, PA, USA) equipped with a 100 W mercury burner (U-RFL-T, Olympus, Center Valley, PA, USA) and fluorescence filter set (exciter ET470/40, dichroic T495LP, emitter ET525/50, Semrock, USA). A 60 × (UPLSAPO60 ×W, water immersion, NA = 1.20) objective was used to visualize bacteria migrations in the microchannel. Images were captured by a CCD camera (QuantEM:512SC, Photometrics, Tucson, AZ, USA) and Micro-Manager software (version 1.4.7, Vale Lab, UCSF, CA, USA). The obtained images were then processed by ImageJ software (version 1.49, NIH).

RESULTS

iDEP properties of *Salmonella typhimurium*

The DEP behavior of *Salmonella* was investigated in the device schematically shown in Figure 6-1(a). The 1-cm-long insulator-based microchannel exhibited an integrated array of circular posts (Figure 6-1(b)). Surface coating with Pluronic® F108 was utilized to significantly reduce the adsorption of samples to the channel walls as well as sample aggregation [42, 81, 82]. A reservoir holder was attached to the PDMS mold and defined the volume of the reservoirs accessing the inlet and outlet. A low conductivity buffer with physiological pH and sucrose was chosen to maintain the cell osmostic pressure. The experiments were conducted at 10 kHz with applied voltages varying from zero to up to hundreds of volts until significant trapping behaviors were observed.

Figure 6-1(c) shows the arising $\nabla \boldsymbol{E}^2$ schematically located at the post sides perpendicular to the direction of the potential drop along the channel. Additionally, solid arrows indicate the direction of pDEP while the nDEP mode is represented by the open arrows at the applied AC conditions.

Upon the application of an AC signal, the DEP trapping behavior of *Salmonella* was pronounced since the electrokinetic component was suppressed. Interestingly, the populations of *Salmonella* stimulated by different levels of [Mg^{2+}], *i.e.* the wild-types and the mutant-types incubated in either low or high [Mg^{2+}], were all observed to be attracted to the post sides with high $\nabla \boldsymbol{E}^2$ (Figure 6-1(c)), indicating pDEP behavior. An example of the trapping behavior of *Salmonella* was shown in Figure 6-2 with a series of fluorescence snapshots of the mutant-type *Salmonella* which were incubated in high [Mg^{2+}] (mutant-H). As the applied AC amplitude increased from 50 to 80 V/cm at 10 kHz, the trapping

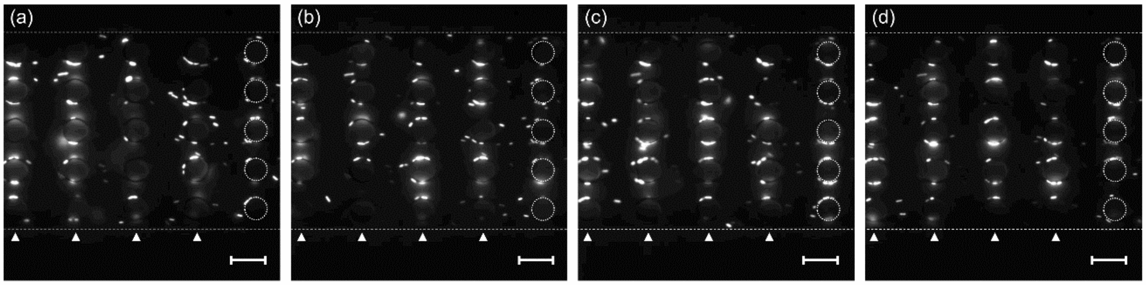

Figure 6-2. iDEP trapping demonstrated by the mutant-type *Salmonella* incubated in high [Mg^{2+}]. The experiments were conducted with a frequency of 10 kHz and an AC amplitude of (a) 50, (b) 60, (c) 70, and (d) 80 V/cm. Scale bar is 20 µm. In each figure, one row of posts and the channel edges are outlined with the other rows of posts indicated by triangles. In all the figures, *Salmonella* either migrated around the insulating posts freely or were trapped at the regions with high electric field gradient at the posts, exhibiting pDEP behavior. Moreover, as the AC amplitude increased from (a) to (d), the trapping response of the bacteria became firmer and accelerated upon the application of the voltage. In addition, less bacteria were observed undergoing free migration. A trapping potential threshold of 80 V/cm for the mutant- H *Salmonella* was determined.

response of the bacteria became firmer such that less freely migrating bacteria could be observed. This effect was also observed upon the application of a higher voltage. The trapping potential threshold was defined as the applied overall electric field, when the applied voltage is increased to a certain magnitude at which no further change in the trapping behavior of a sample can be observed,. Thus, the trapping potential threshold of the mutant-H *Salmonella* was found to be 80 V/cm (as demonstrated in Figure 6-2(d)).

The trapping potential thresholds of the other three types of *Salmonella* were also tested and the results were summarized in Table 6-1. A difference was found in the trapping potential thresholds of the wild-type *Salmonella* incubated in different levels of [Mg^{2+}]. Compared to those incubated in high [Mg^{2+}] (WT-H), the WT-L *Salmonella* required a higher applied voltage to show a significant trapping behavior. In addition, the wild-type *Salmonella* incubated in high [Mg^{2+}] exhibited the same trapping potential threshold as the mutant types which always carry high surface charges regardless of the environmental conditions. This may indicate that the wild-type *Salmonella* incubated in high [Mg^{2+}] exhibited high surface charge in the cell envelope. The results demonstrate the potential application of iDEP in distinguishing *Salmonella* differing in surface charges while possessing the same or similar sizes.

Table 6-1. Observed trapping potential thresholds for the four *Salmonella* types tested

Salmonella type	Trapping potential threshold @10 kHz
mutant-L	80 V/cm
mutant-H	80 V/cm
WT-H	80 V/cm
WT-L	110 V/cm

Channel position dependent iDEP of *Salmonella*

In a repeating experiment of determining the DEP trapping potential thresholds for *Salmonella,* an all-PDMS microfluidic device and the buffer solution A without sucrose were utilized to explore ways of optimizing the experiment procedures. Interestingly, nDEP trapping behavior was observed for *Salmonella* in addition to the pDEP trapping behavior described above. Once this phenomenon was noticed, the migration of the sample in the entire microchannel was investigated with an AC amplitude of 500 V/cm at 30 kHz. Note that two electrodes were placed in the inlet and outlet reservoirs to supply the voltage over the 1-cm-long microchannel. As schematically show in the center of Figure 6-3, the

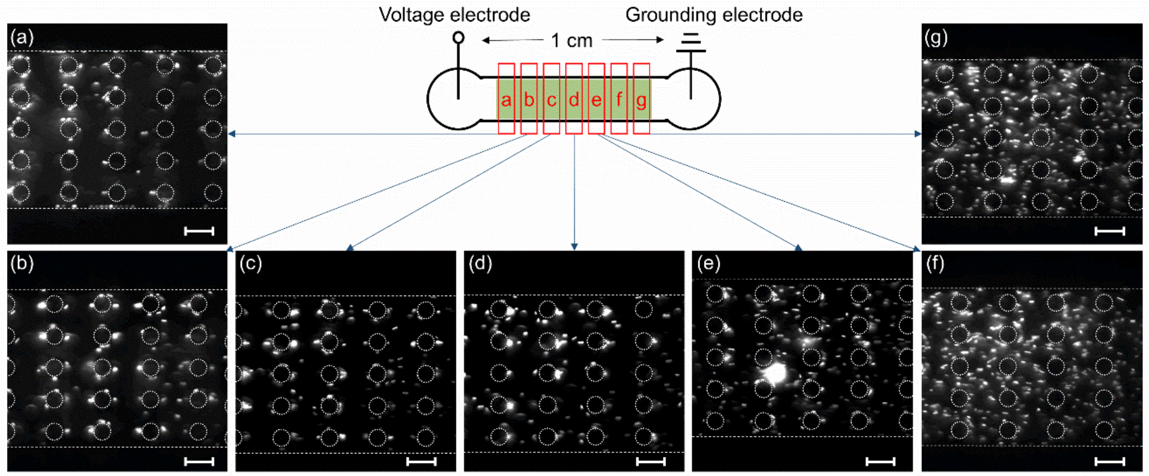

Figure 6-3. Channel position dependent iDEP of *Salmonella*. As demonstrated by the schematics of the 1-cm-long microchannel in the center of the figure, an electrode supplying 500 V/cm at 30 kHz was placed in the left reservoir and a grounding electrode was placed in the right reservoir. Scale bar is 20 μm. The posts and the channel edges are outlined for each figure. With the observation region moving from left to right along the channel, the observed migrations of *Salmonella* were as follows: (a) Firm pDEP trapping of *Salmonella* occurred while it was also observed that some bacteria can migrate along the edges of the channel and loosely attach to the post sides with low $\nabla \boldsymbol{E}^2$. (b) & (c) nDEP trapping of *Salmonella* occurred and it became obvious as the focus plane continued moving to the right along the channel. (d) & (e) Both pDEP and nDEP behaviors of *Salmonella* became less evident. (f) & (g) *Salmonella* tended to migrate freely in the channel rather than being trapped by pDEP or nDEP.

electrode in the left reservoir supplied a positive voltage while the one in the right reservoir was just grounded. Thus they are named as the voltage electrode and the grounding electrode respectively in the following contents. As demonstrated by the fluorescence snapshots in Figure 6-3, starting from the left side of the channel and at a position near the voltage electrode, the pDEP trapping behavior of *Salmonella* occurred and the bacteria were trapped to the post sides with high $\nabla \boldsymbol{E}^2$ firmly. However, it was noticed that in the same region some bacteria could loosely attach to the post sides with low $\nabla \boldsymbol{E}^2$. When the observation region was moved along the channel to the right, bacteria exhibiting nDEP trapping behavior were observed in addition to those trapped by pDEP. Moreover, the nDEP trapping became dominant as the observation region was further moved to the right. When it eventually got closer to the grounding electrode, both pDEP and nDEP behaviors became less evident and the bacteria tended to migrate freely in the channel.

To verify these observations, the voltage and the grounding electrode were switched in the reservoirs and the migration of *Salmonella* was checked again from left to right along the channel. Surprisingly, the trapping behavior of *Salmonella* observed this time were exactly the same as what was described above but the occurrence was in reversed order.

One possible factor that lead to the newly observed DEP behavior of *Salmonella*, *i.e.* the nDEP trapping, was the conditions used in this experiment. Different from the aforementioned iDEP property studies, the sample can only get in contact with the PDMS surface and there was no sucrose in the solution in this case. Yet, it is difficult to tell whether a glass substrate affects the migration behaviors of *Salmonella* or not. As for sucrose, since it is widely used to maintain the osmosis of bio-species, the absence of sucrose may cause physiological alteration of the sample cell which could potentially affect the polarizability. But this needs further experiment before any conclusion is drew.

Furthermore, a possible reason for the simultaneous occurrence of pDEP and nDEP behaviors observed for the same sample at the same conditions could be that the *Salmonella* sample was not homogeneous. Though each sample was prepared freshly, the bacteria populations could be in different growth states which preserved variations in size as well as in surface charge. In addition, the samples prepared that day may have a compromised quality leading to deviations in the response to the application of the electric field. However, it is noteworthy that switching two electrodes lead to the reversed order of the observed trapping behaviors of *Salmonella* along the entire channel, which cannot simply be explained by the sample variation. It is thus proposed that the unusual phenomena was also attributed to the positions of the electrodes.

A possibility that can relate the forenamed phenomena to the positions of the electrodes is the water electrolysis reactions which could potentially happen in an aqueous buffer at the voltage electrodes upon the application of a voltage, generating H^+ at the anode and OH^- at the cathode. A previous study suggested that the H^+ and OH^- transport "is responsible for pH drops from the anode toward the cathode" and results in the formation of a pH gradient across the microfluidic channel [91]. Because the buffering capacity of the solution was limited by the low concentration of the buffering agent used in this experiment which was only 10 mM HEPES, electrolysis could happen at the voltage electrode and cause a pH change in the channel. In addition, the study reported that a significant pH change could be detected within 6 – 9 minutes for a medium with a conductivity of 0.01 or 0.05 S/m at a DC voltage of 100 V/cm [91]. Since the DEP study of *Salmonella* was conducted in a medium of 0.03 S/m and an AC amplitude of 500 V/cm at 30 kHz was employed, it is likely that a pH drop has initiated or already established during an observation along the channel. Moreover, the polarization of a particle involves not just the properties of the particle itself (particle size, effective surface area, and surface charge, *etc.*) but also the macroscopic movement of ions around the particle [46]. Therefore, the migration of *Salmonella* upon the application of the electric field in the post array could vary in accordance with the different concentrations of H^+ and OH^- along the channel, leading to the aforementioned phenomena that *Salmonella* near the voltage electrode can show obvious trapping behaviors (either pDEP or nDEP) while those far away from the voltage electrode more tended to migrate freely. Furthermore, if the voltage electrode and the grounding electrode switched positions, a new pH gradient would be established conversely to the previous pH drop, thus resulting in a reversed order of observation along the channel as mentioned above.

To verify if the migration behavior of *Salmonella* in a non-uniform electric field relate to the pH, experiments can be designed to determine the response of *Salmonella* in buffers of various pH. Meanwhile, strategies of maintaining the pH in the microchannel could be considered. A straightforward way is to use a buffer with high concentration that provides high buffering capacity to mediate the pH drop in the channel [91]. However, a solution of high concentration usually possesses a high conductivity, which could lead to the formation of bubbles in the channel when a high voltage is applied. Therefore, a device that can remove bubbles may also be essential, such as suggested by Xu *et al.* [108] and Zheng *et al.*[109] Yet, assembling and operating such bubble-removal device would increase the complexity of an experiment, which should be considered before use. Another method for maintaining the pH in the channel is to use contactless DEP (cDEP) which avoids the direct contact of the sample solution with the electrodes. Thus, using this technique removes all electrode reactions from the main channel (sample channel) such as water electrolysis. In addition, it is easy to fabricate the cDEP-based device because no miniature feature is needed in the structure [74-77]. However, the limitation of cDEP is still noteworthy. As described in the introduction in Chapter 3, the frequency and voltage applied in the side channel should be strong enough to induce a suitable electric field gradient for the manipulation of particles in the main channel, while it should not exceed the dielectric breakdown voltage of the barriers (such as 280 V for a 20-µm PDMS membrane).

CONCLUSION

In this chapter, an insulator-based microfluidic device was employed to study the DEP properties of four types of *Salmonella typhimurium*, *i.e.* wild type and mutant type incubated in low or high [Mg^{2+}]. Each *Salmonella* sample was prepared freshly and was suspended in a medium with a conductivity of 0.030 S/m at physiological pH. Upon the application of voltages with a frequency of 10 kHz across the 1-cm-long F108-coated microchannel, it was elucidated that *Salmonella* exhibit pDEP behavior. Further, the *Salmonella* sub-populations which differ in the density of the surface charges were found to have different trapping potential thresholds. In general, *Salmonella* with high surface charges, *i.e.* the mutant type incubated in both concentrations of Mg^{2+} and the wild type incubated in high [Mg^{2+}], begin to show significant pDEP trapping behavior at 80 V/cm. Meanwhile, the wild-type *Salmonella* incubated in low [Mg^{2+}] carry low surface charges in the cell envelope and their trapping behavior became evident when the voltage reached 110 V/cm. This difference in the trapping potential thresholds reveals the potential of exploiting iDEP for identifying sub-populations of *Salmonella* with different density of surface charges while possessing similar sizes.

Furthermore, an unusual phenomenon was observed in a repeated DEP experiment for *Salmonella* in which both pDEP and nDEP trapping behavior was observed for the bacteria of the same type. The application of the all-PDMS channel and the absence of sucrose in this experiment may contribute to the newly observed nDEP behavior of

Salmonella. Besides, the sample was not homogeneous or it was of compromised quality may be the possible reasons. In addition, it is likely that water electrolysis happened at the voltage electrode which lead to the formation of a pH gradient in the channel. Since the polarizability of a particle can be affected by the surrounding ions, the different concentrations of H^+ and OH^- along the channel may have contributed to the channel position dependent trapping behaviors of *Salmonella*. Suggestions were provided for maintaining the pH in the channel. But further experiments are needed in order to verify the dependence of the DEP trapping behavior of *Salmonella* on the aforementioned experimental conditions and the pH of the medium. Overall, this work has provided preliminary studies for *Salmonella* at low-frequency AC conditions, contributing to the future development of distinguishing *Salmonella* sub-populations by iDEP.

CHAPTER 7

SUMMARY AND CONCLUSIONS

In summary, the DEP properties of mitochondria isolated from Fischer 344 (F344) rat semimembranosus muscle and C57BL/6 mouse liver were firstly studied in an insulator-based microfluidic device. It was elucidated that the organelle exhibits nDEP behavior in both DC and AC (0 – 50 kHz) electric fields with potentials of 0 – 3000 V applied across a 1-cm-long channel. The tailored iDEP device was statically coated with F108 to prevent adhesion of bio-samples to the channel surface. A dynamic F108 coating and a buffer with a conductivity of 0.025 – 0.030 S/m at physiological pH were used in the experiments. With these experimental conditions, the trapping potential thresholds for the isolated mitochondria at the applied frequency range were found to be generally above 200 V/cm and were weakly dependent on frequency. In addition, the polystyrene beads with a size similar to the normal mitochondria were employed as a model for the DEP study. They exhibited nDEP behavior at the post array which was in good agreement with that of the mitochondria under the same conditions. This study thus provides important information about the isolated mitochondria under both DC and AC conditions,

Further, successful DEP-based sorting of the isolated mitochondria into various size fractions was conducted at low DC potentials. Dynamic light scattering was used to analyze the size distribution of the mitochondria sample collected from each outlet after the sorting experiment. The size range investigated turned out to be highly compatible with separations of “giant” mitochondria observed under conditions of disease and aging [4]. This is the first time that iDEP sorting of an organelle type, specifically mitochondria, has been demonstrated. Additionally, the amount of the sorted mitochondria is suitable for most microbiological studies and any potential negative effects due to the iDEP manipulation are greatly suppressed due to the low potentials applied in the sorting device. Specifically, this study contributes to a foundation for the future development of separation and applications for mitochondria sub-populations to investigate their role in aging and diseases.

Moreover, based on the aforementioned DEP property studies of the isolated mitochondria and polystyrene beads, a non-linear symmetric insulator-based microfluidic post array was successfully developed to evoke dANM. This structure avoided the integration of geometrical traps which were utilized by previous ANM studies [35-38], thus removing the required microstructured features similar in size to the micron- or nano-particles of interest. The first design study for the deterministic counter-intuitive migration mechanism was demonstrated through numerical modeling. Further, by employing µm- and sub-µm sized polystyrene beads, the occurrence of dANM was realized with the integration of periodically driven electrokinetic and dielectrophoretic forces and it was proved to be in excellent agreement with the numerical model. Suitable parameter selection of the driving forces was demonstrated through both numerical modeling and experiment, proving that the size selectivity of this novel migration technique is ideally suited for separation and fractionation, and that it allows steering analytes into opposite directions and at different rates. It is noteworthy that the only tuning parameter is the dielectrophoretic component for given electrokinetic and intrinsic sample contributions, which can be promptly adjusted through the externally applied potentials according to the experimental observations. As quantified from the dANM experiments with polystyrene beads, an intrinsic advantage of dANM lies in the two orders of magnitude improved average migration velocities as compared to the existing ANM approaches [100] and up to four times larger magnitude to ratchet approaches [51], which is favorable for future separation or fractionation applications. In addition, the device for the here presented dANM approach can be fabricated with standard photolithographic and soft lithographic techniques while the technically challenging miniaturization of the geometric traps needed for the previous ANM studies [100] is not required.

Furthermore, by integrating a low-frequency AC signal in one of the half driving periods, the DEP trapping for the sub-μm species can be achieved with the adjustment of the amplitude and frequency of the AC component. Thus, the DC potentials in each half period only need to be adjusted in accordance with the need of sample driving while dANM can be induced for species in the sub-micron size range with this novel waveform. As proof-of-principle, the realization of dANM for the isolated mouse liver mitochondria was shown and it represented the first experimental application of an ANM migration mechanism for a bio-species. Based on that, the migration velocity profile of the isolated C57BL/6 mouse hepatic mitochondria was quantified within the F108-coated all-PDMS microfluidic device with the employment of the aforementioned waveform. This waveform was further employed in the separation experiment with sub-micron sized polystyrene beads. The dANM migration was realized for the 0.9-μm-diameter beads whereas the beads of 0.3 μm diameter showed the normal response. This is the first experimental realization of directing differently sized sub-micron particles into opposite directions by dANM. Thus, the size selectivity of this novel migration technique has successfully extended into the sub-micron size range. Next, together with the experimentally quantified EK mobilities for beads, the waveform was applied in numerical modeling. The simulated velocity profiles were in good agreement with the experimental results and demonstrated a good baseline resolution of dANM-based separation. In addition, the average migration velocities of the beads and the aforementioned mitochondrial velocity profile were two orders of magnitude improved as compared to the existing ANM approaches [100] and four times larger magnitude to ratchet approaches [51]. The results have demonstrated the capacity of this novel migration mechanism in the applications of a wide range of separation problems in which size selectivity is required, such as in the fractionation of organelles and their subpopulations, in nanotechnological applications or as fractionation method for protein nanocrystals.

In addition to the DEP and dANM studies of mitochondria, iDEP was also employed in distinguishing *Salmonella typhimurium* strains grown with different concentrations of Mg^{2+}. The iDEP property studies elucidated that *Salmonella* exhibit pDEP behavior when suspended in a medium with a conductivity of 0.030 S/m at physiological pH. Further, a difference in the trapping potential thresholds for the *Salmonella* samples with different densities of surface charge was observed upon the application of voltages with a frequency of 10 kHz. In general, the mutant types grown in both concentrations of Mg^{2+} and the wild type incubated in high [Mg^{2+}], *i.e.* those with high charge density in the cell envelope, can show significant trapping behaviors starting at 80 V/cm. Meanwhile, the wild-type *Salmonella* incubated in low [Mg^{2+}] carries low surface charges. Thus a higher voltage of 110 V/cm was needed to observe the evident trapping behavior of this type.. Moreover, unusual phenomena were observed for *Salmonella* of the same type that both pDEP and nDEP trapping behaviors can be seen at the same conditions and that different migrations occurred along the channel which related to the position of the voltage electrode. The newly observed nDEP behavior of *Salmonella* may be related to the removal of the glass substrate and the absence of sucrose in the experiment. In addition, possible reasons for the simultaneous occurrence of the pDEP and nDEP trapping behaviors include that the bacterial populations may be at different growth stages and that the sample may have a compromised quality. Furthermore, it is likely that the formation of a pH gradient happened due to water electrolysis at the voltage electrode. Since the polarization of a particle can also be affected by the surrounding ions [46], the channel position dependent iDEP behaviors of *Salmonella* may be caused by the different concentrations of H^+ and OH^- along the channel but will need experiments to verify. Suggestions on maintaining the pH in the microchannel were additionally provided. Overall, this study provided the preliminary experimental results for the DEP properties of *Salmonella* at AC conditions, contributing a foundation to the future development in distinguishing the sub-populations of *Salmonella* by iDEP.

REFERENCES

1. Abou-Sleiman, P. M.; Muqit, M. M. K.; Wood, N. W. Expanding Insights of Mitochondrial Dysfunction in Parkinson's Disease. *Nat. Rev. Neurosci.* **2006**, *7*, 207-219.

2. McBride, H. M.; Neuspiel, M.; Wasiak, S. Mitochondria: More Than Just a Powerhouse. *Curr. Biol.* **2006**, *16*, R551-R560.

3. Newmeyer, D. D.; Ferguson-Miller, S. Mitochondria: Releasing Power for Life and Unleashing the Machineries of Death. *Cell* **2003**, *112*, 481-490.

4. Navratil, M.; Terman, A.; Arriaga, E. A. Giant Mitochondria Do Not Fuse and Exchange Their Contents with Normal Mitochondria. *Exp. Cell Res.* **2008**, *314*, 164-172.

5. Brown, T. A.; Fetter, R. D.; Tkachuk, A. N.; Clayton, D. A. Approaches toward Super-Resolution Fluorescence Imaging of Mitochondrial Proteins Using PALM. *Methods* **2010**, *51*, 458-463.

6. Heffner, R. R.; Barron, S. A. Early Effects of Ischemia upon Skeletal-Muscle Mitochondria. *J. Neurol. Sci.* **1978**, *38*, 295-315.

7. Brenner, O.; deLahunta, A.; Cummings, J. F.; Summers, B. A.; Monachelli, M. A Canine Encephalomyelopathy with Morphological Abnormalities in Mitochondria. *Acta Neuropathol.* **1997**, *94*, 390-397.

8. Squitieri, F.; Falleni, A.; Cannella, M.; Orobello, S.; Fulceri, F.; Lenzi, P.; Fornai, F. Abnormal Morphology of Peripheral Cell Tissues from Patients with Huntington Disease. *J. Neural Transm.* **2010**, *117*, 77-83.

9. Haust, M. D.; Dewar, R. A.; Gatfield, D. P.; Gordon, B. A. Hyperornithinemia-Hyperammonemia-Homocitrullinuria (HHH)-Syndrome - Ultrastructural Changes of Mitochondria in Cultured Dermal Fibroblasts of Three Patients. *Pathol. , Res. Pract.* **1996**, *192*, 271-280.

10. Abramovich, C. M.; Prayson, R. A.; McMahon, J. T.; Cohen, B. H. Ultrastructural Examination of the Axillary Skin Biopsy in the Diagnosis of Metabolic Diseases. *Hum. Pathol.* **2001**, *32*, 649-655.

11. de Pablo-Latorre, R.; Saide, A.; Polishhuck, E. V.; Nusco, E.; Fraldi, A.; Ballabio, A. Impaired Parkin-Mediated Mitochondrial Targeting to Autophagosomes Differentially Contributes to Tissue Pathology in Lysosomal Storage Diseases. *Hum. Mol. Genet.* **2012**, *21*, 1770-1781.

12. Eppenberger-Eberhardt, M.; Riesinger, I.; Messerli, M.; Schwarb, P.; Mueller, M.; Eppenberger, H. M.; Wallimann, T. Adult-Rat Cardiomyocytes Cultured in Creatine-Deficient Medium Display Large Mitochondria with Paracrystalline Inclusions, Enriched for Creatine-Kinase. *J. Cell Biol.* **1991**, *113*, 289-302.

13. Eppenberger, H. M.; Hertig, C.; Eppenberger-Eberhardt, M. Adult-Rat Cardiomyocytes in Culture - a Model System to Study the Plasticity of the Differentiated Cardiac Phenotype at the Molecular and Cellular-Levels. *Trends Cardiovasc. Med.* **1994**, *4*, 187-193.

14. Zick, M.; Rabl, R.; Reichert, A. S. Cristae Formation-Linking Ultrastructure and Function of Mitochondria. *Biochim. Biophys. Acta, Mol. Cell Res.* **2009**, *1793*, 5-19.

15. Fernandez-Vizarra, E.; Lopez-Perez, M. J.; Enriquez, J. A. Isolation of Biogenetically Competent Mitochondria from Mammalian Tissues and Cultured Cells. *Methods* **2002**, *26*, 292-297.

16. Michelsen, U.; von Hagen, J. Isolation of Subcellular Organelles and Structures. *Methods Enzymol.* **2009**, *463*, 305-328.

17. Storrie, B.; Madden, E. A. Isolation of Subcellular Organelles. *Methods Enzymol.* **1990**, *182*, 203-225.

18. Strack, A.; Duffy, C. F.; Malvey, M.; Arriaga, E. A. Individual Mitochondrion Characterization: A Comparison of Classical Assays to Capillary Electrophoresis with Laser-Induced Fluorescence Detection. *Anal. Biochem.* **2001**, *294*, 141-147.

19. Hartwig, S.; Feckler, C.; Lehr, S.; Wallbrecht, K.; Wolgast, H.; Mueller-Wieland, D.; Kotzka, J. A Critical Comparison between Two Classical and a Kit-Based Method for Mitochondria Isolation. *Proteomics* **2009**, *9*, 3209-3214.

20. Kang, D.; Oh, S.; Reschiglian, P.; Moon, M. H. Separation of Mitochondria by Flow Field-Flow Fractionation for Proteomic Analysis. *Analyst* **2008**, *133*, 505-515.

21. Satori, C. P.; Kostal, V.; Arriaga, E. A. Review on Recent Advances in the Analysis of Isolated Organelles. *Anal. Chim. Acta* **2012**, *753*, 8-18.

22. Cetin, B.; Ozer, M. B.; Solmaz, M. E. Microfluidic Bio-Particle Manipulation for Biotechnology. *Biochem. Eng. J.* **2014**, *92*, 63-82.

23. Pasquali, C.; Fialka, I.; Huber, L. A. Subcellular Fractionation, Electromigration Analysis and Mapping of Organelles. *J. Chromatogr. B: Biomed. Sci. Appl* **1999**, *722*, 89-102.

24. Eubel, H.; Lee, C. P.; Kuo, J.; Meyer, E. H.; Taylor, N. L.; Millar, A. H. Free-Flow Electrophoresis for Purification of Plant Mitochondria by Surface Charge. *Plant J.* **2007**, *52*, 583-594.

25. Islinger, M.; Eckerskorn, C.; Voelkl, A. Free-Flow Electrophoresis in the Proteomic Era: A Technique in Flux. *Electrophoresis* **2010**, *31*, 1754-1763.

26. Kostal, V.; Fonslow, B. R.; Arriaga, E. A.; Bowser, M. T. Fast Determination of Mitochondria Electrophoretic Mobility Using Micro Free-Flow Electrophoresis. *Anal. Chem.* **2009**, *81*, 9267-9273.

27. Lu, H.; Gaudet, S.; Schmidt, M. A.; Jensen, K. F. A Microfabricated Device for Subcellular Organelle Sorting. *Anal. Chem.* **2004**, *76*, 5705-5712.

28. Johnson, R. D.; Navratil, M.; Poe, B. G.; Xiong, G.; Olson, K. J.; Ahmadzadeh, H.; Andreyev, D.; Duffy, C. F.; Arriaga, E. A. Analysis of Mitochondria Isolated from Single Cells. *Anal. Bioanal. Chem.* **2007**, *387*, 107-118.

29. Moschallski, M.; Hausmann, M.; Posch, A.; Paulus, A.; Kunz, N.; Duong, T. T.; Angres, B.; Fuchsberger, K.; Steuer, H.; Stoll, D.*; et al.* MicroPrep: Chip-Based Dielectrophoretic Purification of Mitochondria. *Electrophoresis* **2010**, *31*, 2655-2663.

30. Luo, J.; Abdallah, B. G.; Wolken, G. G.; Arriaga, E. A.; Ros, A. Insulator-Based Dielectrophoresis of Mitochondria. *Biomicrofluidics* **2014**, *8*, 021801.

31. Hornig-Do, H. -T.; Guenther, G.; Bust, M.; Lehnartz, P.; Bosio, A.; Wiesner, R. J. Isolation of Functional Pure Mitochondria by Superparamagnetic Microbeads. *Anal. Biochem.* **2009**, *389*, 1-5.

32. Khoshmanesh, K.; Nahavandi, S.; Baratchi, S.; Mitchell, A.; Kalantar-zadeh, K. Dielectrophoretic Platforms for Bio-Microfluidic Systems. *Biosens. Bioelectron.* **2011**, *26*, 1800-1814.

33. Astumian, R. D. Thermodynamics and Kinetics of a Brownian Motor. *Science* **1997**, *276*, 917-922.

34. Haenggi, P.; Marchesoni, F. Artificial Brownian Motors: Controlling Transport on the Nanoscale. *Rev. Mod. Phys.* **2009**, *81*, 387-442.

35. Eichhorn, R.; Reimann, P.; Hanggi, P. Paradoxical Motion of a Single Brownian Particle: Absolute Negative Mobility. *Phys. Rev. E* **2002**, *66*, 066132.

36. Ros, A.; Eichhorn, R.; Regtmeier, J.; Duong, T. T.; Reimann, P.; Anselmetti, D. Brownian Motion - Absolute Negative Particle Mobility. *Nature* **2005**, *436*, 928-928.

37. Eichhorn, R.; Ros, A.; Regtmeier, J.; Duong, T. T.; Reimann, P.; Anselmetti, D. Paradoxical Brownian Motion in a Microfluidic Device: Absolute Negative Mobility. *Eur. Phys. J. : Spec. Top.* **2007**, *143*, 159-164.

38. Eichhorn, R.; Regtmeier, J.; Anselmetti, D.; Reimann, P. Negative Mobility and Sorting of Colloidal Particles. *Soft Matter* **2010**, *6*, 1858-1862.

39. Remcho, V. T.; Vallano, P. T. *RSC Chromatography Monographs, Volume 7 : Capillary Electrochromatography;* Royal Society of Chemistry: Cambridge, GBR, 2001.

40. Ren, X. Q.; Bachman, M.; Sims, C.; Li, G. P.; Allbritton, N. Electroosmotic Properties of Microfluidic Channels Composed of Poly(dimethylsiloxane). *J. Chromatogr. B* **2001**, *762*, 117-125.

41. Kleinstreuer, C. *Microfluidics and Nanofluidics : Theory and Selected Applications;* John Wiley & Sons, Incorporated: Somerset, NJ, USA, 2013.

42. Hellmich, W.; Regtmeier, J.; Duong, T. T.; Ros, R.; Anselmetti, D.; Ros, A. Poly(oxyethylene) Based Durface Coatings for Poly(dimethylsiloxane) Microchannels. *Langmuir* **2005**, *21*, 7551-7557.

43. Rodriguez, M. A.; Armstrong, D. W. Separation and Analysis of Colloidal/Nano-Particles Including Microorganisms by Capillary Electrophoresis: A Fundamental Review. *J. Chromatogr. B: Anal. Technol. Biomed. Life Sci.* **2004**, *800*, 7-25.

44. Dash, S.; Mohanty, S. Dielectrophoretic Separation of Micron and Submicron Particles: A Review. *Electrophoresis* **2014**, *35*, 2656-2672.

45. Pohl, H. A. Dielectrophoresis, a New Technique for Studying Cells and Organelles. *Bull. Am. Phys. Soc.* **1970**, *15*, 1362-&.

46. Pethig, R. Review Article-Dielectrophoresis: Status of the Theory, Technology, and Applications. *Biomicrofluidics* **2010**, *4*, 022811.

47. Jones, T. B. *Electromechanics of Particles;* Cambridge University Press: New York, USA, 1995.

48. Jones, T. B. Basic Theory of Dielectrophoresis and Electrorotation. *IEEE Eng. Med. Biol. Mag.* **2003**, *22*, 33-42.

49. Bhattacharya, S.; Chao, T. -C.; Ros, A. Insulator-Based Dielectrophoretic Single Particle and Single Cancer Cell Trapping. *Electrophoresis* **2011**, *32*, 2550-2558.

50. Weiss, N. G.; Jones, P. V.; Mahanti, P.; Chen, K. P.; Taylor, T. J.; Hayes, M. A. Dielectrophoretic mobility determination in DC insulator-based dielectrophoresis. *Electrophoresis* **2011**, *32*, 2292-2297.

51. Bogunovic, L.; Eichhorn, R.; Regtmeier, J.; Anselmetti, D.; Reimann, P. Particle Sorting by a Structured Microfluidic Ratchet Device with Tunable Selectivity: Theory and Experiment. *Soft Matter* **2012**, *8*, 3900-3907.

52. Marquet, C.; Buguin, A.; Talini, L.; Silberzan, P. Rectified Motion of Colloids in Asymmetrically Structured Channels. *Phys. Rev. Lett.* **2002**, *88*, 168301.

53. Loutherback, K.; Puchalla, J.; Austin, R. H.; Sturm, J. C. Deterministic Microfluidic Ratchet. *Phys. Rev. Lett.* **2009**, *102*, 045301.

54. Sturm, J. C.; Cox, E. C.; Comella, B.; Austin, R. H. Ratchets in Hydrodynamic Flow: More Than Waterwheels. *Interface Focus* **2014**, *4*, UNSP 20140054.

55. Nakano, A.; Chao, T. -C.; Camacho-Alanis, F.; Ros, A. Immunoglobulin G and Bovine Serum Albumin Streaming Dielectrophoresis in a Microfluidic Device. *Electrophoresis* **2011**, *32*, 2314-2322.

56. Camacho-Alanis, F.; Gan, L.; Ros, A. Transitioning Streaming to Trapping in DC Insulator-Based Dielectrophoresis for Biomolecules. *Sens. Actuators, B* **2012**, *173*, 668-675.

57. Asbury, C. L.; Diercks, A. H.; van den Engh, G. Trapping of DNA by Dielectrophoresis. *Electrophoresis* **2002**, *23*, 2658-2666.

58. Hughes, M. P. Strategies for Dielectrophoretic Separation in Laboratory-On-a-Chip Systems. *Electrophoresis* **2002**, *23*, 2569-2582.

59. Pethig, R.; Menachery, A.; Pells, S.; De Sousa, P. Dielectrophoresis: A Review of Applications for Stem Cell Research. *J. Biomed. Biotechnol.* **2010**, 182581.

60. Gagnon, Z. R. Cellular Dielectrophoresis: Applications to the Characterization, Manipulation, Separation and Patterning of Cells. *Electrophoresis* **2011**, *32*, 2466-2487.

61. Ho, C. -T.; Lin, R. -Z.; Chang, W. -Y.; Chang, H. -Y.; Liu, C. -H. Rapid Heterogeneous Liver-Cell On-Chip Patterning via the Enhanced Field-Induced Dielectrophoresis Trap. *Lab Chip* **2006**, *6*, 724-734.

62. Sebastian, A.; Buckle, A.; Markx, G. H. Tissue Engineering with Electric Fields: Immobilization of Mammalian Cells in Multilayer Aggregates Using Dielectrophoresis. *Biotechnol. Bioeng.* **2007**, *98*, 694-700.

63. Yang, M.; Zhang, X. Electrical Assisted Patterning of Cardiac Myocytes with Controlled Macroscopic Anisotropy Using a Microfluidic Dielectrophoresis Chip. *Sens. Actuators, A* **2007**, *135*, 73-79.

64. Becker, F. F.; Wang, X. B.; Huang, Y.; Pethig, R.; Vykoukal, J.; Gascoyne, P. R. C. Separation of Human Breast-Cancer Cells from Blood by Differential Dielectric Affinity. *Proc. Natl. Acad. Sci. U. S. A.* **1995**, *92*, 860-864.

65. Gascoyne, P.; Satayavivad, J.; Ruchirawat, M. Microfluidic Approaches to Malaria Detection. *Acta Trop.* **2004**, *89*, 357-369.

66. Gascoyne, P. R. C.; Noshari, J.; Anderson, T. J.; Becker, F. F. Isolation of Rare Cells from Cell Mixtures by Dielectrophoresis. *Electrophoresis* **2009**, *30*, 1388-1398.

67. del Carmen Jaramillo, M.; Torrents, E.; Martinez-Duarte, R.; Madou, M. J.; Juarez, A. On-Line Separation of Bacterial Cells by Carbon-Electrode Dielectrophoresis. *Electrophoresis* **2010**, *31*, 2921-2928.

68. Zhu, K.; Kaprelyants, A. S.; Salina, E. G.; Markx, G. H. Separation by Dielectrophoresis of Dormant and Nondormant Bacterial Cells of Mycobacterium Smegmatis. *Biomicrofluidics* **2010**, *4*, 022809.

69. Abdallah, B. G.; Chao, T.; Kupitz, C.; Fromme, P.; Ros, A. Dielectrophoretic Sorting of Membrane Protein Nanocrystals. *ACS Nano* **2013**, *7*, 9129-9137.

70. Braff, W. A.; Pignier, A.; Buie, C. R. High Sensitivity Three-Dimensional Insulator-Based Dielectrophoresis. *Lab Chip* **2012**, *12*, 1327-1331.

71. Lapizco-Encinas, B. H.; Simmons, B. A.; Cummings, E. B.; Fintschenko, Y. Dielectrophoretic Concentration and Separation of Live and Dead Bacteria in an Array of Insulators. *Anal. Chem.* **2004**, *76*, 1571-1579.

72. Lapizco-Encinas, B. H.; Simmons, B. A.; Cummings, E. B.; Fintschenko, Y. Insulator-Based Dielectrophoresis for the Selective Concentration and Separation of Live Bacteria in Water. *Electrophoresis* **2004**, *25*, 1695-1704.

73. Nakano, A.; Ros, A. Protein Dielectrophoresis: Advances, Challenges, and Applications. *Electrophoresis* **2013**, *34*, 1085-1096.

74. Shafiee, H.; Caldwell, J. L.; Sano, M. B.; Davalos, R. V. Contactless Dielectrophoresis: A New Technique for Cell Manipulation. *Biomed. Microdevices* **2009**, *11*, 997-1006.

75. Shafiee, H.; Caldwell, J. L.; Davalos, R. V. A Microfluidic System for Biological Particle Enrichment Using Contactless Dielectrophoresis. *JALA* **2010**, *15*, 224-232.

76. Sano, M. B.; Caldwell, J. L.; Davalos, R. V. Modeling and Development of a Low Frequency Contactless Dielectrophoresis (cDEP) Platform to Sort Cancer Cells from Dilute Whole Blood Samples. *Biosens. Bioelectron.* **2011**, *30*, 13-20.

77. Sano, M. B.; Gallo-Villanueva, R. C.; Lapizco-Encinas, B. H.; Davalos, R. V. Simultaneous Electrokinetic Flow and Dielectrophoretic Trapping Using Perpendicular Static and Dynamic Electric Fields. *Microfluid. Nanofluid.* **2013**, *15*, 599-609.

78. Bhattacharya, S. K.; Thakar, J. H.; Johnson, P. L.; Shanklin, D. R. Isolation of Skeletal-Muscle Mitochondria from Hamsters using an Ionic Medium Containing Ethylenediarninetetraacetic Acid and Nagarse. *Anal. Biochem.* **1991**, *192,* 344-349.

79. Madsen, K.; Ertbjerg, P.; Pedersen, P. K. Calcium Content and Respiratory Control Index of Isolated Skeletal Muscle Mitochondria: Effects of Different Isolation Media. *Anal. Biochem.* **1996***, 237*, 37-41.

80. Frezza, C.; Cipolat, S.; Scorrano, L. Organelle Isolation: Functional Mitochondria from Mouse Liver, Muscle and Cultured Filroblasts. *Nat. Protoc.* **2007***, 2*, 287-295.

81. Greif, D.; Galla, L.; Ros, A.; Anselmetti, D. Single Cell Analysis in Full Body Quartz Glass Chips with Native UV Laser-Induced Fluorescence Detection. *J. Chromatogr. A* **2008**, *1206*, 83-88.

82. Viefhues, M.; Manchanda, S.; Chao, T. -C.; Anselmetti, D.; Regtmeier, J.; Ros, A. Physisorbed Surface Coatings for Poly(dimethylsiloxane) and Quartz Microfluidic Devices. *Anal. Bioanal. Chem.* **2011**, *401*, 2113-2122.

83. Asami, K.; Irimajiri, A.; Hanai, T.; Shiraishi, N.; Utsumi, K. Dielectric Analysis of Mitochondria Isolated from Rat-Liver .1. Swollen Mitoplasts as Simulated by a Single-Shell Model. *Biochim. Biophys. Acta* **1984**, *778*, 559-569.

84. Asami, K.; Irimajiri, A. Dielectric Analysis of Mitochondria Isolated from Rat-Liver .2. Intact Mitochondria as Simulated by a Double-Shell Model. *Biochim. Biophys. Acta* **1984**, *778*, 570-578.

85. Joshi, R. P.; Hu, Q.; Schoenbach, K. H. Modeling Studies of Cell Response to Ultrashort, High-Intensity Electric Fields-Implications for Intracellular Manipulation. *IEEE Trans. Plasma Sci.* **2004**, *32,* 1677-1686.

86. Vajrala, V.; Claycomb, J. R.; Sanabria, H.; Miller, J. H., Jr. Effects of Oscillatory Electric Fields on Internal Membranes: An Analytical Model. *Biophys. J.* **2008**, *94*, 2043-2052.

87. Fuller, K. M.; Arriaga, E. A. Capillary Electrophoresis Monitors Changes in the Electrophoretic Behavior of Mitochondrial Preparations. *J. Chromatogr. B: Anal. Technol. Biomed. Life Sci.* **2004**, *806*, 151-159.

88. Zhang, C.; Khoshmanesh, K.; Tovar-Lopez, F. J.; Mitchell, A.; Wlodarski, W.; Klantar-zadeh, K. Dielectrophoretic Separation of Carbon Nanotubes and Polystyrene Microparticles. *Microfluid. Nanofluid.* **2009**, *7*, 633-645.

89. Chaurey, V.; Rohani, A.; Su, Y. -H.; Liao, K. -T.; Chou, C. -F.; Swami, N. S. Scaling Down Constriction-Based (Electrodeless) Dielectrophoresis Devices for Trapping Nanoscale Bioparticles in Physiological Media of High-Conductivity. *Electrophoresis* **2013**, *34*, 1097-1104.

90. Nakano, A.; Luo, J.; Ros, A. Temporal and Spatial Temperature Measurement in Insulator-Based Dielectrophoretic Devices. *Anal. Chem.* **2014**, *86*, 6516-6524.

91. Gencoglu, A.; Camacho-Alanis, F.; Nguyen, V. T.; Nakano, A.; Ros, A.; Minerick, A. R. Quantification of pH Gradients and Implications in Insulator-Based Dielectrophoresis of Biomolecules. *Electrophoresis* **2011**, *32*, 2436-2447.

92. Lim, T. -S.; Davila, A.; Wallace, D. C.; Burke, P. Assessment of Mitochondrial Membrane Potential using an On-Chip Microelectrode in a Microfluidic Device. *Lab Chip* **2010**, *10*, 1683-1688.

93. Rogers, G. W.; Brand, M. D.; Petrosyan, S.; Ashok, D.; Elorza, A. A.; Ferrick, D. A.; Murphy, A. N. High Throughput Microplate Respiratory Measurements Using Minimal Quantities Of Isolated Mitochondria. *PLoS One* **2011**, *6*, e21746.

94. Sun, L.; Zhu, G.; Li, Y.; Yang, P.; Dovichi, N. J. Coupling Methanol Denaturation, Immobilized Trypsin Digestion, and Accurate Mass and Time Tagging for Liquid-Chromatography-Based Shotgun Proteomics of Low Nanogram Amounts of RAW 264.7 Cell Lysate. *Anal. Chem.* **2012**, *84*, 8715-8721.

95. Stuurman, N. ImageJ plugin MTrack 2, 2009. MTrack2. http://valelab.ucsf.edu/~nstuurman/ijplugins/MTrack2.html (accessed Oct 16, 2014).

96. Cordelières, F. P. ImageJ plugin Manual Tracking, 2005. Manual Tracking. http://rsb.info.nih.gov.ezproxy1.lib.asu.edu/ij/plugins/track/track.html (accessed Oct 16, 2014).

97. Fernandez, D. P.; Goodwin, A. R. H.; Lemmon, E. W.; Sengers, J. M. H. L.; Williams, R. C. A Formulation for the Static Permittivity of Water and Steam at Temperatures from 238 K to 873 K at Pressures up to 1200 MPa, Including Derivatives and Debye-Huckel Coefficients. *J. Phys. Chem. Ref. Data* **1997**, *26*, 1125-1166.

98. Sun, G.; Chen, G.; Liu, Z.; Chen, M. Preparation, Crystallization, Electrical Conductivity and Thermal Stability of Syndiotactic Polystyrene/Carbon Nanotube Composites. *Carbon* **2010**, *48*, 1434-1440.

99. Qi, X. -Y.; Yan, D.; Jiang, Z.; Cao, Y. -K.; Yu, Z. -Z.; Yavari, F.; Koratkar, N. Enhanced Electrical Conductivity in Polystyrene Nanocomposites at Ultra-Low Graphene Content. *ACS Appl. Mater. Interfaces* **2011**, *3*, 3130-3133.

100. Regtmeier, J.; Grauwin, S.; Eichhorn, R.; Reimann, P.; Anselmetti, D.; Ros, A. Acceleration of Absolute Negative Mobility. *J. Sep. Sci.* **2007**, *30*, 1461-1467.

101. Cesaro-Tadic, S.; Dernick, G.; Juncker, D.; Buurman, G.; Kropshofer, H.; Michel, B.; Fattinger, C.; Delamarche, E. High-Sensitivity Miniaturized Immunoassays for Tumor Necrosis Factor a Using Microfluidic Systems. *Lab Chip* **2004**, *4*, 563-569.

102. Giddings, J. C. *Unified separation science;* Wiley New York etc: 1991.

103. Coburn, B.; Grassl, G. A.; Finlay, B. B. Salmonella, the Host and Disease: A Brief Review. *Immunol. Cell Biol.* **2007**, *85*, 112-118.

104. Bajpai, V. K.; Baek, K. -H.; Kang, S. C. Control of Salmonella in Foods by Using Essential Oils: A Review. *Food Res. Int.* **2012**, *45*, 722-734.

105. Kong, W.; Weatherspoon, N.; Shi, Y. Molecular Mechanism for Establishment of Signal-Dependent Regulation in the PhoP/PhoQ System. *J. Biol. Chem.* **2008**, *283*, 16612-16621.

106. He, X.; Hu, C.; Guo, Q.; Wang, K.; Li, Y.; Shangguan, J. Rapid and Ultrasensitive Salmonella Typhimurium Quantification using Positive Dielectrophoresis Driven On-Line Enrichment and Fluorescent Nanoparticles Label. *Biosens. Bioelectron.* **2013**, *42*, 460-466.

107. Cormack, B. P.; Valdivia, R. H.; Falkow, S. FACS-Optimized Mutants of the Green Fluorescent Protein (GFP). *Gene* **1996**, *173*, 33-38.

108. Xu, J.; Vaillant, R.; Attinger, D. Use of a Porous Membrane for Gas Bubble Removal in Microfluidic Channels: Physical Mechanisms and Design Criteria. *Microfluid. Nanofluid.* **2010**, *9*, 765-772.

109. Zheng, W.; Wang, Z.; Zhang, W.; Jiang, X. A Simple PDMS-Based Microfluidic Channel Design that Removes Bubbles for Long-Term On-Chip Culture of Mammalian Cells. *Lab Chip* **2010**, *10*, 2906-2910.

APPENDIX A

SUPPLEMENTAL MATERIAL FOR CHAPTER 4

Appendix A 1: Determination of the EK mobility for the 4.4-μm polystyrene beads

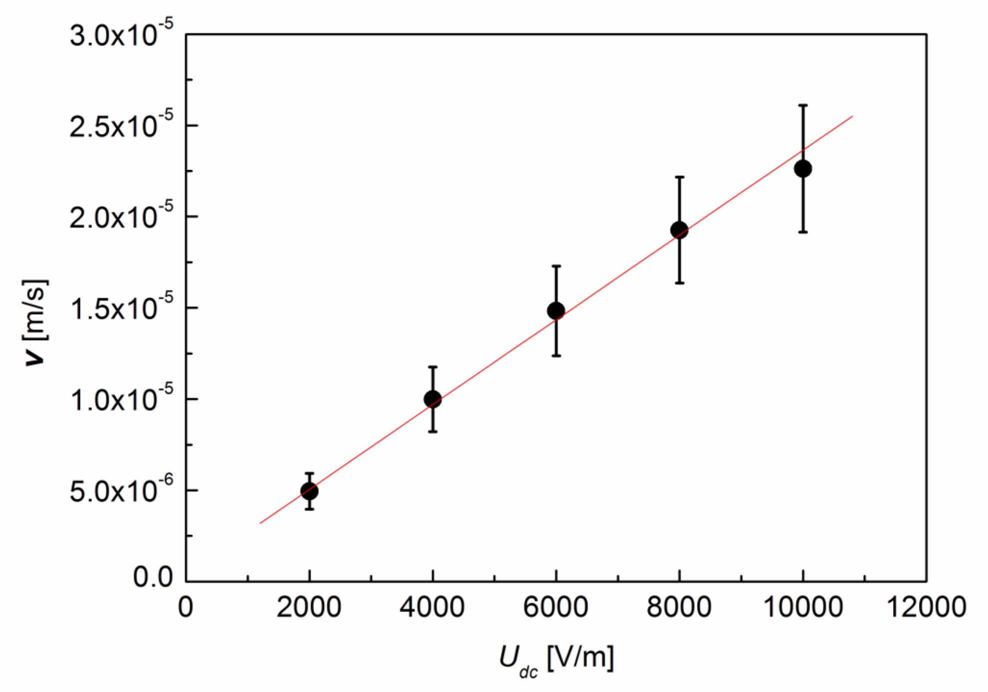

Figure 4-S1. Migration velocity ($\boldsymbol{v}$) vs. DC potential (U_{dc}) for 4.4-μm beads. The experiment was conducted in a post-free straight channel. Each data point was obtained by tracking over 100 individual trajectories. The error bars are the standard deviations of the velocities at each DC voltage.

The slope of the best-fit line for the data set shown in Figure 4-S1 was 2.2 ±0.33 $\times 10^{-9}$ m^{2} ·V^{-1} s^{-1}, which was the μ_{ek} for the 4.4-μm polystyrene beads at the experimental conditions described in Chapter 4.

Appendix A 2: The equations used in COMSOL

Equations:

$$\boldsymbol{E} = (Ex, Ey) \qquad (\mathrm{A}-1)$$

$$E^2 = (Ex, Ey).(Ex, Ey) = Ex^2 + Ey^2 \qquad (\mathrm{A}-2)$$

$$\nabla \boldsymbol{E}^2 = \left(\frac{\delta E^2}{\delta x}, \frac{\delta E^2}{\delta y}\right) = \left(\frac{\delta(Ex^2+Ey^2)}{\delta x}, \frac{\delta(Ex^2+Ey^2)}{\delta y}\right) \qquad (\mathrm{A}-3)$$

$$|\nabla \boldsymbol{E}^2| = \left(\left[\frac{\delta(Ex^2+Ey^2)}{\delta x}\right]^2 + \left[\frac{\delta(Ex^2+Ey^2)}{\delta y}\right]^2\right)^{0.5} \qquad (\mathrm{A}-4)$$

The expressions in COMSOL:

For Eq. $(\mathrm{A}-1)$:

$Ex = \mathrm{ec.Ex},$

$Ey = \mathrm{ec.Ey} \qquad (\mathrm{A}-5)$

For Eq. $(\mathrm{A}-3)$:

$\frac{\delta E^2}{\delta x} = \mathrm{d(ec.Ex\text{^}2 + ec.Ey\text{^}2, x)}$

$\frac{\delta E^2}{\delta y} = \mathrm{d(ec.Ex\text{^}2 + ec.Ey\text{^}2, y)} \qquad (\mathrm{A}-6)$

For Eq. $(\mathrm{A}-4)$:

$|\nabla \boldsymbol{E}^2| = \mathrm{(d(ec.Ex\text{^}2 + ec.Ey\text{^}2, x)\text{^}2 + d(ec.Ex\text{^}2 + ec.Ey\text{^}2, y)\text{^}2)\text{^}0.5} \qquad (\mathrm{A}-7)$

Appendix A 3: The equations for the square waveform in COMSOL

The square waveform shown in Figure 4-1(c) is realized in COMSOL by a rectangle function and an analytic function.

The rectangle function defines an x range = [Lower limit, Upper limit] in which y = 1. Outside this range, y = 0. This actually defines the time duration for each half driving period which will be needed in the analytic function.

The analytic function modifies the rectangle function into the waveform in need. Firstly, a letter is assigned to define the variable in the functions. In my case, the functions are created for the time-dependent studies, so the variable is the time, *t*. Next, the ratio between the value of $U_{dc} + U_{ac}$ and $U_{dc} - U_{ac}$ is calculated to modify the rectangle function. Then the duration of a complete driving period can be defined by the lower and the upper limits in the analytic function. Choose "make periodic" if more than 1 driving period is needed.

For example, to define a waveform with $|U_{ac}| = 450$ V/cm and $U_{dc} = 50$ V/cm with each half driving period lasting 5 seconds, a voltage equal to 450 V/cm (*e.g.* $\mathrm{U_{inlet}}$) is firstly defined in Parameters to be applied in the physical model. Then, for the rectangle function (rect1), the lower limit = 0 and the upper limit = 5. In the analytic function (an1), the lower limit = 0 and the upper limit = 10 are used to represent a complete driving period. According to the ratio of $U_{dc} + U_{ac}$ over $U_{dc} - U_{ac}$ and the waveform as shown in Figure 4-1(c), the expression of the analytic function is set as: 1-(9/5)*rect1(t).

Therefore, based on Eq. $(\mathrm{A}-5)$, the result of *Electric Currents* module integrated in the *Creeping Flow* module for the time-dependent study is expressed as

$$Ex = \mathrm{ec.Ex} * (\mathrm{an1(t[1/s])}),$$

$$Ey = \mathrm{ec.Ey} * (\mathrm{an1(t[1/s])}), \qquad (\mathrm{A}-8)$$

Based on Eq. $(\mathrm{A}-6)$, the result of *Electric Currents* module integrated in the *Particle Tracing for Fluid Flow* module for the time-dependent study is expressed as

$$\frac{\delta E^2}{\delta x} = \mathrm{d((ec.Ex} * \left(\mathrm{an1(t[1/s])}\right))\text{^}2 + (\mathrm{ec.Ey} * \left(\mathrm{an1(t[1/s])}\right))\text{^}2, \mathrm{x})$$

$$\frac{\delta E^2}{\delta y} = \mathrm{d((ec.Ex} * \left(\mathrm{an1(t[1/s])}\right))\text{^}2 + (\mathrm{ec.Ey} * \left(\mathrm{an1(t[1/s])}\right))\text{^}2, \mathrm{y}) \qquad (\mathrm{A}-9)$$

Appendix A 4: Comparison of the simulation results with and without the Brownian motion

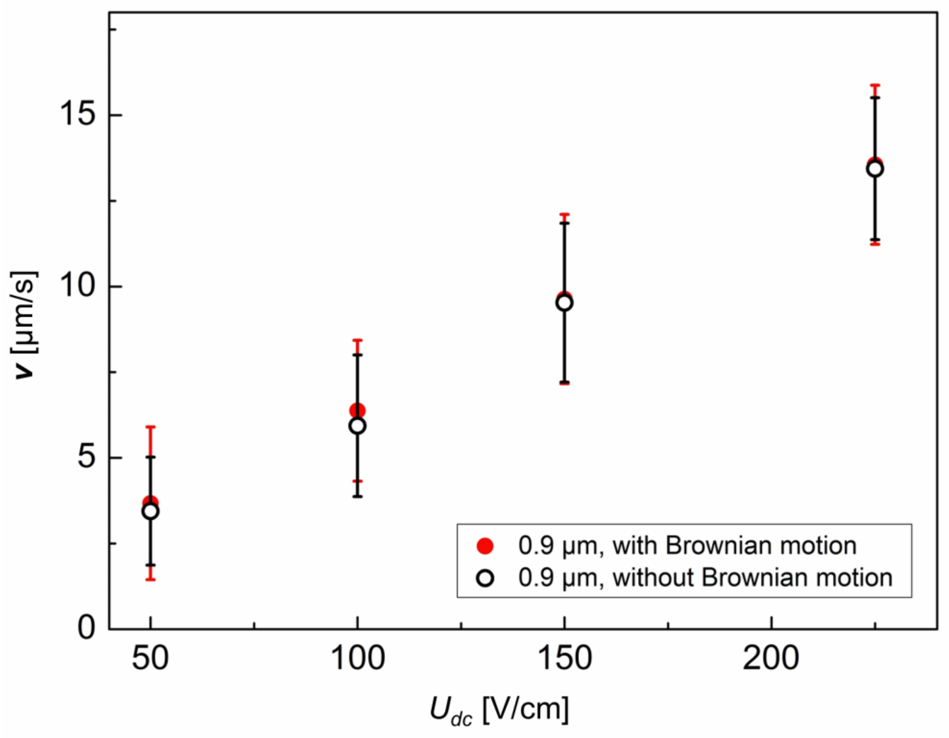

Figure 4-S2. The migration velocities of 0.9-µm beads simulated with (red dot) and without (black circle) the Brownian motion. U_{ac} = 275 V/cm. The error bars represent the standard deviations of the velocities obtained at each U_{dc} from tracking 20 individual trajectories for the simulation results.

Based on the simulation results shown in Figure 4-S2, there is no significant difference between the velocities simulated with Brownian motion (red dot) and that without Brownian motion (black circle). This indicates that the Brownian motion does not influence the migration velocity significantly at the applied conditions.

APPENDIX B

SUPPLEMENTAL MATERIAL FOR CHAPTER 5

Appendix B 1: Determination of the EK mobility for 0.3- and 0.9-μm polystyrene beads

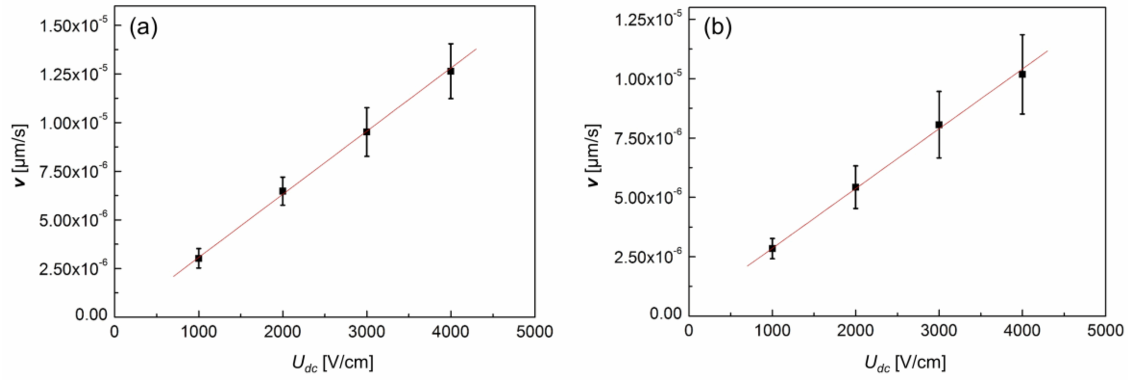

Figure 5-S1. Migration velocity ($\boldsymbol{v}$) vs. DC potential (U_{dc}) for (a) 0.3-μm and (b) 0.9-μm polystyrene beads. Both velocity files were obtained in the post-free region of 3 microchannels. Each data point was averaged from the migration velocities by tracking 60 individual bead trajectories with 20 trajectories per channel. The error bars are the standard deviations of the velocitites at each DC voltage.

The EK mobility of 0.3-μm beads ($\mu_{ek\_0.3\_\mu m}$) at the experimental conditions described in Chapter 5 was determined by the slope of the best-fit line for the data set shown in Figure 5-S1(a), which was $3.24 \pm 0.41 \times 10^{-9}$ m^{2} ·V^{-1} s^{-1}. Also, the EK mobility of 0.9-μm beads ($\mu_{ek\_0.9\_\mu m}$) was determined by the slope of the best-fit line in Figure 5-S1(b) and the value was $2.52 \pm 0.45 \times 10^{-9}$ m^{2} ·V^{-1} s^{-1}.

Appendix B 2: Determination of the size distribution of mitochondria

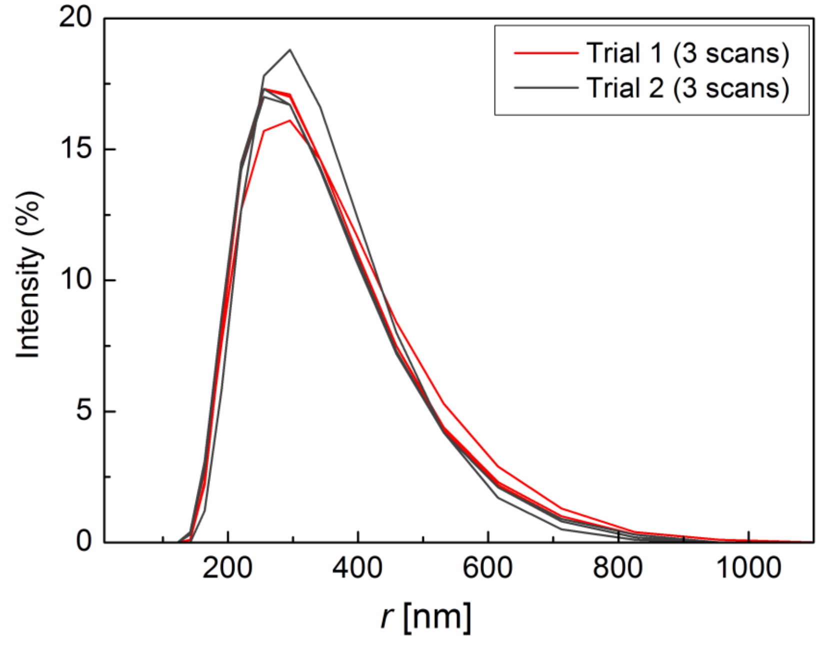

Figure 5-S2.Size distribution of the isolated C57BL/6 mouse hepatic mitochondria determined by a DLS instrument.

Two trials with 3 scans per trial were conducted to determine the size distribution of mitochondria. The hydrodynamic radius (*r*) of the mitochondria sample was determined to be 150 - 800 nm.

Appendix B 3: The equations for the square waveform in COMSOL

The square waveform shown in Figure 5-2(a) as applied in experiments is realized in COMSOL by a rectangle function, a waveform function and two analytic functions.

Firstly, a waveform shown in Figure 4-1(c) is created by a rectangle function (rect1) and an analytic function (an1) as described in Appendix A 3. Then the overlaid AC signal is created by a waveform function (wv1) and the second analytic function (an2). For the waveform function, a sine signal is chosen with the angular frequency expressed as: 2*pi[rad]**f*[Hz], where "pi" means π, and *f* is the frequency defined in Parameter with unit of Hz. For the second analytic function, it is expressed as rect1(t)*wv1(t) so that the AC signal is only overlaid with the half driving period of interest.

As described in Chapter 5, the AC signal is integrated in *Particle Tracing for Fluid Flow* module only. Therefore, the result of *Electric Currents* module integrated in the *Creeping Flow* module for the time-dependent study is the same as expressed by Eq. $(\mathrm{A}-8)$. Based on Eq. $(\mathrm{A}-6)$, the result of *Electric Currents* module integrated in the *Particle Tracing for Fluid Flow* module for the time-dependent study is expressed as

$$\frac{\delta E^2}{\delta x} = \mathrm{d}((\mathrm{ec.Ex} * (\mathrm{an1}(\mathrm{t}[1/\mathrm{s}]) + \mathrm{an2}(\mathrm{t}[1/\mathrm{s}])))\text{\^{}}2 + (\mathrm{ec.Ey} * (\mathrm{an1}(\mathrm{t}[1/\mathrm{s}]) + \mathrm{an2}(\mathrm{t}[1/\mathrm{s}])))\text{\^{}}2, \mathrm{x})$$

$$\frac{\delta E^2}{\delta y} = \mathrm{d}((\mathrm{ec.Ex} * (\mathrm{an1}(\mathrm{t}[1/\mathrm{s}]) + \mathrm{an2}(\mathrm{t}[1/\mathrm{s}])))\text{\^{}}2 + (\mathrm{ec.Ey} * (\mathrm{an1}(\mathrm{t}[1/\mathrm{s}]) + \mathrm{an2}(\mathrm{t}[1/\mathrm{s}])))\text{\^{}}2, \mathrm{y}) \qquad (\mathrm{B}-1)$$

Appendix B 4: Comparison of the simulation results obtained with and without the AC signal

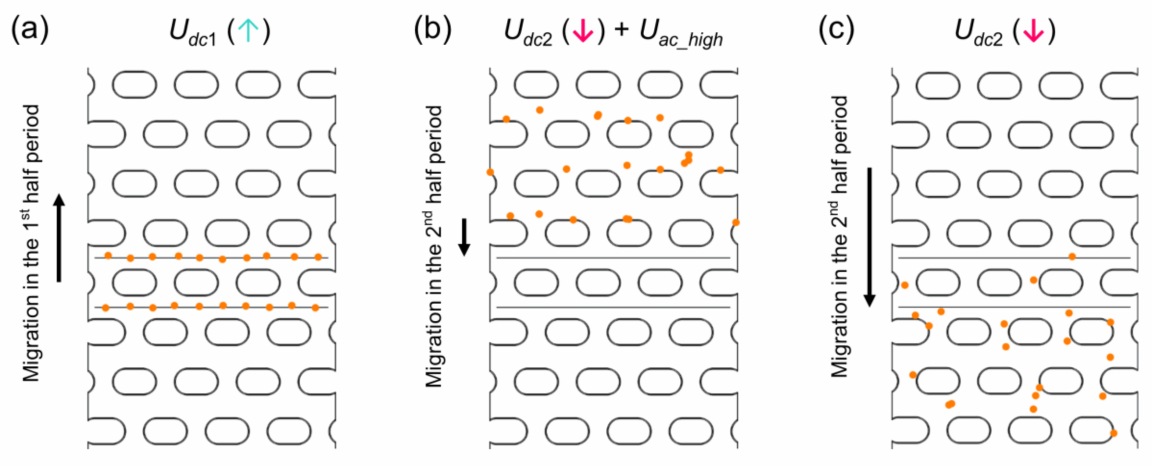

Figure 5-S3. Numerical modeling results simulated with AC component vs. without AC component. The simulation was performed with the 0.9-μm-diameter particles but the diameter depicted in the above figures was enlarged to 3 μm for a better view. The migration direction in each half period was indicated by a black arrow. (a) All particles were released with zero initial velocity at the two inlets indicated by the horizontal lines. Then, U_{dc1} = -40 V/cm (pointing upwards as indicated by the blue arrow) was applied in the first half driving period and all particles moved upwards. (b) In the second half period, U_{dc2} = 60 V/cm (pointing downwards as indicated by the pink arrow) was applied with the overlapping of U_{ac_high} = 800 V/cm at 30 kHz. Therefore, particles moved downwards and they were trapped by the nearby posts or at the gaps which they cannot surpass due to the strong nDEP repulsion. When the entire driving period ended, the net migration direction of the particles pointed upwards. Meanwhile, the net driving DC pointed downwards because $|U_{dc2}| > |U_{dc1}|$. Therefore, the dANM migration behavior was observed for the particles. (c) Upon the removal of the AC component U_{ac_high} which was applied in (b), particles resumed the normal migration which was in the same direction as the net driving DC.

As demonstrated in Figure 5-S3(a) and (b), the application of an AC component U_{ac_high} with an adequate frequency can help induce the dANM migration for particles. Without the AC component, the DC signal is not capable of supplying strong-enough DEP trapping force and particles can only exhibit the normal migration behavior (Figure 5-S3(a) and (c)).

Appendix B 5: A sample calculation for the resolution of a dANM-based separation

According to the simulation results shown in Figure 5-3, the 0.3-µm-diameter particles move in the direction of the net force (similar to Figure 5-S3(a) and (c)) while the 0.9-µm-diameter particles moved in the direction against the net force (similar to Figure 5-S3(a) and (b)). Therefore, the distance between two size groups ($\mathit{\Delta X}$) can be calculated as:

$$\mathit{\Delta X} = |\mathit{\Delta} d_{0.9\_\mu m} - \mathit{\Delta} d_{0.3\_\mu m}| \qquad \text{(B} - 2\text{)}$$

The subscripts indicate the corresponding particle size. The distance migrated by each group of the same particle size ($\mathit{\Delta} d$) can be calculated by the average migration distance of the particles in the same size group:

$$\mathit{\Delta} d = \frac{1}{n}\sum_{i=1}^{n} \mathit{\Delta} x_{(i)} \qquad \text{(B} - 3\text{)}$$

where n indicates the total number of particles being tracked and $\mathit{\Delta} x_i$ is the distance migrated by the i^{th} particle:

$$\mathit{\Delta} x_{(i)} = \mathit{\Delta} x_{(i)final} - \mathit{\Delta} x_{(i)initial} \qquad \text{(B} - 4\text{)}$$

where $\mathit{\Delta} x_{(i)final}$ and $\mathit{\Delta} x_{(i)initial}$ are the coordinates of the i^{th} particle at the final and the initial time step along the flow direction, respectively.

The effective zone width w for each size group can be approximated as the distance between the farthest particle position x_{max} and the nearest particle position x_{min}:

$$w = |x_{max} - x_{min}| \qquad \text{(B} - 5\text{)}$$

A set of coordinates for 0.3- and 0.9-µm-diameter particles obtained from simulation is provide in Table 5-S1. The applied conditions were as follows: each half driving period lasted for 10 seconds; in the 1st half period, U_{dc} = -40 V/cm; in the 2nd half period, U_{dc} = 60 V/cm, U_{ac} = 800 V/cm at 30 kHz.

Table 5-S1. Coordinates for 0.9- and 0.3-μm-diameter particles from simulation.

i	0.9-μm-diameter particle		0.3-μm-diameter particle	
	$x_{(i)initial}$ [μm]	$x_{(i)final}$ [μm]	$x_{(i)initial}$ [μm]	$x_{(i)final}$ [μm]
1	60.064	115.56	98.443	58.417
2	61.14	115.87	122.34	74.772
3	40.629	115.49	118.79	74.167
4	39.968	97.484	102.34	74.798
5	39.988	95.62	123.03	119.82
6	60.659	95.597	99.119	76.995
7	60.932	136.41	98.89	56.684
8	40.886	95.246	122.61	92.171
9	40.846	95.742	117.55	77.609
10	40.577	95.529	98.77	78.739
11	59.499	120.89	105.49	118.47
12	60.232	122.96	115.94	103.68
13	60.949	115.54	100.49	58.816
14	40.74	115.65	118.02	67.213
15	60.178	115.55	124.21	61.406
16	60.636	115.62	99.217	68.144
17	40.863	95.683	106.25	78.088
18	60.464	118.18	121.05	80.049
19	40.205	118.33	100.31	72.136
20	39.985	75.961	119.83	63.761

By processing the data in Table 5-S1 according to Eq. $(\mathrm{B}-3)$, the distance that each size group has migrated could be obtained:

$$\Delta d_{0.9\_\mu m} = \frac{1}{20}\sum_{i=1}^{20} \Delta x_{(i)0.9\_\mu m} = 58.17\ \mu m$$

$$\Delta d_{0.3\_\mu m} = \frac{1}{20}\sum_{i=1}^{20} \Delta x_{(i)0.3\_\mu m} = -32.84\ \mu m$$

Based on Eq. $(\mathrm{B}-5)$, the effective zone width for each size group at the final time step can be calculated as follows:

$$w_{0.9\_\mu m} = |x_{max} - x_{min}|_{0.9\_\mu m} = 60.45\ \mu m$$

$$w_{0.3\_\mu m} = |x_{max} - x_{min}|_{0.3\_\mu m} = 63.14\ \mu m$$

Combining the above values and Eq. $(\mathrm{B}-2)$ into Eq. $(5-3)$ yields:

$$R_s = \frac{2\Delta X}{w_{0.9\_\mu m} + w_{0.3\_\mu m}} = \frac{2\times(58.17+32.84)}{60.45+63.14} = 1.47 \approx 1.5$$

which indicates a good baseline separation. Note that this resolution is achieved after just one driving period which lasted for only 20 seconds. Since the two size groups of particles can be directed into two opposite migration directions, an excellent baseline separation can be easily achieved with more than one driving periods.

APPENDIX C

COPYRIGHT PERMISSION

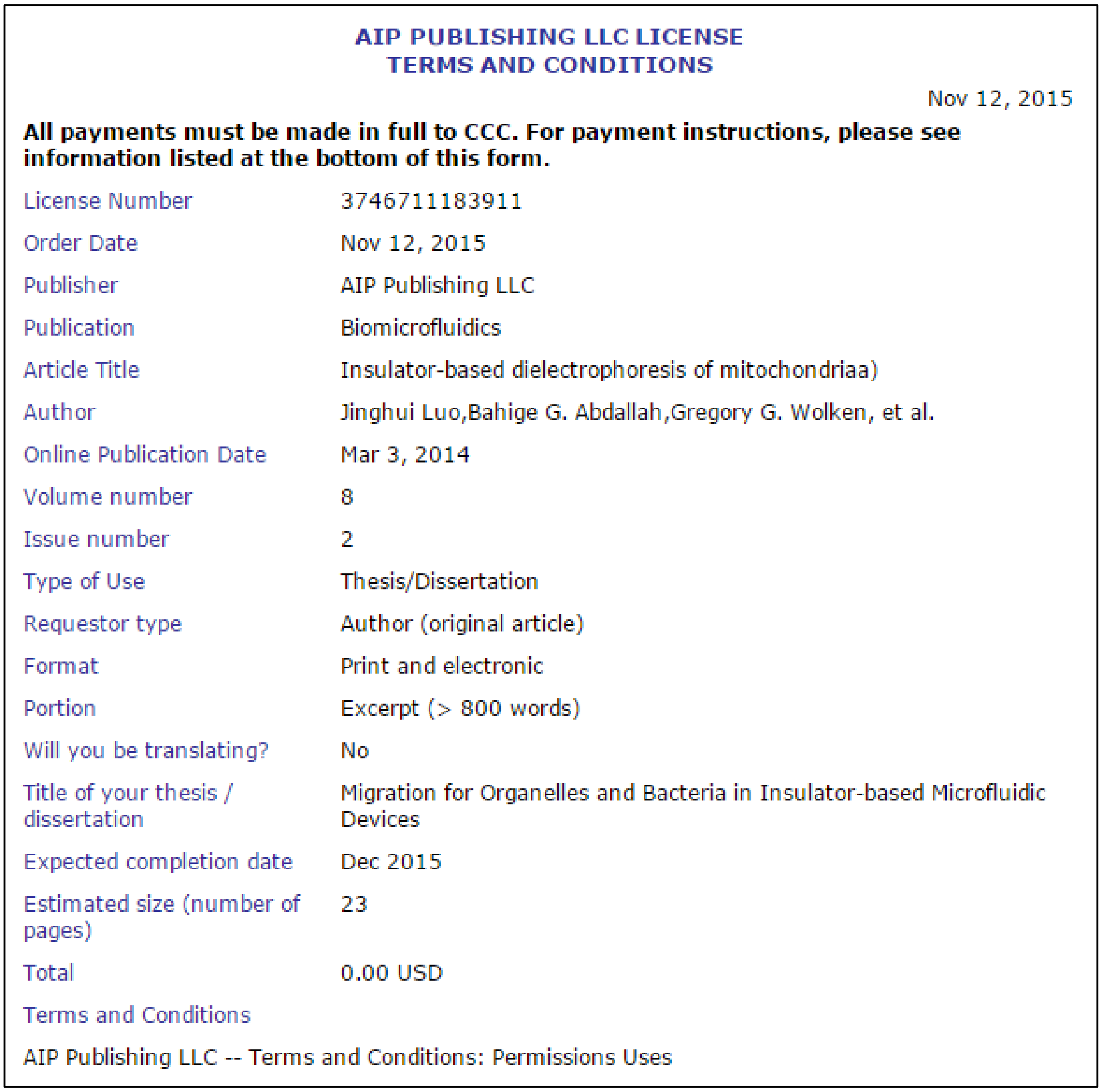

AIP PUBLISHING LLC LICENSE
TERMS AND CONDITIONS

Nov 12, 2015

All payments must be made in full to CCC. For payment instructions, please see information listed at the bottom of this form.

License Number	3746711183911
Order Date	Nov 12, 2015
Publisher	AIP Publishing LLC
Publication	Biomicrofluidics
Article Title	Insulator-based dielectrophoresis of mitochondriaa)
Author	Jinghui Luo,Bahige G. Abdallah,Gregory G. Wolken, et al.
Online Publication Date	Mar 3, 2014
Volume number	8
Issue number	2
Type of Use	Thesis/Dissertation
Requestor type	Author (original article)
Format	Print and electronic
Portion	Excerpt (> 800 words)
Will you be translating?	No
Title of your thesis / dissertation	Migration for Organelles and Bacteria in Insulator-based Microfluidic Devices
Expected completion date	Dec 2015
Estimated size (number of pages)	23
Total	0.00 USD
Terms and Conditions	

AIP Publishing LLC -- Terms and Conditions: Permissions Uses

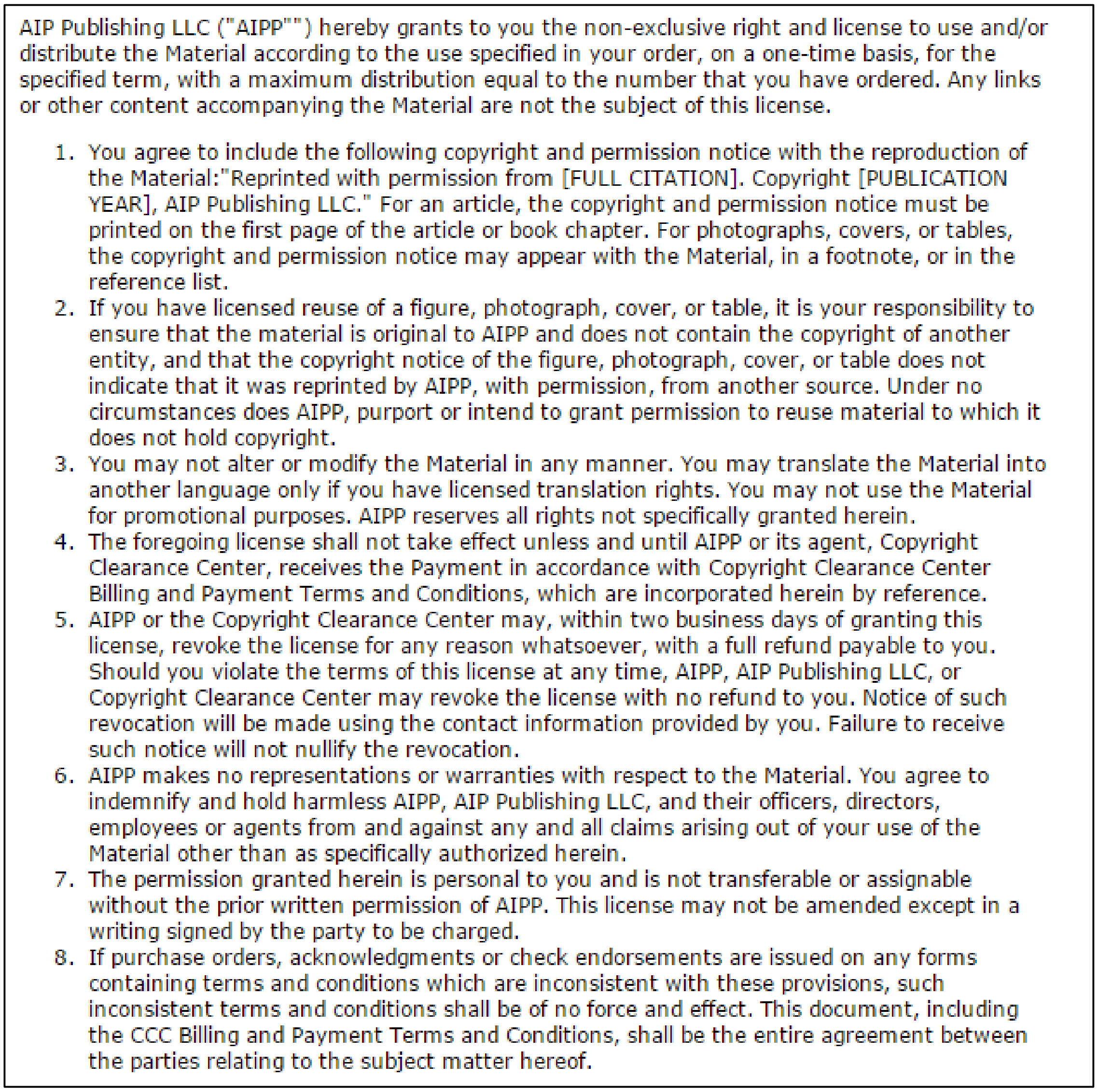

AIP Publishing LLC ("AIPP"") hereby grants to you the non-exclusive right and license to use and/or distribute the Material according to the use specified in your order, on a one-time basis, for the specified term, with a maximum distribution equal to the number that you have ordered. Any links or other content accompanying the Material are not the subject of this license.

1. You agree to include the following copyright and permission notice with the reproduction of the Material:"Reprinted with permission from [FULL CITATION]. Copyright [PUBLICATION YEAR], AIP Publishing LLC." For an article, the copyright and permission notice must be printed on the first page of the article or book chapter. For photographs, covers, or tables, the copyright and permission notice may appear with the Material, in a footnote, or in the reference list.
2. If you have licensed reuse of a figure, photograph, cover, or table, it is your responsibility to ensure that the material is original to AIPP and does not contain the copyright of another entity, and that the copyright notice of the figure, photograph, cover, or table does not indicate that it was reprinted by AIPP, with permission, from another source. Under no circumstances does AIPP, purport or intend to grant permission to reuse material to which it does not hold copyright.
3. You may not alter or modify the Material in any manner. You may translate the Material into another language only if you have licensed translation rights. You may not use the Material for promotional purposes. AIPP reserves all rights not specifically granted herein.
4. The foregoing license shall not take effect unless and until AIPP or its agent, Copyright Clearance Center, receives the Payment in accordance with Copyright Clearance Center Billing and Payment Terms and Conditions, which are incorporated herein by reference.
5. AIPP or the Copyright Clearance Center may, within two business days of granting this license, revoke the license for any reason whatsoever, with a full refund payable to you. Should you violate the terms of this license at any time, AIPP, AIP Publishing LLC, or Copyright Clearance Center may revoke the license with no refund to you. Notice of such revocation will be made using the contact information provided by you. Failure to receive such notice will not nullify the revocation.
6. AIPP makes no representations or warranties with respect to the Material. You agree to indemnify and hold harmless AIPP, AIP Publishing LLC, and their officers, directors, employees or agents from and against any and all claims arising out of your use of the Material other than as specifically authorized herein.
7. The permission granted herein is personal to you and is not transferable or assignable without the prior written permission of AIPP. This license may not be amended except in a writing signed by the party to be charged.
8. If purchase orders, acknowledgments or check endorsements are issued on any forms containing terms and conditions which are inconsistent with these provisions, such inconsistent terms and conditions shall be of no force and effect. This document, including the CCC Billing and Payment Terms and Conditions, shall be the entire agreement between the parties relating to the subject matter hereof.

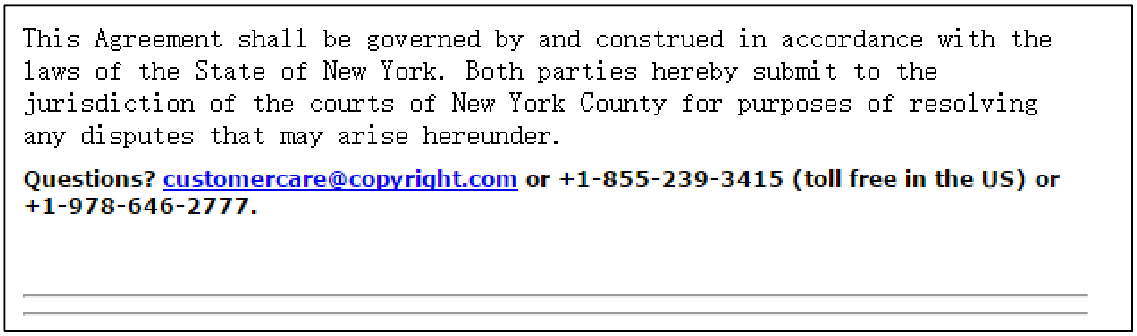

This Agreement shall be governed by and construed in accordance with the laws of the State of New York. Both parties hereby submit to the jurisdiction of the courts of New York County for purposes of resolving any disputes that may arise hereunder.

Questions? customercare@copyright.com or +1-855-239-3415 (toll free in the US) or +1-978-646-2777.